МИКРОЕЛЕКТРОНИКА И ОПТОЕЛЕКТРОНИКА
/
MICROELECTRONICS AND OPTOELECTRONICS, NANOSCIENCES AND NANOTECHNOLOGIES

(MO/MOI)

Efekti zračenja i odžarivanja kod naponsko temperaturno naprezanih p-kanalnih VDMOS tranzistora snage

Sandra Veljković, *Student Member, IEEE,* Nikola Mitrović, *Student Member, IEEE,* Snežana Đorić-Veljković, *Member, IEEE,* Vojkan Davidović, *Member, IEEE,* Snežana Golubović, *Member, IEEE,* Danijel Danković, *Member, IEEE*

***Sadržaj* — U radu su prikazani efekti zračenja i odžarivanja kod p-kanalnih VDMOS (vertical double-diffused metal-oxide semiconductor) tranzistora snage koji su prethodno bili izloženi naponsko temperaturnom naprezanju tokom različitih unapred tačno utvrđenih vremenskih perioda. Ovaj eksperiment je sproveden kako bi se ispitali efekti naprezanja zračenjem kod komponenata koje su prethodno bile izložene drugim uticajima, odnosno naprezanjima. Primećeno je da je promena napona praga tokom ozračivanja malo više izražena kod komponenata koje su bile izložene naponsko temperaturnom naprezanju negativnom polarizacijom gejta nedelju dana, što može biti od značaja u slučaju kada su komponente primile visoke ukupne doze. Pored toga, primećeno je da kod komponenata koje su naponski temperaturno naprezane jedan sat, a zatim ozračene do 90 Gy pri pozitivnoj polarizaciji gejta, termički aktivirani procesi tokom odžarivanja nisu dovoljni da se napon praga smanji na vrednost pre naponsko temperaturnih naprezanja, što bi moglo biti od interesa u slučaju kada komponente rade u pooštrenim uslovima.**

***Ključne reči* — VDMOS tranzistor snage; napon praga; NBT (negative bias temperature) nestabilnosti; ozračivanje; odžarivanje.**

I. UVOD

Zbog svojih specifičnih performansi VDMOS (vertical double-diffused metal-oxide semiconductor) tranzistori snage imaju široku primenu kako u komercijalnim, tako i u uređajima specijalne namene (u prekidačkim izvorima napajanja, u audio pojačavačima, u automobilskoj industriji u uređajima i sistemima koji predstavljaju i dodatnu i primarnu opremu [1-3]). Pri tome, u nekim aplikacijama mogu biti podvrgnuti i pooštrenim uslovima rada i/ili nekom od oblika naprezanja, tako da u poslednjih dvadeset godina postoji povećano interesovanje za istraživanje njihove pouzdanosti, kao i efekata koji se javljaju pri radu u određenim uslovima [2-20]. Istraživanja su bila usredsređena uglavnom na efekte koji se javljaju pri izlaganju visokim vrednostima električnog polja [4-6], pri ozračivanju [2, 7-9], kao i pri ispitivanju efekata ubrzanih visokom temperaturom [10-12] i efekata naponsko temperaturnih naprezanja [4, 13-19].

VDMOS tranzistori snage su veoma osetljivi na jonizujuće zračenje koje ozbiljno degradira napon praga (V_T) [2, 7-9], tako da je za primenu u radijacionom okruženju, postupak provere pouzdanosti važan za odabir visoko pouzdanih komponenata. Standardno ispitivanje pouzdanosti za ove komponente uključuje „burn-in“ testove, pri kojima se primenjuju polarizacija i povišena temperatura [10-12, 21, 22].

Naponsko temperaturne nestabilnosti koje nastaju usled negativne polarizacije gejta i povišene temperature (u literaturi poznate kao NBTI - negative bias temperature instability), su nestabilnosti koje kod p-kanalnog MOSFET-a dovode do degradacije veoma bitnih električnih parametara, od kojih je najkritičniji napon praga. Ove nestabilnosti se javljaju kao rezultat rada uređaja na povišenoj temperaturi (obično 100-250 ^{o}C) i sa negativnom polarizacijom gejta (pri električnom polju u oksidu gejta u opsegu 2-6 MV/cm) [13, 16, 23-25]. Iako se ovi uslovi mogu javiti pri sprovođenju testova [10, 11], mogu da se jave i u nekim primenama pri standardnom režimu rada VDMOS tranzistora snage [13]. Štaviše, ove komponente mogu biti izložene istovremeno i zračenju i NBT naprezanju, kao što je navedeno u [26-29]. Takođe, u nekim primenama je moguća kombinacija sa drugim vrstama naprezanja, poput izlaganja magnetnom polju [18-20] ili uslovima visoke temperature i vlažnosti [10].

Promena napona praga IRF9520 p-kanalnih VDMOS tranzistora snage izazvana NBT naprezanjem (koja se aktivno proučava već više godina [13, 16, 30-32]) se menja po dobro poznatom t^n zakonu. Pri tome se ova zavisnost može da podeli na tri faze u zavisnosti od vrednosti parametra n. Vremena koja odgovaraju kraju prve faze (1 sat) i druge faze (1 nedelja, tj. 168 sati) izabrana su kao periodi u toku kojih je naprezanje negativnom polarizacijom gejta primenjeno u eksperimentima čiji su rezultati analizirani u ovom radu.

U ovom radu prikazani su rezultati ozračivanja IRF9520 p-kanalnih VDMOS tranzistora snage, koji su prethodno naponski temperaturno naprezani negativnom polarizacijom gejta (NTNNP) 1 sat i 168 sati, sa ciljem da se pojasni efekat trajanja naprezanja negativnom polarizacijom gejta na kasnije efekte zračenja i odžarivanja. Na osnovu podataka o apsorbovanoj dozi pri tipičnoj primeni MOS komponenata u komunikacionim satelitima [33], izabrana je granica ukupne doze od 100 Gy (SiO_2).

Sandra Veljković – Univerzitet u Nišu, Elektronski fakultet, Aleksandra Medvedeva 14, 18000 Niš, Srbija (e-mail: sandra.veljkovic@elfak.rs).

Nikola Mitrović – Univerzitet u Nišu, Elektronski fakultet, Aleksandra Medvedeva 14, 18000 Niš, Srbija (e-mail: nikola.i.mitrovic@elfak.ni.ac.rs).

Snežana Đorić-Veljković – Univerzitet u Nišu, Građevinsko-arhitektonski fakultet, Aleksandra Medvedeva 14, 18000 Niš, Srbija (e-mail: snezana.djoric.veljkovic@elfak.ni.ac.rs).

Vojkan Davidović – Univerzitet u Nišu, Elektronski fakultet, Aleksandra Medvedeva 14, 18000 Niš, Srbija (e-mail: vojkan.davidovic@elfak.ni.ac.rs).

Snežana Golubović – Univerzitet u Nišu, Elektronski fakultet, Aleksandra Medvedeva 14, 18000 Niš, Srbija (e-mail: snezana.golubovic@elfak.ni.ac.rs).

Danijel Danković – Univerzitet u Nišu, Elektronski fakultet, Aleksandra Medvedeva 14, 18000 Niš, Srbija (e-mail: danijel.dankovic@elfak.ni.ac.rs).

II. EKSPERIMENT

Uzorci koji su testirani u eksperimentu su komercijalni, p-kanalni VDMOS tranzistori snage tipa IRF9520. Eksperimentalna procedura se sastojala od primene NTNNP, izlaganja γ-zračenju i termičkog odžarivanja, koji su međusobno bili odvojeni dvema fazama spontanog oporavka.

Primena NTNNP na komponente je obavljena u Heraeus HEP2 komorama za testiranje pouzdanosti, koje su obezbeđivale stabilnu temperaturu od 175 °C tokom 168 sati za prvu grupu uzoraka i 1 sat za drugu grupu uzoraka. Kod svih komponenata sors i drejn su bili uzemljeni, dok je primenjena polarizacija na gejtu bila - 45 V.

Uzorci su bili izloženi γ-zračenju korišćenjem izvora Co-60 sa brzinom doze od 0.5 Gy(SiO_2)/min u Laboratoriji za zaštitu od zračenja i zaštitu životne sredine, Instituta za nuklearne nauke "Vinča" u Srbiji. Obe grupe komponenata koje su najpre podvrgnute NTNNP (168 sati i 1 sat), kao i one koje nisu prethodno naprezane podeljene su u po dve podgrupe. Komponente prve podgrupe su ozračivane bez polarizacije, dok su komponente druge podgrupe ozračivane uz primenu pozitivne polarizacije gejta od +10 V, pri čemu su sors i drejn svih komponenata bili uzemljeni. Svih šest podgrupa komponenata su ozračene do ukupne doze od 90 Gy.

Završna faza eksperimenta, termičko odžarivanje, izvedeno je na 175°C tokom 168 sati bez primenjene polarizacije. Pored toga, treba napomenuti da su se komponente spontano oporavljale između NTNNP i zračenja (tokom 670 sati) i između zračenja i odžarivanja (tokom 15 sati), u oba slučaja na sobnoj temperaturi bez polarizacije komponenata.

U cilju praćenja degradacije komponenata, NTNNP, ozračivanje i odžarivanje su prekidani nakon prethodno definisanog vremenskog perioda da bi se snimale prenosne karakteristike I_D-V_G, na osnovu kojih je određen napon praga. Sva merenja su obavljana na sobnoj temperaturi. Na Sl. 1 su prikazani merna konfiguracija i uslovi merenja. Za električnu karakterizaciju je korišćen visoko precizni Keysight Technologies B2901A (Source Measure Unit - SMU), koji je kontrolisan pomoću laptopa, preko GPIB-a.

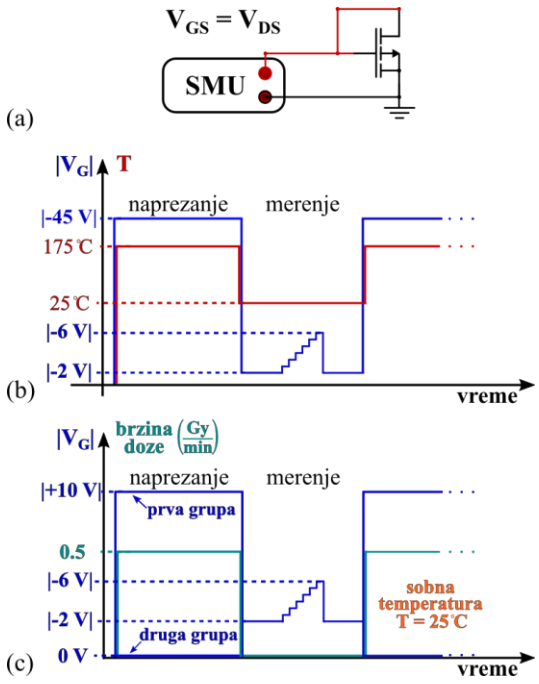

Sl. 1. Merenja istraživanih komponenata a) šema, i uslovi tokom naprezanja b) pri NTNNP i c) pri ozračivanju.

III. REZULTATI I DISKUSIJA

Iako je u toku svakog procesa naprezanja vršena karakterizacija, na Sl. 2 su prikazane samo prenosne strujno naponske karakteristike nakon NTNNP, ozračivanja do 90 Gy (pri V_G = +10 V) i odžarivanja. Pri tome su na Sl. 2a i Sl. 2b predstavljene neke od prenosnih karakteristika p-kanalnih VDMOS tranzistora snage koji su podvrgnuti NTNNP tokom 168 sati i 1-og sata, respektivno.

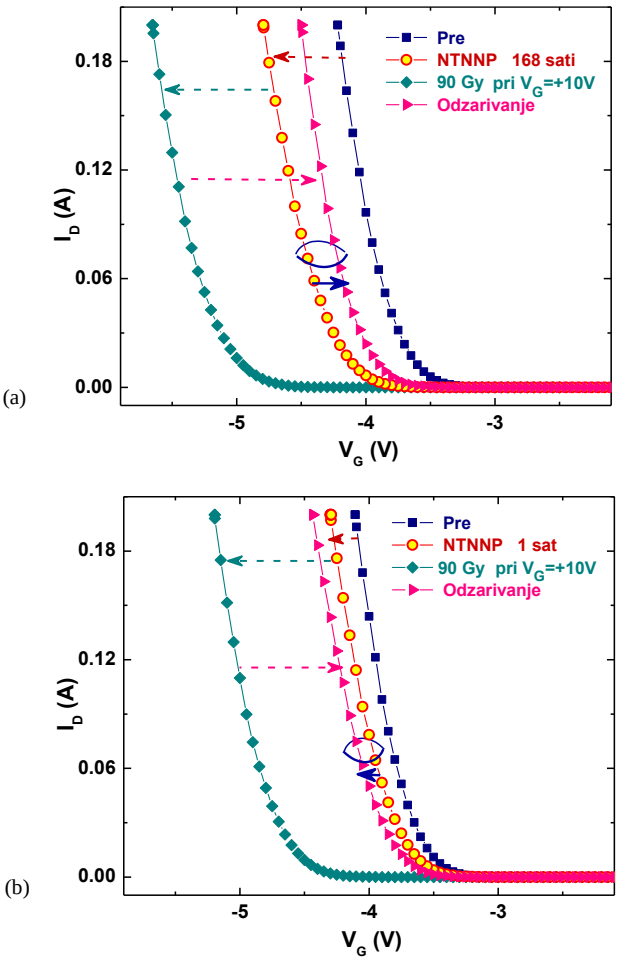

Sl. 2. Prenosne karakteristike p-kanalnog VDMOS tranzistora snage (IRF9520), nakon (a) 168 sati i (b) 1-og sata naponsko temperaturnog naprezanja, ozračivanja pri V_G = + 10 V i odžarivanja.

Na osnovu Sl. 2 se jasno uočava da nakon primene NTNNP dolazi do pomeranja prenosnih karakteristika duž V_G ose ka negativnijim vrednostima, što ukazuje na porast napona praga ispitivanih tranzistora po apsolutnoj vrednosti, pri čemu su ove promene jasno izraženije kod uzoraka koji su duže naprezani, kao što se vidi na Sl. 3a i Sl. 4a. Ozračivanje do 90 Gy, koje je sledilo, je dovelo do značajnog daljeg pomeranja karakteristika duž V_G ose ka negativnijim vrednostima, kod obe grupe komponenata, odnosno do porasta V_T po apsolutnoj vrednosti (Sl. 3b i Sl. 4b), što je uočeno i kod komponenata koje prethodno nisu podvrgnute NTNNP, kao što se vidi na Sl. 5a.

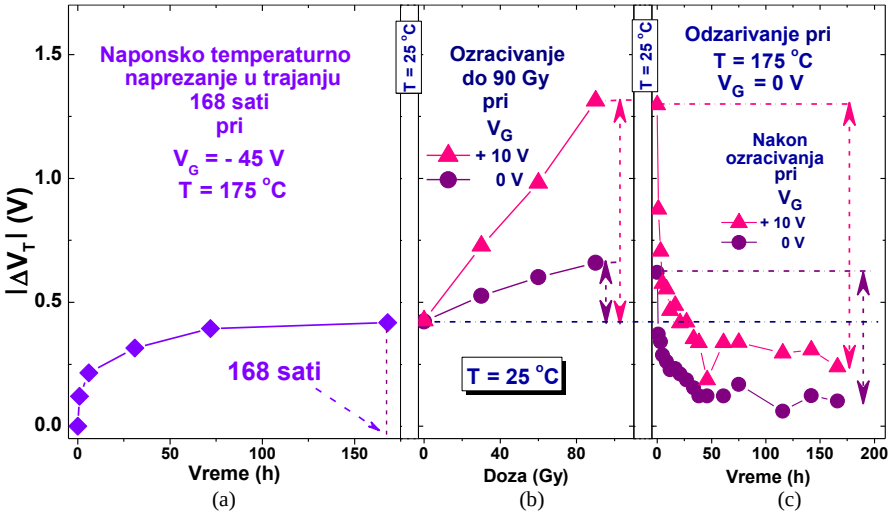

Sl. 3. Promene V_T p-kanalnih VDMOS tranzistora snage (IRF9520) tokom primene (a) NTNNP u trajanju od 168 sati, (b) ozračivanja i (c) odžarivanja.

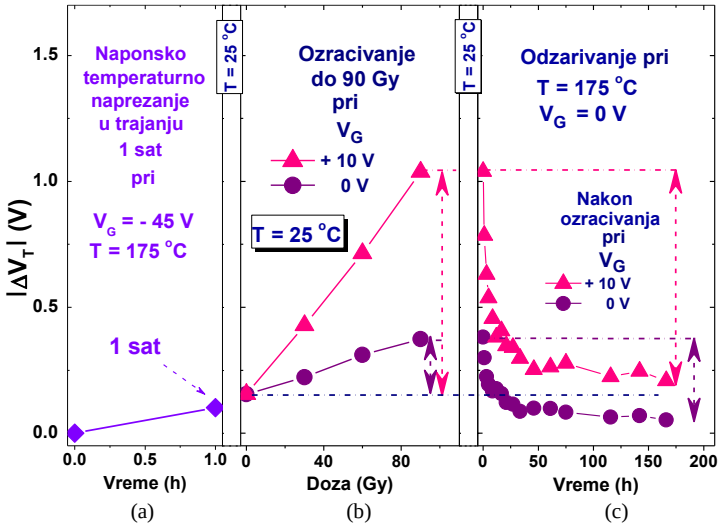

Sl. 4. Promene V_T p-kanalnih VDMOS tranzistora snage (IRF9520) tokom primene (a) NTNNP u trajanju od 1-og sata, (b) ozračivanja i (c) odžarivanja.

Tokom ozračivanja komponenata kod kojih je primenjena polarizacija gejta došlo je do veće promene V_T usled formiranja znatno većeg broja defekata u oksidu gejta i zahvatanja nosilaca naelektrisanja na površinskim stanjima. Uopšte, dobro je poznato da su promene V_T prouzrokovane formiranjem naelektrisanja u oksidu gejta i površinskih stanja tokom određenog naprezanja usled elektrohemijskih procesa koji uključuju defekte u oksidu, na međupovršini, šupljine i čestice vodonika.

Jonizujuće zračenje formira parove elektron-šupljina u strukturi gejta oksida i mada se neki parovi rekombinuju najveći broj elektrona napusti oksid [26]. Ukoliko je primenjena pozitivna polarizacija na gejt elektroni napuštaju oksid upravo kroz gejt, dok se najveći broj šupljina (koje imaju manju pokretljivost) zahvata na defektima, pri čemu dolazi do povećanja zahvaćenog pozitivnog naelektrisanja u oksidu [28]. U slučaju ozračivanja bez polarizacije gejta, u oksidu postoji malo pozitivno električno polje kao rezultat male kontaktne razlike potencijala između polisilicijumskog gejta i n-tipa balka kod p-kanalog MOSFET-a i može uticati

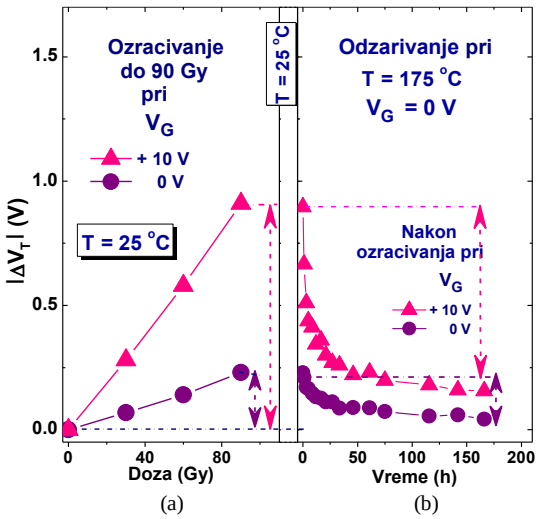

Sl. 5. Promene napona praga p-kanalnih VDMOS tranzistora snage (IRF9520) tokom (a) ozračivanja pri V_G = + 10 V i (b) odžarivanja.

na rezultate formiranja naelektrisanja u oksidu gejta pod dejstvom γ zračenja [34, 35].

Pored toga, konačni efekti ozračivanja zavise i od predistorije komponenata, tako da su konačne apsolutne vrednosti V_T najviše kod komponenata prethodno podvrgnutih NTNNP u toku 168 sati, dok su najmanje kod komponenata koje prethodno nisu podvrgnute NTNNP. Međutim, brzina promene V_T u toku procesa ozračivanja je nešto manje izražena kod komponenata podvrgnutih NTNNP, što može biti posledica manje brzine porasta i gustine naelektrisanja u oksidu gejta i površinskih stanja zbog smanjenog broja prekursora defekata nakon NTNNP. Pri tome su promene V_T tokom zračenja nešto izraženije kod komponenata prethodno podvrgnutih NTNNP tokom 168 sati nego tokom 1-og sata i ova razlika može biti posledica razlike u nastalim i započetim procesima u prvoj i drugoj fazi primenjenog NTNNP. Srednje vrednosti razlika u promenama napona praga nakon ozračivanja do 90 Gy (ΔV_T (90 Gy)) i nakon primene NTNNP (ΔV_T (NTNNP)) su naznačene strelicama na desnoj strani Sl. 3b, Sl. 4b, a na Sl. 5a samo nakon ozračivanja i date su u Tab. 1.

Tabela 1. Srednje vrednosti promene ΔV_T nakon ozračivanja u odnosu na vrednosti nakon primenjenog NTNNP.

	Vreme primenjenog NTNNP		
	168 sati	1 sat	0 (bez NTNNP)
V_G tokom ozračivanja	ΔV_T (90 Gy) - ΔV_T (NTNNP) (V)		ΔV_T (90 Gy)
+ 10 V	0.897	0.882	0.912
0 V	0.220	0.218	0.232

Za komponente ozračene do 90 Gy, pri V_G=+10 V razlika je 0.16 mV/Gy između komponenata na koje je primenjeno NTNNP 168 sati i 1 sat. Iako ove vrednosti nisu posebno velike mogu biti od interesa u slučaju ozračivanja do visokih doza, koje mogu biti primljene tokom rada uređaja u elektronskim sistema pri dugotrajnoj misiji u radijacionom okruženju.

Odžarivanje koje je primenjeno nakon ozračivanja i kratkotrajnog spontanog oporavka (Sl. 3c, Sl. 4c i Sl. 5b) dovodi do značajnog opadanja V_T po apsolutnim vrednostima. Pri tome je ovo opadanje najveće na samom početku, kod svih grupa komponenata i izraženije je ukoliko je pri ozračivanju primenjena polarizacija gejta. Vrednosti promena V_T u toku odžarivanja, kod komponenata na koje je primenjeno NTNNP (Sl. 3c i Sl. 4c), kao i na koje nije primenjeno NTNNP (Sl. 5b) date su u Tab. 2, a ove promene su naznačene i strelicama na desnoj strani ovih slika.

Treba napomenuti da konačne vrednosti ΔV_T postignute nakon vremena odžarivanja od 168 sati na temperaturi od 175°C, u odnosu na vrednosti posle primene NTNNP, kvalitativno zavise od trajanja primenjenog NTNNP. Naime, kod svih komponenata na koje je primenjeno NTNNP u toku 168 sati, konačne (apsolutne) vrednosti ΔV_T nakon odžarivanja su niže od onih neposredno nakon NTNNP. Međutim, kod komponenata na koje je primenjeno NTNNP u toku jednog sata vrednosti ΔV_T nakon odžarivanja su niže od onih neposredno nakon NTNNP za komponente ozračene bez polarizacije (pri V_G=0 V), dok su za komponente ozračene sa polarizacijom (pri V_G=+10 V) više. Ove razlike u vrednostima promena V_T mogu se videti sa Sl. 3c, i Sl. 4c, a mogu se jasno uočiti i na Sl. 2, gde je naznačen odnos karakteristika nakon NTNNP i nakon odžarivanja.

Tabela 2. Srednje vrednosti promene ΔV_T u toku odžarivanja.

	Vreme primenjenog NTNNP		
	168 sati	1 sat	0 (bez NTNNP)
V_G tokom ozračivanja	ΔV_T u toku odžarivanja (V)		
+ 10 V	1.0582	0.8306	0.7842
0 V	0.5194	0.3290	0.1980

Tokom odžarivanja ispitivane komponente nisu bile polarisane, pa su efekti koji se javljaju u komponentama termički aktivirani, tako da procesi koji se dešavaju i elektrohemijske reakcije mogu biti u vezi sa difuzijom nekih čestica vodonika. Tako čestice kao što su neutralni molekuli H_2 i pozitivni joni H^+ mogu da difunduju sa mesta gde je njihova koncentracija veća (oksid) ka mestima sa nižom koncentracijom (međupovršina), a može doći i do preraspodela zahvaćenog pozitivnog naelektrisanja u oksidu [36, 37]. Očigledno termički aktivirani procesi odžarivanja bez polarizacije (koji su u vezi sa difuzijom čestica vodonika) nisu dovoljni da smanje vrednosti promena napona praga na vrednost pre primene NTNNP kod komponenata na koje je primenjeno NTNNP u toku jednog sata i ozračivanih do 90 Gy pod polarizacijom V_G=+10 V.

IV. Zaključak

U ovom radu su prikazani eksperimentalni rezultati zračenja i odžarivanja p-kanalnih VDMOS tranzistora snage nakon primene naponsko temperaturnog naprezanja negativnom polarizacijom gejta tokom 168 sati i 1 sat. Svrha istraživanja je bila da se rasvetli trajanje NTNNP na efekte zračenja i odžarivanja, kako bi se ispitali efekti specifičnog uticaja zračenja na uređaje koji su prethodno bili izloženi naprezanju. Pokazano je da zračenje dovodi do daljeg porasta V_T kod svih komponenata koje su prethodno izložene NTNNP, pri čemu je ovaj porast malo izraženiji kod komponenata koje su prethodno bile izložene NTNNP tokom 168 sati, nego kod onih koje su bile izložene tokom jednog sata. To bi moglo biti od interesa u slučaju ozračivanja do visokih doza, koje mogu biti primljene tokom rada uređaja u elektronskim sistemima pri dugotrajnoj misiji u radijacionom okruženju. Takođe, primećeno je da kod uređaja izloženih NTNNP tokom jednog sata i ozračenih do 90 Gy pod polarizacijom, termički aktivirani procesi tokom odžarivanja (povezani sa difuzijom neutralnih čestica, kao što su molekuli vodonika) nisu dovoljni za smanjenje V_T na vrednost pre izlaganja NTNNP. To može biti od interesa kada se komponente ugrađuju u uređaje koji rade u pooštrenim uslovima, u okruženja gde su izloženi višestrukim naprezanjima.

ZAHVALNICA

Prikazani rezultati dobijeni su u okviru programa za finansiranje naučnoistraživačkog rada (pod brojem 451-03-9/2021-14/200102) koji finansira Ministarstvo prosvete, nauke i tehnološkog razvoja Republike Srbije i u okviru projekta "Osobine tankih i ultratankih oksidnih slojeva" (F-148), koji finansira Srpska akademija nauka i umetnosti-SANU. Rezultatima predstavljenim u ovom radu je u mnogome doprineo nedavno preminuli akademik Ninoslav Stojadinović i svojim naučnim i istraživačkim aktivnostima i značajnom saradnjom sa autorima.

LITERATURA

[1] B. Jayant Baliga, *Fundamentals of Semiconductor Power Devices*, Springer, New York, 2008.
[2] T. P. Ma and P. V. Dressendorfer, Ionizing Radiation Effects in MOS Devices and Circuits, 1989, Wiley; New York.
[3] S. Gamerith and M. Polzl, Negative bias temperature stress in low voltage p-channel DMOS transistors and role of nitrogen, *Microelectron. Reliab.* 42, 2002, 1439-1443.
[4] N. Stojadinović et al., Effects of electrical stressing in power VDMOSFETs, Microelectron. Reliab. 45, 2005, 115-122.
[5] G. S. Ristić, et al. Defect behaviors in n-channel power VDMOSFETs during HEFS and thermal post-HEFS annealing, Appl. Surf. Sci. 252 (8), 2006, 3023–3032.
[6] X. R. Ye et al., VDMOSFET HEF degradation modelling considering turn-around phenomenon, *Microelectron. Reliab.* 50, 2018, 37-41.
[7] N. Stojadinović et al., Analysis of gamma-irradiation induced degradation mechanisms in power VDMOSFETs, *Microelectron. Reliab.* 35, 1995, 587-602.
[8] C. Pickard et al., Use of commercial VDMOSFETs in electronic systems subjected to radiation, *IEEE Trans. Nucl. Sci.* 47, 2000, 627-633.
[9] M. S. Park, C. R. Wie, Study of radiation effects in γ-ray irradiated power VDMOSFET by DCIV technique, *IEEE Trans. Nucl. Sci.* 48, 2001, 2285-2293.
[10] N. Tošić, et al., High-temperature-reverse-bias testing of power VDMOS transistors, *Microelec. Reliab.* 37, 1997, 1759-1762.
[11] S. Djorić-Veljković et al, Effects of burn-in stressing on post-irradiation annealing response of power VDMOSFETs, *Microelectron. Reliab.* 43, 2003, 1455-1460.
[12] P. Magnone et al., Investigation of degradation mechanisms in low-voltage p-channel power MOSFETs under High Temperature Gate Bias stress, *Microelectron. Reliab.* 88-90, 2018, 438-442.
[13] N. Stojadinović et al., Negative bias temperature instability mechanisms in p-channel power VDMOSFETs, *Microelectron. Reliab.* 45, 2005, 1343-1348.
[14] I. Manić et al., NBTI related degradation and lifetime estimation in p-channel power VDMOSFETs under the static and pulsed NBT stress conditions, *Microelectron. Reliab.* 51, 2011, 1540-1543.
[15] A. N. Tallarico et al., Negative bias temperature stress reliability in trench-gated p-channel power MOSFETs, *IEEE Trans. Dev. Mater. Reliab.* 14, 2014, 657-663.
[16] N. Stojadinović et al., Negative Bias Temperature Instability in Thick Gate Oxides for Power MOS Transistors, in *Bias Temperature Instability for Devices and Circuits*, edited by Tibor Grasser, 2014, Springer, New York, 533-559.
[17] D. Danković et al., Negative bias temperature instability in p-channel power VDMOSFETs: recoverable versus permanent degradation, *Semicond. Sci. Technol.* 30, 2015, 105009.
[18] H. Tahi et al., Experimental Investigation of NBTI Degradation in Power VDMOS Transistors Under Low Magnetic Field, *IEEE Trans. Device Mater. Reliab.* 17 (1), 2017, 99-105.
[19] A. Bhattacharjee, S.N. Pradhan, NBTI-Aware Power Gating Design with Dynamically Varying Stress Probability Control on Sleep Transistor, *J. Circuit Syst. Comp.* 2021, Art. no 2120004 2120004.
[20] H. Tahi et al., Capacitance–Voltage Technique Based on Time Varying Magnetic Field for VDMOSFET-Part I: Concept and Implementation, *IEEE Trans. on Elec. Dev.* 68 (5), 2021, 2173-2180
[21] N. Stojadinović et al., Effects of High Electric Field and Elevated-Temperature Bias Stressing on Radiation Response in Power VDMOSFETs, *Microelectron. Reliab.* 42, 2002, 669-677.
[22] N. Stojadinović et al., Effects of Burn-in Stressing on Radiation Response of Power VDMOSFETs, *Microelectron. J.*, 33, 2002, 899-905.
[23] D. K. Schröder, J. A. Babcock, Negative bias temperature instability: Road to cross in deep submicron silicon semiconductor manufacturing, *J. Appl. Phys.* 94, 2003, 1-18.
[24] J. H. Stathis, S. Zafar, The negative bias temperature instability in MOS devices: A Review, *Microelectron. Reliab.* 46, 2006, 270-286.
[25] T. Grasser et al., Recent advances in understanding the bias temperature instability, *IEEE Proc. IEDM*, 2010, 82-85.
[26] V. Davidović et al., NBTI and irradiation effects in p-channel power VDMOS Transistors, *IEEE Trans. Nucl. Sci.* 63, 2016, 1268-1275.
[27] V. Davidović et al., Effects of consecutive irradiation and bias temperature stress in p-channel power vertical double-diffused metal oxide semiconductor transistors, *Jap. J. App. Phys.* 57 (4), 2018, 044101-1-10.
[28] V. Davidović et al., NBT Stress and Radiation Related Degradation and Underlying Mechanisms in P-Channel Power VDMOS Transistors, *Facta Universitatis: Electronics and Energetics*, 16 (4), 2018, 367-388.
[29] D. Danković, et al., Radiation and Annealing Related Effects in NBT Stressed P-Channel Power VDMOSFETs, prihvaćeno za *32nd European Symposium on Reliability of Electron Devices, Failure Physics and Analysis (ESREF 2021*), Bordeaux (France) 8-8 October 2021
[30] D. Danković et al., Implications of Negative Bias Temperature Instability in Power MOS Transistors, in *Micro Electronic and Mechanical Systems*, edited by Kenichi Takahata, 2009, IN-TECH Press, Boca Raton, 19.319-19.342
[31] D. Danković et al., Negative Bias Temperature Instabilities in Sequentialy Stressed and Annealed in p-Channel Power VDMOSFETs, *Microelectron. Reliab.* 47, 2007, 1400-1405.
[32] I. Manić et al., Effects of Low Gate Bias Annealing in NBT Stressed p-Channel Power VDMOSFETs, *Microelectron. Reliab.* 49, 2009, 1003-1007
[33] D.M. Fleetwood et al., An overview of radiation effects on electronics in the space telecommunication environment, *Microelectron. Reliab*. 40, 2000, 17-26.
[34] T. R. Oldham and J. M. McGarrity, Comparison of ^{60}Co response and 10keV X-ray response in MOS capacitors, *IEEE Trans. Nucl. Sci.*, 30, 1983, 4377-4381.
[35] M.M. Pejovic, Application of p-channel power VDMOSFET as a high radiation doses sensor, *IEEE Trans. Nucl. Sci.* 62, 2015, 1905-1910.
[36] D. M. Fleetwood, Effects of hydrogen transport and reactions on microelectronics radiation response and reliability, *Microelectron. Reliab*. 42, 2002, 523-541.
[37] T. Grasser et al., The paradigm shift in understanding the bias temperature instability: from reaction-diffusion to switching oxide traps, *IEEE Trans. Electron. Dev.* 58, 2011, 3652-3666.

ABSTRACT

The radiation and annealing effects in p-channel VDMOS power transistors which were formerly exposed to the negative bias temperature stress during different previously exactly determined time periods are presented in the paper. This experiment was conducted in order to explore the effects of particular radiation stress in components which were formerly exposed to other influences that may act as stress. It was noticed that radiation response of threshold voltage was slightly further changed for components which were previously NBT (negative bias temperature) stressed for one week, what may be of importance when high total doses were received. Besides, it was noticed that in components exposed to NBT stress for one hour before irradiation (up to 90 Gy) with positive gate voltage applied, thermally activated processes during subsequent annealing are not enough to reduce V_T to the magnitude before NBT stress, which might be of interest in the case when components work under harsh conditions.

Effects of Radiation and Annealing in Bias Temperature Stressed p-channel power VDMOS transistors

SandraVeljković, Nikola Mitrović, Snežana Đorić-Veljković, Vojkan Davidović, Snežana Golubović and Danijel Danković

Porast elektroprovodnosti Li-jonskih baterija oblaganjem elektroda metal-oksidnim nano-filmovima

Jovan P. Šetrajčić, Siniša M. Vučenović, Igor J. Šetrajčić, Stevo K. Jaćimovski,
Ana J. Šetrajčić-Tomić, Dušan I. Ilić, Nikola R. Vojnović

***Apstrakt* — U radu su predstavljeni rezultati teoriskih istraživanja ponašanja fononskog podsistema u ultratankim metal-oksidnim (MO) prevlakama kakve se nanose na elektrode u Li-jonskim baterijama radi povećanja efikasnosti jonskog transporta. Primenjen je metod Grinovih funkcija i numeričkom analizom je pokazano da kod ultratankih filmova i to normalno na granične površi tog filma, dolazi do pojave izrazito pojačanog mehaničkog oscilovanja kristalne rešetke i formiranja stojećih talasa, čime fononi podstiču oslobađanje zarobljenih jona u graničnim slojevima elektroda i time povećavaju efikasnost jonskog transporta između elektroda, a time i doprinose uvećanju elektro-provođenja ovih baterija.**

***Ključne reči*—Li-jonske baterije; jonska provodnost; fononi; ultratanke film-strukture.**

I. Uvod

U ovom radu će se analizirati nanostrukturni materijali za poboljšanje energetske konverzije i skladištenje energije. Li-jon baterije bi trebalo da mogu da zadovolje izuzetno visoko postavljene ciljeve jer imaju vrlo visoku zapreminsku (oko 300 Wh/m^3) i težinsku (oko 130 Wh/kg) specifičnu energetsku gustinu [1], tj. imaju visoku kapacitivnost, veliku gustinu energije i radni napon. Ali u praksi se ne dostižu ni približno te vrednosti. Radi povećanja ključnih energetskih parametara, neophodno je obezbediti veću površinu elektroda, jer je glavni problem – relativno slab jonski transport koji još opada u toku svakog radnog punjenja baterije. Tako, na žalost, veća površina ne dovodi do očekivanih rezultata. Naime, prvenstveno – veoma je važno kako napraviti mikrostrukturu kompozita elektrode dostupnom za Li-jone, a da oni ne budu zarobljavani.

U tom smislu, nanostrukturni materijali u Li-jonskim baterijama igraju važnu ulogu. Naime, nanostrukturni materijali, zbog njihove posebne morfologije, pokazuju neo-čekivano elektrohemijsko ponašanje. Važno je napomenuti da, kada se nanostrukturni materijali koriste u Li-jonskim baterijama, njihove male dimenzije (do 10-tak nm) samo dovode do kraće dužine difuzije i veće površine Li inkorporiranja u čvrstu matricu. Ovaj problem se može rešiti upotrebom aktivnih materijala sa debljinom zidova od oko 10 – 20 nm [2]. Ovi materijali pozitivno utiču na jonski kontakt između aktivnih materijala i elektrolita. Jednaku zaslugu oni imaju i u postizanju boljeg elektronskog provođenja.

Dakle, za efikasno funkcionisanje Li-jon baterije potrebno je nesmetano paraleno provođenje elektronima i jonima, a za baterije velike snage ovakvo provođenje je i suštinsko. Ovde će biti analizirano nekoliko vidova nano-arhitektura specifičnog dizajna, prvenstveno od MO materijala.

II. Elektrode u Li-jonskim baterijama

Sve funkcionalne tehnologije baterija imaju kinetičkih problema sa opadajućom jonskom difuzijom kako u čvrstim Li elektrodama, tako i sa provodljivošću kroz elektrolite. U te svrhe, za poboljšanje jonske kinetike obično se predlažu specijalne arhitekture nano-strukturnih elektroda [2], koje se izrađuju u obliku dodatnog nanošenja ultratankih filmova na korišćene elektrode.

U toku rada baterije kontakt između elektroda i tih dodatih filmova treba da obezbedi mehaničku koheziju, ali i da pozitivno utiče na električne osobine elektroda preko površinske modifikacije. Korišćenjem mikroskopije atomskom silom (AFM), u radu [3] proučavane su površinski strukturni nanosi sa tri veziva: polivinildenfluorid (PVDF), carboksimethil celuloza (CMC) i želatin. Učinjeni su veliki napori da se pronađe veza između svojstava i arhitekture posmatranih struktura i elektrohemijskih karakteristika procesa punjenja–pražnjenja baterije.

Poboljšanje jonske/elektronske provodnosti može se postići primenom više metoda, uključujući i nanošenje ugljenika, jonski super-valentni doping umesto Li i nano-umrežavanje elektronski provodnih metala. Pomoću ovoga može se dobiti dopirani materijal sa značajnom elektronskom provodljivosti – i do $4{,}8\cdot10^{-2}$ S/cm. Iz ovih rezultata sledi da će i ostale osobine upotrebljenih materijala, kao što su fazne transformacije, imati značaan uticaj na ukupnu efikasnost [4].

$Li_{1-x}CoO_2$ je komercijalno najdostupniji materijal katode. Na žalost, njegova praktična primena je ograničena relativno velikom nestabilnošću, jer se brzo raspada već pri naponima iznad 4,2 V. Međutim, i ove nestabilnosti mogu se razrešiti upotrebom premaza $LiCoO_2$ praha nanošenjem MO nanoskopske debljine – do nekoliko desetina nm [5]. Primeri MO koji su istraživani su, npr. Al_2O_3, ZrO_2, ZnO, SiO_2, TiO_2,

Jovan P. Šetrajčić, Igor Šetrajčić i Ana Šetrajčić-Tomić – *Akademija nauka i umjetnosti Republike Srpske, Banja Luka, Republika Srpska, BiH* (e-mail: jovan.setrajcic@gmail.com, seki_1976@yahoo.com, setrajcic.a@gmail.com).

Siniša M. Vučenović – *Univerzitet u Banjoj Luci, Prirodno-matematički fakultet*, *Dr Mladema Stojanovića 2, 78000 Banja Luka, Republika Srpska, BiH* (e-mail: vucenovic.s@gmail.com).

Stevo K. Jaćimovski, *Kriminalističko-policijski univerzitet, Cara Dušana 196, 11080 Zemun – Beograd, Srbija* (e-mail: jacimovskis@gmail.com)..

Dušan I. Ilić i Nikola R. Vojnović – *Univerzitet u Novom Sadu, Fakultet tehničkih nauka, Trg Dositeja Obradovića 6, 21000 Novi Sad, Srbija* (e-mail: dusilic69@gmail.com).

$AlPO_4$ i AlF_3. Većina metoda formiranja prevlaka zasnivaju se na tehnikama kao što je *sol-gel*, ali se sve češće koristi metoda taloženja atomskog sloja (ALD – *Atomic Layer Deposition* [5]), koja je zapravo gasno–fazno formiranje ultratankih filmova.

III. Uloga ultratankih premaza elektroda

U najopštijem slučaju, efikasnost elektroda se može dovesti u direktnu vezu sa migracijom jona: što je ona veća, veća je i efikasnost elektrode (Sl. 1).

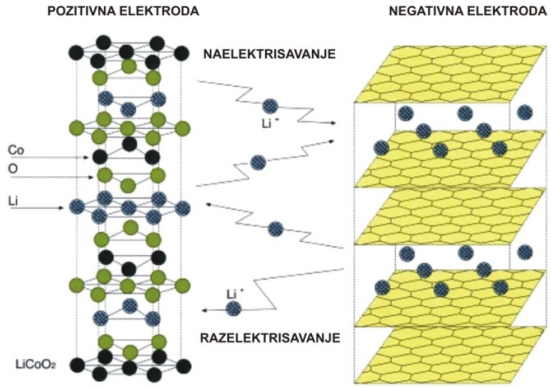

Sl. 1. Prikaz migracije jona u Li-jonskim baterijama (iz [3])
Fig. 1. Demonstration of ion migration in Li-ion batteries (from [3])

Opravdano se postavlja sledeće pitanje: na osnovu čega je povećana efikasnost elektroda posledica prisustva premaza, jer premaz, suštinski predstavlja dodatnu „barijeru“ prolasku jona. Pokazaćemo da odgovor leži u izmenjenim mehaničim svojstvima premaza zbog delovanja „konfajnment“ uslova. Naime, nije nemoguće napraviti totalnu analogiju tankih elektrodnih premaza i ultra-tankih MO filmova. Nakon uspostavljanja ove analogije, ostaje da se istraži uloga fononskog podsistema ultratankih filmova, a to je i učinjeno nadalje u ovom radu, jer je upravo taj sistem odgovoran za neobične mehaničke osobine.

Modelni ultratanki filmovi [6–9] predstavljaju strukture sa narušenom translacionom simetrijom duž jednog pravca. Ovakve kristalne nanostrukture mogu se teorijski analizirati pomoću metoda sa jednočestičnim talasnim funkcijama, ali ovakav prilaz nije „zatvoren u sebe“, jer se za izračunavanje statitičkih srednjih vrijednosti moraju „uzajmljivaiti“ statističke formule. Jedini potpuno kompletan je metod Grinovih funkcija (GF) [10–15], jer on pruža mogućnost za ozračunavanje dinamičkih i statističkih karakteristika posmatranog sistema. Kao prvo i osnovno, ovaj metod smo uspešno „prilagodili“ za istraživanje nanoskopskih kristalnih struktura [16–20] u kojima egzistiraju nanoskopske dimenzije i postoje različite granične površi, poznate kao „konfajnment“ uslovi, koji unose najbitnije promene u sve fundamentalne osobine date strukture.

IV. Mehaničko oscilovanje u film-strukturi

Hamiltonijan mehaničkih oscilacija u ultratankom filmu (Sl. 2) uzet u aproksimaciji najbližih suseda i uz zanemarivanje torzionih efekata je oblika

$$H = \frac{1}{2M}\sum_{\vec{n}} p_{\vec{n}}^2 + \frac{C}{2}\sum_{\vec{n}}\left[\left(u_{\vec{n}} - u_{\vec{n}-\vec{a}_x}\right)^2 + \left(u_{\vec{n}} - u_{\vec{n}-\vec{a}_y}\right)^2 + \left(u_{\vec{n}} - u_{\vec{n}-\vec{a}_z}\right)^2\right], \quad (1)$$

gde su u – pomjeraji, p – impulsi, M – mase molekula i C – Hukove konstante istezanja. Torzioni efekti mogu biti isključeni, jer se fundamentalni efekat postiže u pravcu normalnom na granične površi strukture, dakle duž pravca gde je posmatrana struktura debljine do desetak nm i zanemariva je u odnosu na druge dve dimenzije!

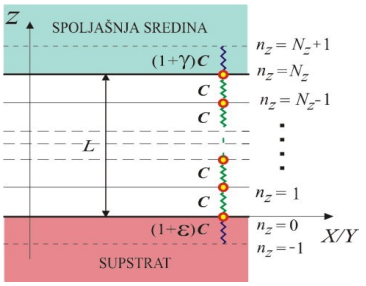

Sl. 2. Model fononskog ultratankog filma (iz [15])
Fig. 2. Model of phonon ultrathin film (from [15])

Posmatraćemo GF tipa pomeraj-pomeraj, koja se definiše [13–15], na sedeći način:

$$\Psi_{\vec{n},\vec{m}}(t) \equiv \Psi_{n_x,n_y,n_z;m_x,m_y,m_z}(t) \equiv << u_{\vec{n}}(t) | u_{\vec{m}}(0) >>= \theta(t) < [u_{\vec{n}}(t), u_{\vec{m}}(0)] >, \quad (2)$$

a GF tipa impuls-impuls:

$$\Phi_{\vec{n},\vec{m}}(t) \equiv \Phi_{n_x,n_y,n_z;m_x,m_y,m_z}(t) \equiv << p_{\vec{n}}(t) | p_{\vec{m}}(0) >>= \theta(t) < [p_{\vec{n}}(t), p_{\vec{m}}(0)] >. \quad (3)$$

Pri rešavanju sistema jednačina za ove GF iskorišćena je činjenica da je film dimenziono neograničen u x i y pravcu i da je translatorno invarijantan. Međutim, duž pravca narušenja simetrije (z) granični uslovi postoje i moraju se pravilno definisati:

$$u(n_z = -1) = u(n_z = N_z - 1) = 0; \quad p(n_z = -1) = p(n_z = N_z - 1) = 0. \quad (4)$$

Zbog ovakvih graničnih uslova jednačine za određivanje Ψ i Φ „raspadaju se“ na sistem od tri jednačine [13]. Zbog toga, komponente funkcija Ψ i Φ zavise od indeksa sloja n_z, pa se moraju razvijati po stojećim talasima oblika $\sin(N_z + 2)\varphi_\mu$, gde je parametar φ_μ definisan kao:

$$\varphi_\mu = \frac{\pi\mu}{N_z + 2}; \quad \mu = 1,2,...,N_z + 1. \quad (5)$$

Veoma je bitna činjenica ta da, u formuli (5), broj μ ne može da uzme vrijednost 0, a ni N_z+2, jer bi tada GF Ψ i Φ bile jednake nuli, a to je neinteresantan – trivijalni slučaj.

Opisanim postupkom određene su GF Ψ i Φ, a njihovi polovi u ω ravni, koji određuju energetsa stanja elementarnih pobuđenja – ovde fonona, definisani su sledećom kvadratnom determinantom:

$$D_{N_z+1}(\rho) = \begin{vmatrix} \rho-\varepsilon & 1 & 0 & \dots & 0 & 0 & 0 \\ 1 & \rho & 1 & \dots & 0 & 0 & 0 \\ 0 & 1 & \rho & \dots & 0 & 0 & 0 \\ \cdot & \cdot & \cdot & \ddots & \cdot & \cdot & \cdot \\ 0 & 0 & 0 & \dots & \rho & 1 & 0 \\ 0 & 0 & 0 & \dots & 1 & \rho & 1 \\ 0 & 0 & 0 & \dots & 0 & 1 & \rho-\gamma \end{vmatrix}_{N_z+1}$$

gde je

$$\rho_k^\alpha = \frac{\omega^2}{\Omega_\alpha^2} - 4\sin^2\frac{ak_x}{2} - 4\sin^2\frac{ak_y}{2} - 2 \equiv \rho,$$

Ali i sledećim uslovom:

$$D_{N_z+1}(\rho) = 0. \tag{6}$$

U sasvim opštem slučaju, uslov (6) nije egzaktno rešiv, jer njegov red, kao i rešenje zavise od tri parametra: ε, γ i N_z, čeje vrednosti diktira sama modelna struktura, njena arhitektura, ali i precifična kontaktna svojstva supstrata, ovde elektroda i lepka, i okoline, ovde elektrolita.

Egzaktno rešenje ipak postoji, u potpuno idealizovanom slučaju [16], kada parametri filma imaju vrednost: $\varepsilon = \gamma = 0$. Tada se zakon disperzije (spektar dozvoljenih energija) fonona u filmu dobija u obliku:

$$\Theta \equiv \frac{E}{\hbar\Omega} = 2\sqrt{\sin^2\frac{a_x k_x}{2} + \sin^2\frac{a_y k_y}{2} + \sin^2\frac{\pi\mu}{2(N_z+2)}}; \tag{7}$$

$$\Omega = \sqrt{\frac{C}{M}}; \quad \mu = 1,2,...,N_z+1.$$

Ovaj zakon disperzije grafički je predstavljen na Sl. 3, gde je: $R_{xy} = \sin^2\frac{a_x k_x}{2} + \sin^2\frac{a_y k_y}{2}$. Uočljive su diskretne vrednosti mogućih energija.

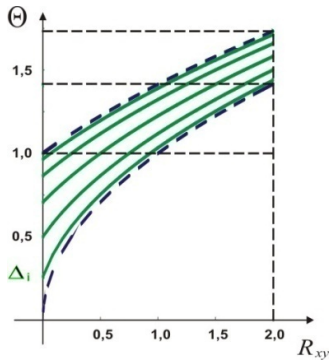

Sl. 3. Zakon disperzije fonona u „idealnom“ filmu
Fig.. 3. Dispersion law of phonons in „ideal“ film

Iako je ovo idealizovan slučaj i udaljen od prakse, on se mora izučiti, iz više razloga. Prvi je taj koji će nam omogućiti već nekakvo zaključivanje, a to je odsustvo kontinualnosti, tj. postojanje izrazite diskretnosti i prebrojive brojnosti energetskih fononskih stanja. Drugi razlog proizilazi iz činjenice – rešenja za GF, da se između dve granične površi ne prostire običan mehanički (zvučni) talas, nego specifičan stojeći, koji ima dvostruko veću amplitudu! Treći razlog je da u proračunima koji slede i koje ćemo morati numerički da rešavamo, imamo „kontrolnu tačku“, kada drastično smanjimo vrednosti graničnih parametara. Dakle, svi ostali – neidealni slučajevi urađeni su numerički, upotrebom programskog paketa *Mathematica*. Grafici su slični onom prikazanom na pređašnjoj Sl. 3, ali se raspored (zelenih) fononskih stanja menja u zavisnosti od veličine graničnih parametara.

Evidentno je i to da u ovakvom sistemu ne mogu da nastanu izolovana, tj. lokalizovana fononska stanja, njihov broj ostaje uvek isti i unutar „balkovskih“ granica, a definisan je brojem kristalnih ravni duž pravca narušenja translacione simetrije.

Nakon ovoga, uobičajenom procedurom [13] određene su srednje vrednosti kvadrata pomeraja i kvadrata impulsa i one su bile date forulama:

$$< u_{\vec{n}}^2 >= \frac{\hbar}{M}\frac{1}{N_x N_y}\frac{1}{N_z+2}\sum_{k_x,k_y}\sum_{\mu=1}^{N_z+1}\frac{1}{\omega_{k_x,k_y,\mu}} \cdot \tag{8}$$

$$\cdot \sin^2(n_z+1)\frac{\pi\mu}{N_z+2}\coth\frac{\hbar\omega_{k_x,k_y,\mu}}{2\Theta};$$

$$< p_{\vec{n}}^2 >= \frac{\hbar M}{N_x N_y (N_z+2)}\sum_{k_x,k_y}\sum_{\mu=1}^{N_z+1}\omega_{k_x,k_y,\mu} \cdot \quad . \tag{9}$$

$$\cdot \sin^2(n_z+1)\frac{\pi\mu}{N_z+2}\coth\frac{\hbar\omega_{k_x,k_y,\mu}}{2\Theta}.$$

Iz dobijenih izraza se vidi da, za razliku od idealne strukture, srednji kadrati pomeraja i impulsa zavise od prostorne koordinate n_z.

Moramo podvući, da je za nas veoma bitno i evidentno da rešenja GF uvek predstavljaju stojeće talase, slično kao kod vazdušnog stuba. Pri tome, trbusi se nalaze na graničnim ravnima filma, što ukazuje da atomi na tim ravnima imaju najveću energiju i amplitudu oscilovanja.

V. Zaključna analiza rezultata

U fononskom podsistemu ultratankih kristalnih filmova, koji je odgovoran, odnosno – koji opisuje mehanička svojstva posmatrane strukture, dolazi do pojave znatno pojačanog oscilovanja i formiranja stojećih talasa. Pojačanim fononskim delovanjem – za očekivati je, i njihovo vrlo intenzivno i pozitivno delovanje na veličinu jon-fonon interakcije, jer najveći deo njihove – mehaničke energije, ide upravo na ovo povećanje. Usled toga može se jasno zaključiti da bi odgovor na pitanje mehanizma za poboljšanje efikasnosti jonskog transporta, upravo mogao da bude u značajnom pozitivnom uticaju vibracija kristalne rešetke prevlaka elektroda na „razbijanje“ klopki koje zarobljavaju jone u graničnom sloju elektroda. Ove znatno jače vibracije – na neki poseban način „razmrdavaju” ili „oživljavaju” jone, i na taj način im stvaraju uslove za brojniji, neometaniji i, u svakom slučaju, mnogo brži transfer kroz elektrolit, sa jedne na drugu elektrodu i nazad.

Istovremeno, svojim znatno ojačanim oscilovanjem, fononi oslobađaju u elektrodama i u zaprečnom međusloju između graničnog sloja elektroda i elektrolita, one „zarobljene” jone koji, bez prisustva predloženih i ovde analiziranih MO prevlaka, ne bi više nikako mogli da učestvuju u prenosu

naelektrisanja i energije između elektroda unutar elektrolita u Li-jonskim baterijama. Na taj način, sistem: elektrode sa ultratankim MO filmovima – u mogućnosti je da značajnije i trajnije povećava efikasnosti Li-jon provođenja.

ZAHVALNICA

Istraživanja čiji su rezultati ovde prezentovani, finanskijski su potpomognuta od Ministarstva za naučnotehnološki razvoj, visoko obrazovanje i informaciono društvo Republike Srpske (Projekti br. 19/6-020/961-2/18, 19/6-020/961-35/18, 19.032/961-36/19 i 19.032/961-42/19).

LITERATURA

[1] J.-M. Tarascon, M. Armand, Nature, 414, (2001) 359-367

[2] P. L. Taberna, S. Mitra, P. Poizot, P. Simon & J.-M. Tarascon, Nature Materials 5, 567 – 573 (2006).

[3] S. Pejovnik, R. Dominko , M. Bele, M. Gaberscek and J. Jamnik, Journal of Power Sources, Vol. 184, Issue 2, 593-597 (2008).

[4] J. Hong, Ch. Wang , U. Kasavajjula, Journal of Power Sources 162 (2006) 1289–1296.

[5] Yoon Seok Jung, Andrew S. Cavanagh,b Anne C. Dillon, Markus D. Groner, Steven M. George, and Se-Hee Leea, Journal of The Electrochemical Society, 157, 1, A75-A81, 2010.

[6] D. Popov, S.K. Jaćimovski, B.S. Tošić, J.P. Šetrajčić, Physica A vol.317, 129-139 (2003).

[7] B.S. Tošić, J.P.Šetrajčić, D.Lj. Mirjanić, Z.V. Bundalo, Physica A vol.184, 354-366 (1992).

[8] S.G. Davison and M. Steslicka: Basic Theory of Surface States, Clarendon , Osford (1996).

[9] M. Prutton: Introduction to Surface Physics, Clarendon, Oxfod (1995).

[10] M. Tkach, V. Holovatsky, O. Voitsekhivska, Physica E vol.11, 17-26 (2001).

[11] V.M. Golovach, G.G. Zegrya, A.M. Makhanets, I.V. Pronishin, N.V. Tkach, Semiconductors, vol.33/5, 564-568 (1999).

[12] J.M.Wesselinowa, Phys.Stat.Sol. (b), vol.223, 737 (2001); vol.229, 1329 (2002).

[13] J.P.Šetrajčić, S.K.Jaćimovski, Review of Results of Theoretical Approaches to Phonon Engineering of Thermodynamic Properties for Different Quantum Structures, *NBP* **20**/3, 67-82 (2015).

[14] J.P.Šetrajčić, S.K.Jaćimovski, D.I.Ilić, Process of Phonon Diffusion through Crystalline Structures, *NBP* **22**/2, 1-12 (2017).

[15] B.S.Tošić, J.P.Šetrajčić, S.K.Jaćimovski: Metodi teorijske fizike, Kriminalističko-policijski univerzitet, Zemun 2018.

[16] M. Mozetič et all: Recent developments in surface science and engineering, thin films, nanoscience, biomaterials, plasma science, and vacuum technology, Thin Solid Films **660**, 120-160 (2018)

[17] B.S. Tošić*:* Statisticka fizika, PMF, Novi Sad (1978).

[18] S. Doniach, E.H. Sondheimer: Green's Functions for Solid State Physicists, Imperial College Press, London (1999).

[19] D.Lj.Mirjanić and J.P.Šetrajčić, Proceedings UNITECH'08 **3**, 566-571 (2008).

[20] C. Kittel, Introduction to Solid State Physics, Wiley, New York (1986).

ABSTRACT

The paper presents the results of theoretical research of the phonon subsystem behavior in ultrathin metal-oxide (MO) coatings when they are applied to electrodes in Li-ion batteries in order to increase the efficiency of ion transport. The method of Green's functions was applied and numerical analysis showed that in ultra-thin films (in direction perpendicular to the boundary surfaces of the film) occur distinctly amplified mechanical oscillation of the crystal lattice and the formation of standing waves, whereby phonons stimulate the release of trapped ions in the boundary layers of the electrodes and with that increase the efficiency of ion transport between the electrodes, and thus contribute to increasing of the electrical conductivity in these batteries.

Increase in the Electrical Conductivity of Li-ions Batteries by Electrode Coating Metal-Oxide Nano-Films

Jovan P. Šetrajčić, Siniša M. Vučenović,
Igor J. Šetrajčić, Stevo K. Jaćimovski,
Ana J. Šetrajčić-Tomić, Dušan I. Ilić, Nikola R. Vojnović

Performanse sklopova termoelektrični modul - hladnjak namenjenih samonapajajućim sistemima u uslovima prirodnog hlađenja

Aleksandra Stojković, *Student Member, IEEE*, Miloš Marjanović, *Student Member, IEEE*, Jana Vračar, *Student Member, IEEE*, Aneta Prijić, *Member, IEEE* i Zoran Prijić, *Member, IEEE*

***Apstrakt*— Sklopovi termoelektrični modul-hladnjak nalaze široku primenu u sistemima za konverziju termičke u toplotnu energiju i obrnuto. U ovom radu je analiziran izabrani termoelektrični modul u ulozi termoelektričnog generatora u sprezi sa šest različitih hladnjaka bliskih dimenzija pod uslovima prirodnog hlađenja. Razmatrana je efikasnost sklopova sa aspekta električnog napona predatog potrošaču pri različitim temperaturnim pobudama. Izvršena su eksperimantalna merenja i odgovarajuće numeričke simulacije, pri čemu su analizirani doprinosi pojedinih termoelektričnih efekata i mehanizama odvođenja toplote sa površina hladnjaka. Pokazano je da ravni hladnjaci od mikroporoznih materijala mogu adekvatno da zamene ekstrudirane aluminijumske hladnjake kod samonapajajućih sistema u uslovima prirodnog hlađenja.**

***Ključne reči*—Termoelektrični generator; hladnjak; samonapajajući sistem; prirodno hlađenje; radijacija.**

I. Uvod

Termoelektrični moduli (TEM-ovi) u sprezi sa različitim tipovima hladnjaka se često susreću kao delovi prenosnih mini uređaja za hlađenje/grejanje ili termoelektrično napajanih bežičnih senzorskih čvorova. Sami moduli baziraju svoj rad na Peltijevom (Peltier) odnosno Zebekovom (Seebeck) efektu. Kada rade kao izvori ili apsorberi toplote termoelektrični moduli se pobuđuju električnom strujom i kao takvi su poznati pod nazivom Peltijevi elementi za grejanje odnosno hlađenje [1]. Analogno, kada se na suprotne strane ovih modula primeni odgovarajuća temperaturna razlika oni generišu električni napon i tada se klasifikuju kao termoelektrični generatori (TEG-ovi) [2]. Za efikasan rad TEM-ova je neophodna dopunska razmena toplote sa njegove hladne i/ili tople strane što se obezbeđuje kako aktivnim tako i pasivnim hladnjacima. S obzirom da su standardni pasivni hladnjaci znatno jednostavnije konstrukcije i bez potrebe za dodatnim podsklopovima za protok rashladnog fluida, oni su široko prisutni u komercijalnim sistemima. Performanse sklopova sa pasivnim hladnjacima, pod definisanim radnim uslovima, osim od karakteristika TEM-a zavise i od konstrukcije i materijala upotrebljenog hladnjaka [3].

Aluminijumski hladnjaci sa ekstrudiranim rebrima ili stubićima su standardno rešenje za primene u kojima se zahteva jednostavno povećanje površine za odvođenje toplote. Hladnjaci od keramike alumine (Al_2O_3) zamenjuju aluminijumske pri zahtevima za visokim probojnim naponima i elektromagnetnom kompatibilnošću i primenjuju se kod LED rasvete, modula snage i specifičnih integrisanih kola [4]. Mikroporozni keramički hladnjaci ravne ili jednostavne rebraste geometrije su niskoprofilni, lagani i bez efekta antene [5]. Njihova mikroporozna struktura obezbeđuje povećanje efektivne kontaktne površine sa fluidom i niski toplotni kapacitet po jedinici zapremine, što ih čini pogodnim za primenu u sistemima gde prevladava prirodno hlađenje (bez strujanja okolnog fluida) unutar ograničenog prostora. Odnedavno komercijalno dostupne hladnjake od bakarne pene takođe karakteriše mikroporozna struktura, kao i dodatna prevlaka od bakar-oksida radi povećanja emisivnosti [6].

Ovaj rad analizira funkcionisanje sklopova TEG-hladnjak prvenstveno za primenu u bežičnim senzorskim čvorovima u uslovima prirodnog hlađenja. Osnovni cilj je da se uporede performanse nestandardnih pasivnih hladnjaka (keramičkih i mikroporoznih) sa aluminijumskim hladnjacima bliskih spoljašnjih dimenzija. Osim vrednosti generisanog napona na potrošaču, prati se i vremenski odziv sklopa na iznenadnu termičku pobudu, odnosno njegova termička inertnost. Sva eksperimentalna merenja prate numeričke simulacije sa ciljem uspostavljanja standardizovane procedure za predviđanje karakteristika novoprojektovanih sklopova.

II. Eksperimentalna postavka

Razmatraju se komercijalno dostupne komponente tako da je izabran tipičan „minijaturni“ TEG GM200-127-14-16 sa 127 termoelektričnih parova, spoljašnjih dimenzija (40×40×3,8) mm [4]. Karakteristični električni parametri ovog TEG-a su dati u Tabeli I. Na hladnu stranu TEG-a je termoprovodnom adhezivnom trakom pričvršćen hladnjak. Analizirno je šest niskoprofilnih hladnjaka čije su osnove dimenziono kompatibilne sa pločama TEG-a a izrađeni su od aluminijuma, alumine, mikroporozne keramike i bakarne pene. Parametri izabranih hladnjaka su navedeni u Tabeli II.

Aleksandra Stojković – Univerzitet u Nišu, Elektronski fakultet, Aleksandra Medvedeva 14, 18000 Niš, Srbija (e-mail: aleksandra.stojkovic@elfak.ni.ac.rs).

Miloš Marjanović – Univerzitet u Nišu, Elektronski fakultet, Aleksandra Medvedeva 14, 18000 Niš, Srbija (e-mail: milos.marjanovic@elfak.ni.ac.rs)

Jana Vračar – Univerzitet u Nišu, Elektronski fakultet, Aleksandra Medvedeva 14, 18000 Niš, Srbija (e-mail:jana.vracar@ elfak.ni.ac.rs)

Aneta Prijić – Univerzitet u Nišu, Elektronski fakultet, Aleksandra Medvedeva 14, 18000 Niš, Srbija (e-mail: aneta.prijic@elfak.ni.ac.rs)

Zoran Prijić – Univerzitet u Nišu, Elektronski fakultet, Aleksandra Medvedeva 14, 18000 Niš, Srbija (e-mail: zoran.prijic@elfak.ni.ac.rs)

Eksperimentalna postavka koja obezbeđuje automatizovanu kontrolu radnih uslova i merenje napona predatog od strane TEG-a potrošaču je šematski prikazana na Sl. 1. Sklop je termoprovodnom trakom fiksiran za površinu grejača u horizontalnom položaju a ceo sistem je okružen zaklonom koji obezbeđuje uslove prirodnog hlađenja. Grejač generiše toplotnu pobudu, pri čemu se njegova temperatura, koja je ujedno i temperatura tople strane TEG-a (T_{hot}), zadaje po predefinisanim vrednostima nekoliko desetina °C višim od temperature okoline (T_{amb}). S obzirom da nije moguće direktno merenje temperature hladne strane TEG-a (T_{cold}), kao kontrolni parametar se prati temperatura površine hladnjaka (T_{hs}). Električni izvodi TEG-a su vezani za programabilno aktivno opterećenje koje istovremeno predstavlja potrošač promenljive vrednosti (R_L) i ima ulogu multimetra. Sve vrednosti temperatura se prate pomoću računarom vođenih digitalnih multimetara.

TABELA I
KARAKTERISTIČNI ELEKTRIČNI PARAMETRI TEG-A GM200-127-14-16

Maksimalna snaga - P_{max}	4,73 W
Maksimalna struja - I_{max}	1,19 A
Maksimalni napon – U_{max}	3,98 V
Unutrašnja otpornost - R_{TEG}	2,1 Ω

TABELA II
GEOMETRIJSKI PARAMETRI RAZMATRANIH HLADNJAKA

Oznaka hladnjaka	Geometrija	Materijal	Dimenzije L×W×H mm
HS1	110 stubića	aluminijum	40×40×10
HS2	100 stubića	aluminijum	40×40×5
HS3	121 stubić	alumina	42×42×12
HS4	7 niskih rebara	mikroporozna keramika	40×40×5,25
HS5	ravan	mikroporozna keramika	40×40×2,5
HS6	ravan	bakarna pena	40×40×5

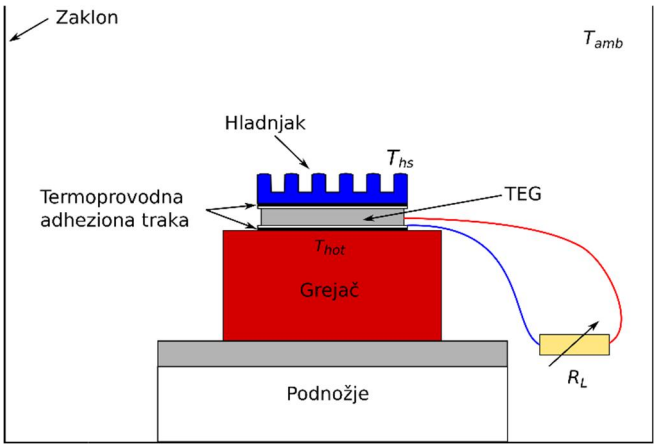

Sl. 1. Šematski prikaz eksperimentalne postavke za kontrolu radnih uslova sklopa i merenje temperature i napona na potrošaču.

Grejač se postavlja na željenu temperaturu i prati promena T_{hot} kao i napon otvorenog kola TEG-a (V_{oc}). Kada sistem uđe u termičku ravnotežu, uključuje se aktivno opterećenje koje obezbeđuje otpornost u opsegu od 2 Ω do 5 Ω sa korakom od 1 Ω (od veće ka manjoj vrednosti). Ove otpornosti odgovaraju ulaznoj otpornosti tipičnog kola za upravljanje energijom u samonapajajućim sistemima. Za svaku zasebnu vrednost otpornosti potrošača meri se vrednost pada napona na njemu (V_L) i struje kroz kolo (I_L). Zatim se isključuje aktivno opterećenje i kada se napon otvorenog kola vrati na stacionarnu vrednost ponavlja se ciklus za sledeću temperaturu grejača. S obzirom da je opterećenje direktno vezano za TEG, električne veličine zadovoljavaju relaciju:

$$V_L = R_L I_L = V_{TEG} - R_{TEG} I_L = \\ = N\alpha_{pn}(T_{hot} - T_{cold}) - R_{TEG} I_L, \quad (1)$$

gde je N broj termoelektričnih parova a α_{pn} Zebekov koeficijent materijala TEG-a.

III. POSTAVKA SIMULACIJE

Postavka simulacije u potpunosti prati eksperimentalnu postavku sa Sl. 1. Elementi sklopa i okruženje su modelirani u CAD softveru [7] i uvezeni u simulator za numeričku multifizičku analizu metodom konačnih elemenata [8]. Simulira se stacionarno stanje pri odgovarajućoj temperaturnoj pobudi primenom modula za rešavanje problema u spregnutom termo-električnom i domenu dinamike fluida. Simulacioni domen obuhvata okolni fluid (vazduh) dovoljnih dimenzija da granični uslovi odgovaraju uslovima prirodnog hlađenja. Sa gornje strane je domen otvoren kako bi se dozvolilo slobodno odvođenje toplote.

Model TEG-a obuhvata 127 termoelektričnih spojeva (parova Bi_2O_3 nožica n- i p-tipa) redno povezanih bakarnim kontaktima i smeštenih između dve ploče od alumina keramike. Geometrija hladnjaka je modelirana detaljno, dok su grejač i podnožje pojednostavljeni. Termoprovodna adheziona traka se, usled male debljine, smatra idealnim termičkim kontaktom. Grejač obezbeđuje konstantan dotok toplote kao uslov termičkog opterećenja dok eksterni otpornik vezan za izvode TEG-a predstavlja električno opterećenje. Uključeni mehanizmi prenosa toplote su provođenje kroz čvrste i mikroporozne strukture, laminarno strujanje zagrejanog fluida pod dejstvom gravitacije i radijacija. U uslovima prirodnog hlađenja, radijacija ima značajan doprinos odvođenju toplote sa elemenata sklopa kako putem direktnog zračenja površine ka ambijentu tako i putem indirektnog zračenja od jedne ka drugoj površini [9]. Automatski kreirana inicijalna simulaciona mreža je naknadno poboljšana u okolini dodirne površine hladnjaka sa vazduhom, tako da tipična mreža sadrži 400.000-500.000 diskretizacionih elemenata.

Specifični geometrijski i parametri materijala TEG-a i hladnjaka, neophodni za realizaciju simulacije, dati su u Tabeli III i Tabeli IV, respektivno. Naglašava se da su ukupan Zebekov koeficijent, specifična električna otpornost i specifična termička provodnost Bi_2Te_3 nožica temperaturno

zavisni parametri [10]. Kod mikroporoznih hladnjaka, usled složene strukture uslovljene postojanjem otvorenih pora, za proračun efektivnih vrednosti specifične termičke provodnosti, specifičnog toplotnog kapaciteta, kao i efikasnosti protoka fluida, softver koristi vrednosti koeficijenta poroznosti i permeabilnosti [11].

TABELA III
GEOMETRIJSKI I PARAMETRI MATERIJALA TEG-A

Dimenzije nožica - l×w×h (mm)	1,4×1,4×1,6
Dimenzije Cu kontakta (mm)	4,2×1,4×0,3
Debljina ploče od alumine (mm)	0,8
Ukupan Zebekov koeficijent termopara α_{pn} (μV/K)	$1{,}22\cdot10^{-5}\times T^3$-$0{,}021\times T^2$+$10{,}23\times T$-1081
Specifična električna otpornost termopara (10^{-5} Ωm)	$-1{,}48\cdot10^{-5}\times T^2$+$0{,}017\times T$-2,78
Specifična termička provodnost termopara (W/mK)	$3{,}96\cdot10^{-5}\times T^2$-$0{,}026\times T$+5,84

TABELA IV
PARAMETRI MATERIJALA RAZMATRANIH HLADNJAKA

Parametar	Materijal			
	Aluminijum	Alumina	Mikroporozna keramika	Bakarna pena
Gustina (kg/m^3)	2700	3660	1800	3320
Specifična termička provodnost (W/mK)	201	25	125	45
Specifični toplotni kapacitet (J/kgK)	900	880	670	385
Poroznost (%)	-	-	30	63
Permeabilnost (m^2)	-	-	$0{,}54\cdot10^{-10}$	$5{,}32\cdot10^{-8}$
Emisivnost	0,85	0,6	0,6	0,7

IV. REZULTATI I DISKUSIJA

Tipičan rezultat eksperimentalnog merenja na sklopu sa hladnjakom HS4 je prikazan na Sl. 2. Na sklop se primenjuje iznenadna termička pobuda $\Delta T=T_{hot}-T_{amb}$=20 °C koja stvara temperaturnu razliku na stranama TEG-a a time se generiše napon otvorenog kola $V_{oc}=V_{TEG}$. Ovakva pobuda odgovara uslovima hladnog starta u samonapajajućim sistemima. U prvom trenutku postoji premašenje napona koje nastaje usled termičke inertnosti sklopa [12] i ono lagano opada kako se sklop zagreva i pune njegove termičke kapacitivnosti [13]. Kada sklop uđe u stabilno stanje uključuje se aktivno opterećenje tako da kroz TEG protiče struja I_L a vrednost merenog napona V_L prati relaciju (1). Treba napomenuti da je napon V_{TEG} pri uslovima proticanja struje manji od V_{oc} usled izraženog delovanja Peltijevog efekta koji povećava temperaturu hladne a smanjuje temperaturu tople strane, odnosno smanjuje efektivnu temperaturnu razliku na TEG-u [10]. Smanjenje napona je izraženije pri većim temperaturnim razlikama ΔT i nižim vrednostima R_L usled viših vrednosti I_L. Ovaj fenomen se može kvalitativno uočiti pri isključenju aktivnog opterećenja kod sklopova sa aluminijumskim hladnjacima jer su oni manje inertni i lakše se oslobode toplote generisane Peltijevim efektom.

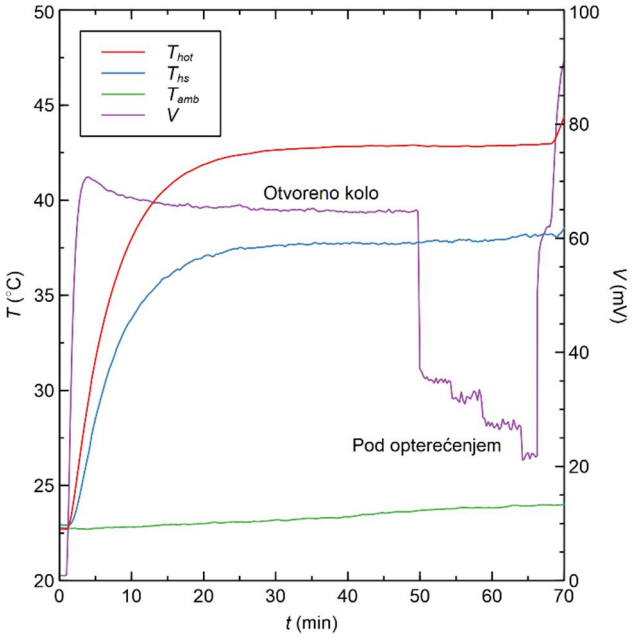

Sl. 2. Eksperimentalne vrednosti temperature na sklopu sa HS4 i napona na potrošaču za $\Delta T=T_{hot}-T_{amb}$=20 °C.

Temperaturna raspodela dobijena simulacijom za sklop sa HS4 pri $\Delta T=T_{hot}-T_{amb}$=40 °C i bez električnog opterećenja TEG-a je prikazana na Sl. 3. Jasno se uočava raspodela temperature kroz nožice i na hladnoj strani TEG-a kao i profil strujanja toplog vazduha sa hladnjaka, odnosno oblik perjanice. Simulacijama je uočeno da efekat radijacije, značajno doprinosi izgledu raspodele i vrednostima temperature na elementima sklopa.

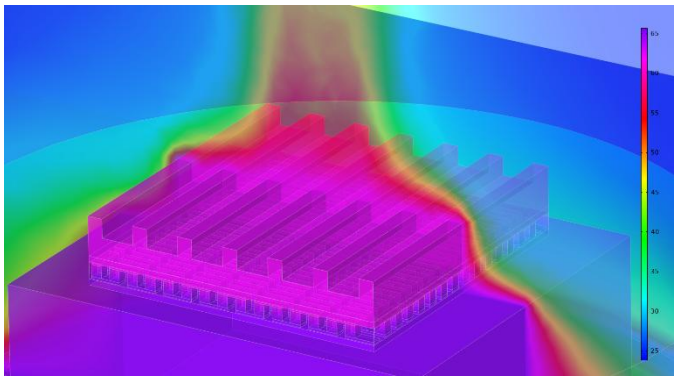

Sl. 3. Raspodela temperature na sklopu sa HS4 i okolnom fluidu dobijena simulacijom pri $\Delta T=T_{hot}-T_{amb}$=40 °C i pri otvorenom kolu.

Rezultati eksperimentalnih merenja i simulacija su predstavljeni u vidu zavisnosti napona V_{oc} od temperaturne razlike $\Delta T=T_{hot}-T_{amb}$ na Sl. 4 i Sl. 5. Opseg temperaturnih razlika je karakterističan za najčešće dostupne razlike u temperaturi grejača i okoline kod samonapajajućih sistema. Rezultati simulacije veoma dobro prate rezultate eksperimentalnih merenja. Maksimalno odstupanje kod aluminijumskih i alumina hladnjaka je 6% dok je kod mikroporoznih hladnjaka 10%, prvenstveno zbog nemogućnosti softvera da adekvatno simulira efekte indirektne radijacije kod ovakvih materijala. Napominje se da, obično zanemarivana, radijacija utiče čak do 30% na vrednost generisanog napona dobijenu simulacijama.

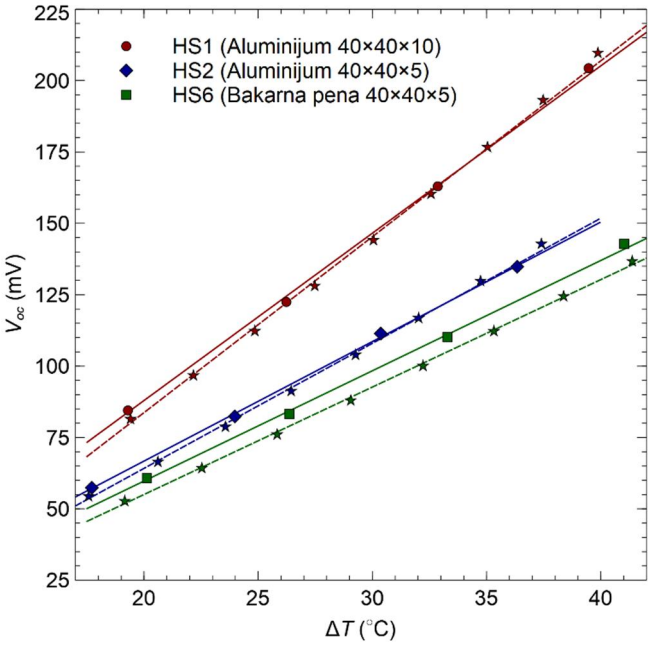

Sl. 4. Zavisnost napona otvorenog kola od temperaturne razlike $\Delta T=T_{hot}-T_{amb}$ za sklopove sa hladnjacima od aluminijuma i bakarne pene. Simboli i pune linije – eksperiment; zvezdice i isprekidane linije - simulacije.

Hladnjaci HS1 i HS3 daju najviše vrednosti napona za ceo opseg razmatranih temperaturnih razlika, što je i očekivano s obzirom da imaju najveći broj i visinu stubića ali oni zauzimaju najveću zapreminu. Uočava se da hladnjaci HS2 i HS4, bliskih spoljašnjih gabarita, imaju skoro identičnu efikasnost. Ovo je značajno jer je HS2 ekstrudirani aluminijumski hladnjak, složene geometrije a HS4 od mikroporozne keramike, niskoprofilni i jednostavne geometrije. Mikroporozni ravni hladnjaci HS5 i HS6 su skoro jednakih performansi. Pri tome, debljina i poroznost hladnjaka od keramike je dvostruko manja u odnosu na hladnjak od bakarne pene. Kvantitativnim poređenjem karakteristika hladnjaka HS2 i HS6, uočava se da aluminijumski hladnjak daje približno 10% više napone, što ne predstavlja prevelik doprinos. Istovremeno, analiza rezultata za mikroporozne keramičke hladnjake HS4 i HS5, ukazuje da dvostruko veća debljina hladnjaka poboljšava performanse za svega 8%. Opšti zaključak je da u uslovima prirodnog hlađenja, a uzevši u obzir gabarite i složenost geometrije, keramički materijali (alumina i mikroporozna keramika) pokazuju najbolju efikasnost. Ravni hladnjaci od bakarne pene se takođe mogu uspešno primeniti u uslovima prirodnog hlađenja. Evidentno je da stubići kod ekstrudiranih hladnjaka poboljšavaju efikasnost prevashodno kod hlađenja uz postojanje strujanja okolnog fluida.

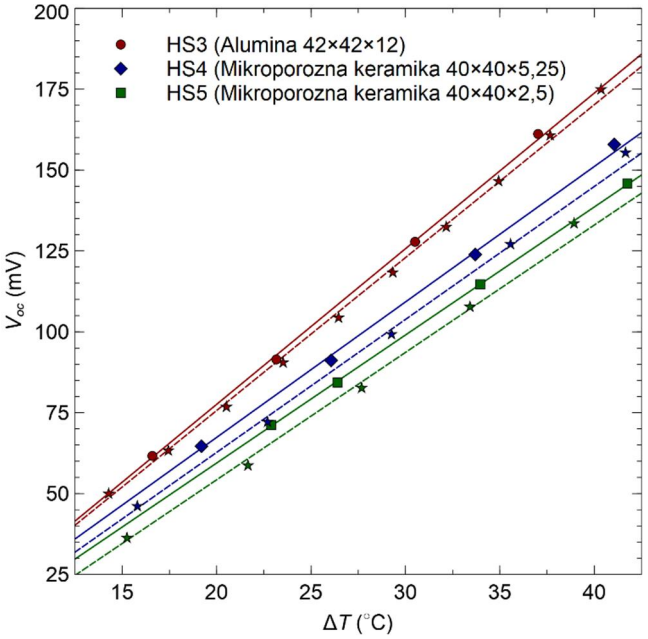

Sl. 5. Zavisnost napona otvorenog kola od temperaturne razlike $\Delta T=T_{hot}-T_{amb}$ za sklopove sa hladnjacima od alumine i mikroporozne keramike. Simboli i pune linije – eksperiment; zvezdice i isprekidane linije - simulacije.

Zavisnost napona na potrošaču V_L od temperaturne razlike za sklop sa rebrastim hladnjakom od mikroporozne keramike (HS4) i pri različitim vrednostima aktivnog opterećenja R_L je prikazana na Sl. 6. Rezultati omogućavaju kvantitativnu procenu uticaja Peltijevog efekta na vrednost generisanog napona. U odnosu na vrednost V_L koja bi se dobila raspodelom V_{oc} na otpornostima R_L i R_{TEG}, ovaj efekat doprinosi njenom smanjenju za 22% do 36% u zavisnosti od ΔT i R_L, što je u saglasnosti sa ranijim analizama termoelektrično napajanih senzorskih čvorova [14].

V. Zaključak

Analiza performansi sklopova TEM-hladnjak treba da obezbedi jednostavniji proces projektovanja sistema koji se na njima baziraju. U ovom radu je akcenat stavljen na primene u termoelektrično napajanim bežičnim senzorskim čvorovima gde moduli imaju ulogu generatora i to pod najnepovoljnijim uslovima rada tj. pri prirodnom hlađenju. Posvećena je pažnja i radu sklopova pod opterećenjem koji odgovaraju realnom funkcionisanju senzorskog čvora. Tada dolazi do izražaja Peltijev efekat koji smanjuje vrednost efektivno generisanog napona čak do 36%. Simulacije su pokazale i da efekat radijacionog zračenja uvećava vrednost generisanog napona do 30%. Uočava se da keramički hladnjaci, bilo čvrsti ili mikroporozni, pokazuju najbolje performanse za data geometrijska ograničenja. Rezultati analize mogu potpuno analogno da se primene i na mini sisteme za hlađenje/grejanje.

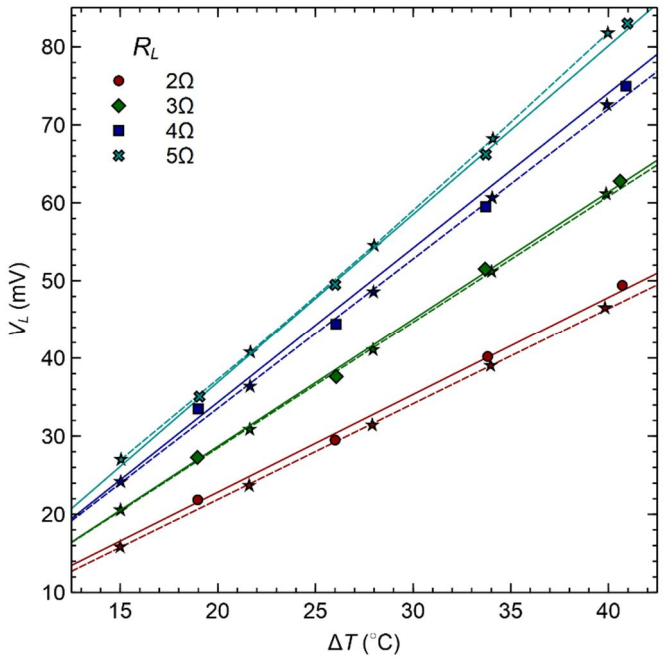

Sl. 6. Zavisnost napona na potrošaču od temperaturne razlike $\Delta T=T_{hot}-T_{amb}$ za sklop sa HS4. Simboli i pune linije – eksperiment; zvezdice i isprekidane linije - simulacije.

ZAHVALNICA

Ovaj rad je realizovan u okviru projekta finansiranog od strane Ministarstva za prosvetu, nauku i tehnološki razvoj Republike Srbije (Ev. br. 451-03-9/2021-14/200102).

LITERATURA

[1] H. J. Goldsmid,."Thermoelectric Modules and Their Application", in *Introduction to Thermoelectricity. Springer Series in Materials Science*, vol 121. pp. 197-220, Springer, Berlin, Heidelberg, 2016.

[2] N. Jaziri, A. Boughamoura, J. Müller, B. Mezghani, F. Tounsi, M. Ismail, „A comprehensive review of Thermoelectric Generators: Technologies and common applications", *Energy Reports*, vol. 6, Suppl. 7, pp. 264-287, 2020.

[3] M. Baldry, V. Timchenko, C. Menictas, „Optimal design of a natural convection heat sink for small thermoelectric cooling modules", *Appl. Therm. Eng.*, vol. 160, 114062, Sept., 2019.

[4] European Thermodynamics Ltd, https://www.europeanthermodynamics.com/

[5] AMEC Thermasol, https://amecthermasol.co.uk/datasheets/MPC%20Ceramic%20Series.pdf

[6] Versarien Technologies Ltd, http://www.versarien-technologies.co.uk/.

[7] FreeCAD 3D parametric modeler, https://www.freecadweb.org.

[8] ANSYS Inc., Multiphysics simulation, https://www.ansys.com/products/platform/multiphysics-simulation.

[9] A. Sarkar, S. Mahapatra, "Role of surface radiation on the functionality of thermoelectric cooler with heat sink", *Appl. Therm. Eng.*, vol. 69, no. 1-2, pp. 39-45, Aug. 2014.

[10] M. Liao, Z. He, C. Jiang, X. Fan, Y. Li, F. Qi, „A three-dimensional model for thermoelectric generator and the influence of Peltier effect on the performance and heat transfer", *Appl. Therm. Eng.*, vol. 133, pp. 493-500, March, 2018.

[11] J. Wang, J. Carson, M. North, D. Cleland, „A new approach to modelling the effective thermal conductivity of heterogeneous materials", *Int. J. Heat Mass Transf.*, vol. 49, no. 17-18, pp. 3075-3083, Aug. 2006.

[12] N. Nguyen, K. Pochiraju, „Behavior of thermoelectric generators exposed to transient heat sources", Appl. Thermal Eng., vol. 51, no. 1, pp.1-9, Mar., 2013.

[13] M. Marjanović, A. Prijić, B. Randjelović, Z. Prijić, „A transient modeling of the thermoelectric generators for application in wireless sensor network nodes", *Electronics-MDP*I, vol. 9, 1015, Jun. 2020.

[14] A. Prijić, M. Marjanović, Lj. Vračar, D. Danković, D. Milić, Z. Prijić, „A Steady-State SPICE Modeling of the Thermoelectric Wireless Sensor Network Node", Proc. of the 4th IcETRAN, Kladovo, Serbia, pp. MOI2.3.1-6, June 05-08, 2017.

ABSTRACT

Thermoelectric module-heatsink assemblies are widely used in systems converting thermal into electrical energy and vice versa. In this paper, performances of the selected thermoelectric module in conjunction with six different heatsinks of similar dimensions under natural cooling conditions are analyzed. The efficiency of the assemblies is determined by the value of the voltage transferred to the electric load at different temperature loads. Experimental measurements and appropriate numerical simulations were performed, and the contributions of individual thermoelectric effects and heat dissipation mechanisms were analyzed. It is shown that flat heatsinks made of microporous materials can adequately replace extruded aluminum heatsinks in energy harvesting systems under natural cooling conditions.

Performances of the thermoelectric module-heatsink assemblies for energy harvesting under natural cooling

Aleksandra Stojković, Miloš Marjanović, Jana Vračar, Aneta Prijić, Zoran Prijić

Analiza uporednog praćenja temperature površine ohlađenih materijala pri njihovom zagrevanju do ambijentalne temperature

Stevan Đenadić, Ljubiša Tomić, Vesna Damnjanović i Katarina Nestorović

***Apstrakt*—U datom eksperimentalnom radu su termografskim metodama ispitivane termofizičke karakteristike različitih materijala. Za ispitivanja su izabrani mesingani niovčić, ugalj i pelet, jer imaju različita termoizolaciona svojstava i različito stanje površine. Uzorci su najpre hlađeni, a zatim je njihovo zagrevanje na sobnoj temperaturi praćeno termalnom kamerom. U drugom delu eksperimenta, korišćena je impulsna termografija, a zagrevanje površine uzoraka vršeno je svetlosnom pobudom.**

***Ključne reči*—termografija; impulsna termografija; nedestruktivno testiranje materijala; mesing; ugalj; pelet.**

I. Uvod

Metode infracrvene termografije koje se koriste za otkrivanje zagrejanih tela, beskontaktnu procenu temperature površine objekata i nedestruktivno testiranje materijala, danas imaju široku primenu ne samo u bezbednosnom sektoru već i u mnogobrojnim privrednim i naučnim granama [1,2]. Još neke mogućnosti primene termografskih metoda odnose se na praćenje procesa neželjenog zapaljenja pojedinih gasova, tečnosti, lako zapaljivih čvrstih supstanci, ali i na praćenje procesa sagorevanja materijala različitih kalorijskih vrednosti [3-6]. Širokoj rasprostranjenosti termografskih metoda, doprinele su sve pristupačnije cene odgovarajuće komercijalne opreme.

II. Test uzorci

Kao uzorak broj 1 izabran je novčić od pet dinara [7]. Na njegovoj prednjoj strani je brojem i slovima oznaka nominalne vrednosti, a na njegovoj zadnjoj strani je reljef manastira Krušedol i oznaka godine kovanja. Prečnik novčića je 24 mm a masa 5,78 g. Novčić je višeslojni. Jezgro je izrađeno od legure niskougljeničnog čelika. Obostrano je dvostruko presvučen galvanskom prevlakom, i to prvim slojem bakra (do jezgra), i drugim slojem mesinga (na površini). Mesing kao legura bakra i cinka široko se koristi ne samo u kovnici novca za prevlaku apoena, već i u elektrotehnici, kao konstruktivni ukrasni materijal, za izradu muzičkih instrumenata, i dr. Mesing koji se koristi za kovanice (oznaka: CuZn49) sadrži 65% bakra i 35% cinka. Gustina mu je 8,7 g/cm^3, specifični toplotni kapacitet 380 J/(kg ^{o}C), toplotni kapacitet po jediničnoj zapremini 3,2 J/(cm^3 ^{o}C), toplotna provodnost 130 W/(m ^{o}C), koeficijent toplotne difuzije 32×10^{-6} m^2/s, a poseduje i antibakterijsko dejstvo. Mesingana legura koja je na površini novčića je termoprovodni materijal, neravna je ali je reljef pravilnih oblika.

Kao uzorak broj 2, izabran je pljevaljski ugalj [3], koji spada u kategoriju visokokaloričnog mrkog lignita. Njegova kalorijska vrednost (toplotna moć) se kreće u granicama od 15424 kJ/kg do 14021 kJ/kg. Ugalj je po svojoj prirodi nehomogeni materijal. Ovu vrstu uglja karakteriše izuzetno mali sadržaj sumpora, nizak procenat vlage i pepela, a granulacija ove vrste uglja je od 40 mm do 80 mm. Masa uzorka iznosila je oko 3,5 g. Ugalj je termoizolacioni materijal a njegova površina je hrapava.

Za uzorak broj 3, izabran je bukov pelet [6]. Pelet je čvrsto gorivo u vidu briketa koje se dobija u specijalnim presama koje rade na principu kompresije prethodno prerađenog materijala. Materijal se sastoji od 70% tvrdog drveta i 30% mekog drveta. U procesu proizvodnje, drvo se najpre usitnjava, zatim se separira u krupnu i sitnu piljevinu (brašno) i skladišti u velike silose, odakle se kao pripremljena drvena smeša presuje u pelet. Briketi su valjkastog oblika, visina valjka je do 4 cm, a prečnik do 6,1 mm. Gustina bukovog peleta je 6,36 g/cm^3, toplotna moć je 17300 kJ/kg a masa po briketu je približno 2,97 g. Pelet je termoizolacioni materijal a površina briketa je glatka.

III. Eksperimentalna postavka

U prvom delu eksperimenta primenjena je metoda pasivne termografije. Sva tri uzorka, najpre su postavljena na izolacioni materijal od plastike (fotografija prikazana na slici 1.) a zatim hlađena zajedno sa njim u zamrzivaču. Nakon jednog sata, uzorci na plastičnoj podlozi izneti su iz zamrzivača i postavljeni na sto za snimanje termalnom kamerom FLIR S60.

Neposredno nakon hlađenja, u nastavku eksperimenta, snimljena je serija termograma u odgovarajućim vremenskim intervalima, sa ciljem praćenja zagrevanja ohlađenih uzoraka, različitih termofizičkih svojstava sve do ambijentalne

Stevan Đenadić–Univerzitet u Beogradu, Rudarsko-geološki fakultet, Đušina 7, 11000 Beograd, Srbija (e-mail: stevan.djenadic@rgf.bg.ac.rs)
Ljubiša Tomić–Vojnotehnički institute, Ratka Resanovića 1, 11030 Beograd, Srbija (e-mail: ljubisa.tomic@gmail.com)
Vesna Damnjanović–Univerzitet u Beogradu, Rudarsko-geološki fakultet, Đušina 7, 11000 Beograd, Srbija (e-mail: vesna.damnjanovic@rgf.bg.ac.rs)
Katarina Nestorović–Vojnotehnički institute, Ratka Resanovića 1, 11030 Beograd, Srbija (e-mail: katarina.nestorovic933@gmail.com)

temperature. Temperatura ambijenta, mereno termografski, iznosila je 21 °C.

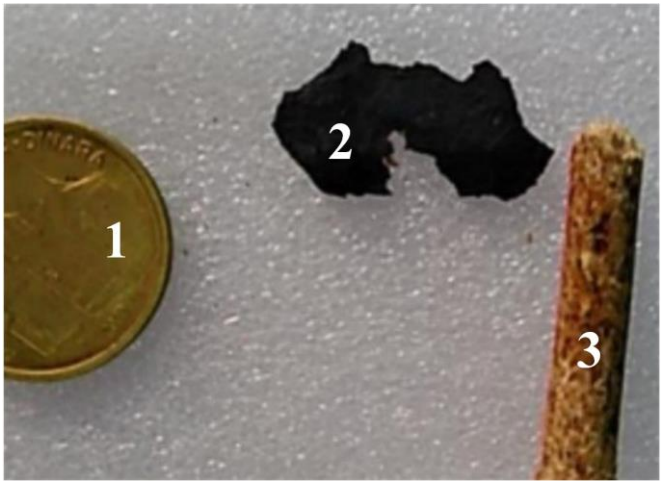

Sl. 1. Fotografija uzoraka postavljenih na termoizolacionom materijalu od plastike

U drugom delu eksperimenta, za ispitivanja je primenjena metoda impulsna termografija (PT – *Pulse thermography*), koja spada u metode aktivne termografije. Pobuda uzoraka je impulsna - svetlosnim fluksom u kratkom vremenskom intervalu. Naime, u eksperimentalnoj postavci sada je, pored termalne kamere FLIR S60, kao impulsni svetlosni izvor za osvetljavanje uzoraka (za zagrevanje njihovih površina) korišćen fotografski blic YASHICA CS-250AF. Trajanje i intenzitet svetlosnog impulsa je kalibrisano [8]. Dakle, uzorci nisu bili hlađeni, ali je jedan od uzoraka (briket od peleta), pre snimanja, jednim delom, bio neko vreme potopljen u vodi. Briket peleta je i posle kraćeg sušenja bio po dužini homogeno vlažan.

IV. Rezultati i diskusija

Eksperiment je osmišljen tako da se "uporedo" pod "istim uslovima" prate promene temperatura površina ohlađenih materijala sve do njihovog zagrevanja do ambijentalne temperature. Cilj je bio da se utvrdi brzina promene temperature (zagrevanja) u zavisnosti od termofizičkih svojstava uzoraka, sa ciljem da se potom izvrši procesiranje snimljenih termograma u infracrvenom programskom paketu ThermaCAM Researcher 2.9 i analiza praćenja zagrevanja.

Na slici 2, prikazan je termogram iste scene kao i na slici 1 (u vidljivoj oblasti elektromagnetskog spektra), nastale u istom trenutku kao i termogram u infracrvenoj oblasti elektromagnetnog spektra (8–14 μm). Termogram prikazan na slici 2 snimljen je neposredno posle iznošenja iz zamrzivača (oko 1 minut kasnije), nakon čega su, u nastavku eksperimenta, snimljeni termogrami u određenim vremenskim intervalima sa ciljem praćenja "zagrevanja" ohlađenih uzoraka sve do ambijentalne temperature. Uzorci su bili izloženi početnim stacionarnim uslovima dovoljno dugo da dođe do uspostavljanja termičke ravnoteže. Naglim pomeranjem uzoraka iz stacionarnog temperaturnog stanja (pothlađenog) u odnosu na ambijentalnu temperaturu, tj. sa niže na višu ambijentalnu temperaturu, dolazi do zagrevanja uzoraka.

Procesi zagrevanje uzoraka nisu identični, iako su isti eksperimentalni uslovi, usled njihovih različitih termofizičkih svojstava. Na brzinu zagrevanja uzoraka uticali su različiti faktori - pre svega njihova fizička svojstva, ali i parazitni toplotni izvori, čiji je uticaj više dolazio do izražaja kod glatkih (refleksivnih) površina. Naime novčić ima reljefnu ali refleksivnu površinu, pa parazitna refleksija njegove površine stvara lažnu sliku o pravoj radijacionoj temperaturi njegove površine. Dok kod uzorka sa višim koeficijentom emisivnosti a niskim koeficijentom refleksije (tj. kod ugalja i briketa od peleta) parazitna refleksija slabije utiče na radijacionu temperaturu površine.

Na termogramu predstavljenom na slici 2, radi termografske procene njihove radijacione temperature, markirane su tri oblasti označene kao: Bx1, Bx2, i Bx3. Prosečna temperatura uzorka 1 (novčić) iznosila je 7,2 °C. Masa novčića znatno je različita od masa uzorka peleta i uzorka uglja. Prosečna temperatura uzorka 2 (ugalj) iznosila je - 3,6 °C. Prosečna temperatura uzorka 3 (pelet) iznosila je - 4,4 °C.

Na istom termogramu, uočljiva je i refleksija toplih predmeta u okolini koja je dominantna na površini visokorefleksionog materijala (novčića) prekrivenog slojem blage kondenzacije vlage iz okolnog vazduha na hladnoj površini.

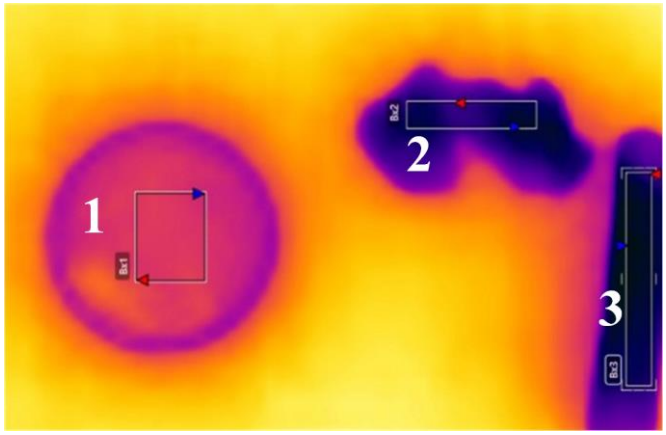

Sl. 2. Termogram uzoraka postavljenih na izolacioni materijal od plastike (ista scena kao na Sl. 1.)

Ispitivanja na osnovu snimljenih termograma ukazuju da se ponašanje ohlađenih uzoraka različitih termofizičkih svojstava, u odnosu na topliju okolinu ambijenta, tokom vremena odvija svojstveno fizičkoj prirodi materijala.

Na slici 3 prikazana je fotografija uzoraka u formatu *thermal blending* zajedno sa termogramom uzoraka u istoj sceni. Istovremeno su prikazane i slika snimljena video kamerom i termogram snimljen termalnom kamerom, jer se radi o različitim objektivima koji su pomereni prostorno za oko 1 cm od centra do centra otvora jednog i drugog objektiva. Upravo iz tog razloga su u horizontalnoj ravni

pomerene slike uzoraka (rastojanja jednog i drugog sočiva objektiva od ravni scene).

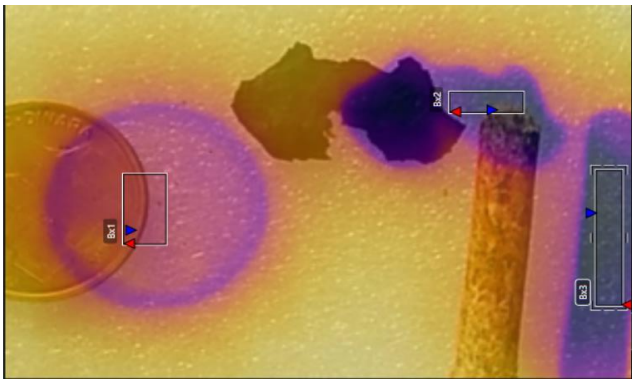

Sl. 3. Fotografija (*format thermal blending*) uzoraka postavljenih na plastičnom izolacionom materijalu i termogram iste scene

Na slici 4 prikazan je termogram (flir_20210527T15:18:30) uzoraka postavljenih na plastičnom izolacionom materijalu na kome su povučene marker linije radi određivanja temperaturnog profila, obeležene kao Li1-novčić, Li2-ugalj, i Li3-pelet.

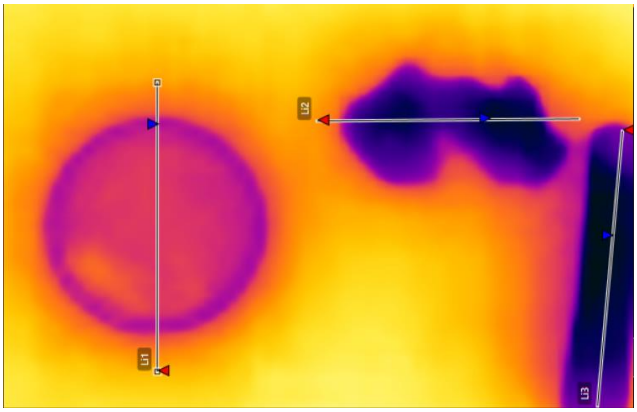

Sl. 4. Termogram uzoraka postavljenih na plastičnom materijalu na kome su povučene marker linije radi određivanja temperaturnog profila

Temperaturni profil duž marker linija Li3 povučene preko briketa peleta prikazan je na slici broj 5.

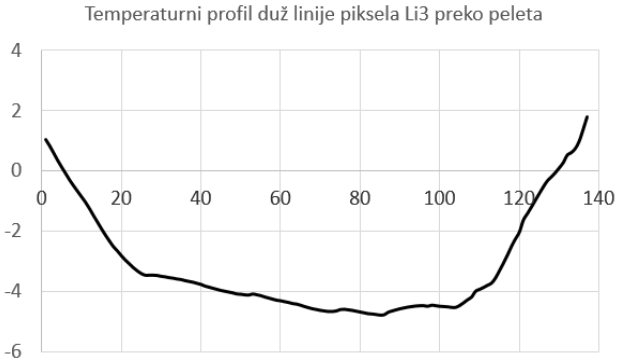

Sl. 5. Temperaturni profil duž marker linije Li3 (na Sl. 4) ohlađenog uzorka briketa peleta snimljen na početku zagrevanja na sobnoj temperaturi

Na slici 6 prikazan je termogram (flir_20210527T15:19:23) snimljen 53 s nakon iznošenja uzoraka iz zamrzivača. Sa navedenog termograma se očitava da je srednja temperature mesinganog novčića 10,7 ºC, a temperature komada uglja pljevlja 10,0 ºC, što je za 0,7 ºC niže od temperature novčića. Dakle, uočava se da je temperatura uglja niža od temperature mesinganog novčića.

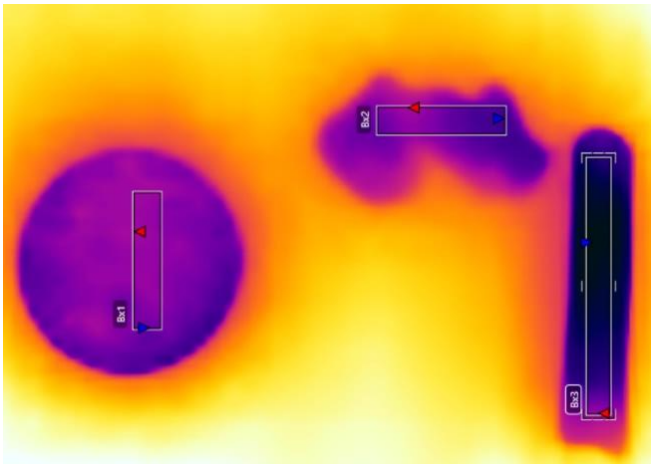

Sl. 6. Termogram uzoraka snimljen 53 s nakon hlađenja

Na slici 7 prikazan je termogram (flir_20210527T15:20:06) snimljen 96 s kasnije nakon hlađenja, tj. 43 s kasnije u odnosu na termogram prikazan na slici 6. Sa navedenog termograma se očitava da srednja temperature mesinganog novčića iznosi 13,2 ºC, a temperature komada uglja 14,4 ºC, što je za 1,2 ºC više od temperature novčića.

Uočava se da je sada prikazan „obrnut slučaj“, tj. temperatura uglja je viša od temperature mesinganog novčića. Dakle, može da se zaključi da zbog visokorefleksivne mesingane prevlake novčić sporije prima toplotu od okoline. Viši koeficijent emisivnosti ima ugalj pljevlja u odnosu na novčić presvučen mesinganom prevlakom.

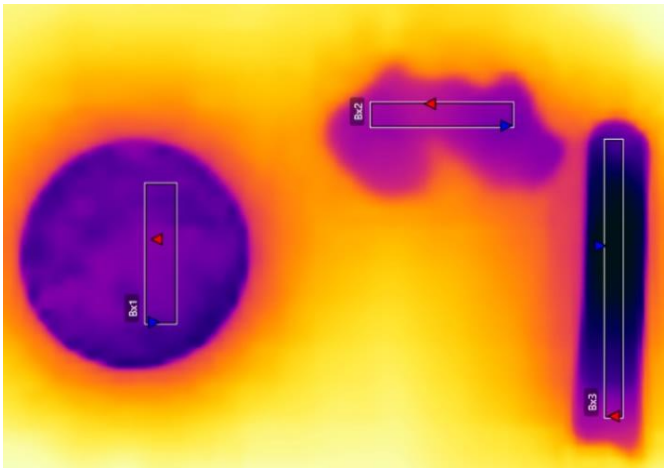

Sl. 7. Termogram uzoraka snimljen 96 s nakon hlađenja

Očigledno da od oko 70-te sekunde od početka zagrevanja, pa do 170-te sekunde, dolazi do isparavanja filma vodene pare na novčiću i sporije apsorpcije toplote iz okoline u odnosu na ugalj. Na slici 8, termogram (flir_20210527T15:23:44) nastao 280 s nakon hlađenja, vodena para je isparila sa njegove površine (novčić se osušio), pa do izražaja dolazi (dominantna je) njegova visokorefleksivna prevlaka na površini, u odnosu na parazitnu refleksiju zračenja toplih predmeta iz okoline scene (na primer tople ruke ekperimentatora).

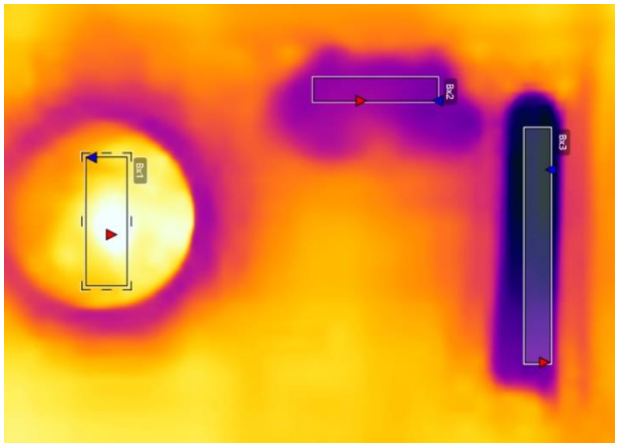

Sl. 8. Termogram nastao 280 s nakon hlađenja

Na slici 9 predstavljen je grafik zavisnosti temperature od vremena pri zagrevanju hlađenog uzoraka: novčića T_1, uglja T_2 i peleta T_3. Početne temperature uzorka uglja i peleta su – 3,6°C i – 4,4°C respektivno – radi se o toplotnim izolatorima sa visokim vrednostima emisivnosti. Početna temperaturu novčića je 7,2 °C – radi se o toplotnom provodniku visokorefleksivne površine pa na njega veliki uticaj ima parazitno zračenja okoline.

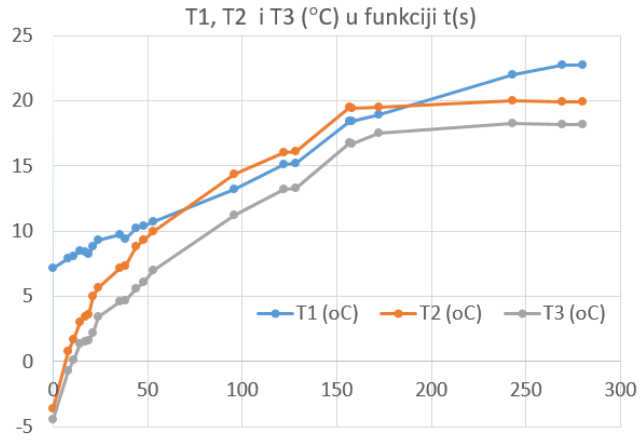

Sl. 9. Zavisnost temperature od vremena pri zagrevanju hlađenog uzorka: novčić – plava serija T1; ugalj – narandžasta serija T2; i peleta – siva serija T3

U tabeli broj 1 navedeni su rezultati termografskog merenja temperature tokom vremena u procesu zagrevanja hlađenih uzoraka 1, 2, i 3 do sobne temperature.

TABLE I
RAST TEMPERATURE TOKOM VREMENA U PROCESU ZAGREVANJA HLAĐENIH UZORAKA (NOVČIĆ – T_1; UGALJ – T_2; I PELET – T_3)

	t (s)	T_1 (°C)	T_2 (°C)	T_3 (°C)
flir_20210527T15:18:30	0	7.2	-3.6	-4.4
flir_20210527T15:18:38	8	7.9	0.8	-0.7
flir_20210527T15:18:41	11	8.1	1.7	0.1
flir_20210527T15:18:44	14	8.5	3	1.4
flir_20210527T15:18:47	17	8.4	3.4	1.5
flir_20210527T15:18:49	19	8.2	3.6	1.6
flir_20210527T15:18:51	21	8.8	5	2.2
flir_20210527T15:18:54	24	9.3	5.7	3.4
flir_20210527T15:19:05	35	9.7	7.2	4.6
flir_20210527T15:19:08	38	9.4	7.3	4.7
flir_20210527T15:19:14	44	10.2	8.8	5.6
flir_20210527T15:19:18	48	10.4	9.3	6.1
flir_20210527T15:19:23	53	10.7	10	7
flir_20210527T15:20:06	96	13.2	14.4	11.2
flir_20210527T15:20:32	122	15.1	16	13.2
flir_20210527T15:20:38	128	15.2	16.1	13.3
flir_20210527T15:22:07	157	18.4	19.5	16.8
flir_20210527T15:22:08	158	18.4	19.4	16.7
flir_20210527T15:22:22	172	18.9	19.5	17.5
flir_20210527T15:23:07	243	22	20	18.3
flir_20210527T15:23:33	269	22.7	19.9	18.2
flir_20210527T15:23:44	280	22.7	19.9	18.2

U drugom delu eksperimenta, u merenjima je primenjena PT termografija. Na slici 10 prikazan je termogram površine drvenog peleta i uglja dok su u termodinamičkoj ravnoteži, tj. neposredno "pre" okidanja blica.

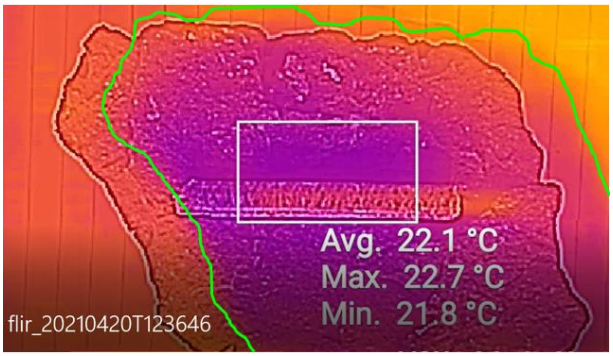

Sl. 10. Termogram površine drvenog peleta i uglja neposredno pre okidanja blica

Na slici 11 prikazan je termogram površine peleta i uglja pola sekunde nakon osvetljavanja blicem, tj. nakon primanja toplotnog impulsa. Nakon okidanja blica dolazi do generisanja površinski homogenog toplotnog impulsa, koji se procesom toplotne difuzije prostire kroz materijale, usled čega dolazi do temperaturne perturbacije na površini uzoraka. Toplotni impuls koji se formirao na nehomogenoj površini uglja, prostire se kroz uzorak različito, u zavisnosti od sastava uglja,

to jest koeficijenta difuzivnosti, na primer čistog uglja i uglja sa više primesa gline. Toplije i hladnije oblasti na površini uglja su nastale usled heterogenog sastava uglja (više i manje gline), razlike u emisivnosti oblasti sa glinom i čistog uglja, gde je apsorbovano više energije od svetlosnog impulsa. Pelet je homogenije zagrejan pošto je kompaktnijeg od uglja koji je „ljuspastog“ sastava. Deo potapanog briketa peleta, iako ponovo suv, bio je hrapaviji od dela peleta koji nije potapan u vodu (tj. hrapavije površine), što znači da mu je hrapavost površine degradirana trajno pa ima promenjenu emisivnost. Na termogramu se za uzorak 3 (pelet) u donjem delu uočava svetlija površina koja odgovara delu uzorka koji je bilo potopljena u vodu kratko vreme, nakon čega se osušio ali sa degradacijom koeficijenta emisivnosti u odnosu na nepokvašeni gornji deo koji nije bio u dodiru sa vodom.

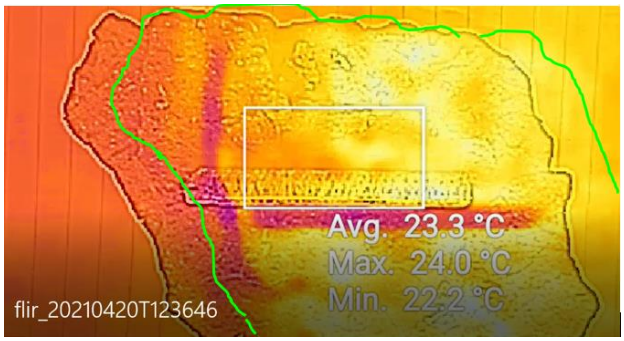

Sl. 11. Termogram površine drvenog peleta i uglja pola sekunde nakon osvetljavanja blicem

Dati rad je pionir ideje da se utvrdi može li se termografija koristi i za grubu procenu kalorijske vrednosti uglja, zasnovanoj na vremenskoj promeni površinske temperature. Inače, utvrđivanje kalorijske vrednosti uglja, koji u termoelektranama Srbije pokriva oko 80% proizvodnje električne energije, je izuzetno složen proces. Propisan je ISO standardom B.H8 318:1972 koji dozvoljava mernu nesigurnost u proceni čak iznad 20 % [9]. Vrednost toplotnog kapaciteta uzorka jeste povezana sa promenom temperature površine, ali da bi se utvrdila veza i sa njegovom kalorijskom vrednošću, treba izvršiti merenja sa uzorcima potpuno istih masa i oblika, uz uzimanje u obzir svih navedenih uticaja u datom eksperimentu, ali i njihovu minimizaciju kroz dizajn eksperimenta.

V. Zaključak

Rezultati predstavljeni u radu, dobijeni na osnovu analize termograma pri proučavanju različitih materijala kako pasivnom tako i aktivnom impulsnom termografijom sa ciljem procene njihovih termofizičkih svojstava. Pri istim uslovima, snimani su uzorci sačinjeni od materijala potpuno različitih termofizičkih karakteristika, i to mesingani novčić, ugalj i pelet. Navedeni materijali su izabrani jer imaju različita termoizolaciona svojstava i različito stanje površine. Termogrami nastali pasivnom metodom, tokom procesa prirodnog zagrevanja (na sobnoj temperaturi), prethodno ohlađenih uzoraka od različitih materijala (termoprovodnih i termoizolacionih) ukazuje na to da termografske metode mogu biti alternativna metoda u proceni termofizičkih svojstava materijala. Problemi koji javljaju pri praćenju promena temperature površina uzoraka kada se primenjuje metoda aktivne impulsne termografije nastaju usled nehomogene strukture (konkretno, naglašene nehomogenosti sastava uglja, hrapavosti površine i nepravilnog oblika) mogu biti svedeni na minimum izborom homogenih, pravilno obrađenih komada (uzoraka) istih oblika.

Zahvalnica

Rad je nastao uz podršku Ministarstva prosvete, nauke i tehnološkog razvoja Republike Srbije - kontakt broj: 451-03-9/2021-14/200126.

Literatura

[1] X. P. Maldague, *Theory and Practice of Infrared Technology for Nondestructive Testing*, John Wiley & Sons, New York, USA, 2001.
[2] G. Gaussorgues, *Infrared Thermography*. English language edition. Springer-Science, Berlin, Germany, 1994.
[3] S. Đenadić, V. Damnjanović, P. Jovančić, D. Ignjatović, D. Jovković, F. Miletić, “Primena termografije u rudarstvu”, IX Međunarodna konferencija Ugalj 2019, Zlatibor, Srbija, s. 57-66, 23-26 Oktobar 2019.
[4] S. Đendić, Lj. Tomić, V. Damnjanović, P. Jovančić, D. Jovković, „Testing the energy value of different types of coal by the method of Active Thermography”, 9th International scientific conference on defensive technologies OTEH 2020, Belgrade, Serbia, pp. 424-428, 15-16 October 2020.
[5] Lj. Tomić; M. Milinović: Experimental research of limits for thermal modulation transfer function,*Thermal Science*, vol. 13, no. 4, pp. 119 – 128, 2009.
[6] Ljubiša Tomić., Vesna Damnjanović., Katarina Mišković., Boban Bondžulić., Dragan Knežević., Aleksandar Kovačević. (2018) Analiza uticaja temperature materijala na primenu metode impulsne termografije. *ETRAN 2018* (*62. konferencija za elektroniku, telekomunikacije, računarstvo, automatiku i nuklearnu fiziku*). *Zbornik radova*, MO. s. 314-318, 11-14. jun, Palić, Srbija.
[7] Народна банка Србије www.nbs.rs/sr_RS/novac-i-p
[8] Lj. D. Tomić, „Nondestructive evaluation of the thermophysics properties materials by IR thermography“, Ph.D. dissertation, School of Electrical Engineering, University of Belgrade, Serbia, 2013.
[9] *Solid mineral fuels – Determination of gross calorific value by bomb calorimetric method and calculation of net calorific value*, SRPS ISO 1928:2015 https://iss.rs/en/project/show/iss:proj:47873

Abstract

In the given experimental work, thermophysical characteristics of different materials were examined by thermographic methods. Brass coin, coal, and pellets were chosen for the tests - because they have different thermal insulation properties and different surface condition. The samples were first cooled and then let to be warmed to room - temperature was continuously being recorded by a thermal camera. In the second part of the experiment, pulsed thermography was used, and the surface of the samples was heated by light excitation.

Analysis of comparative monitoring of surface temperature of cooled materials during their heating to ambient temperature

Stevan Djenadic, Ljubisa Tomic, Vesna Damnjanovic, Katarina Nestorovic

Synthesis and characterization of thin copper coatings obtained by sonoelectrodeposition method

Ivana Mladenović, Jelena Lamovec, Stevan Andrić, Miloš Vorkapić, Marko Obradov, DanaVasiljević-Radović, Vesna Radojević and Nebojša D. Nikolić

***Abstract*—Influence of an intensity of ultrasonic mixing of electrolyte in a temperature range of 27–37 °C and ultrasonic power intensity in the range of 3.77–18.84 W/cm^2 (10–50 %) on a synthesis of fine-grained copper deposits was examined. Copper coatings were electrodeposited on a brass substrate in direct current (DC) regime with an applied current density of 50 mA·cm^{-2}. The laboratory-made copper sulfate electrolyte was used without or with addition of additives. The variation of temperature under sonoelectrodeposition process and variation mixing intensity of electrolyte were ensured by using an ultrasonic probe. The produced Cu coatings were examined by optical microscope (OM) in order to observe the microstructural modification with variation ultrasonic parameters and for measuring imprints of Vickers indenter. The micro hardness properties of composite systems were characterized using Vickers micro indentation test. The composite hardness models Chicot-Lesage and Chen-Gao were used for the determination the coatings hardness and adhesion evaluation. Application of Atomic Force Microscopy (AFM) technique also confirmed the strong influence of ultrasonic mixing conditions of electrolyte onto change of the microstructure of copper deposits and surface roughness of the coatings. The maximum hardness, good adhesion properties and minimum micro surface roughness was obtained for the fine-grained Cu coating produced with amplitude of 50 % ultrasonic mixing of electrolyte without additives and 30 % for electrolyte with additives.**

***Index Terms*— ultrasonic probe; microindentation; composite system; coatings; adhesion; sonoelectrodeposition.**

I. Introduction

THE effects of ultrasonic electrolyte mixing can be seen from a few aspects: chemical, mechanical and theirs combination. The chemical effects of ultrasound are due to the "implosion of microbubbles", generating free hydroxyl radicals [1, 2] with high chemical reactivity, while mechanical effects are caused by "shock waves" formed during symmetric cavitation or by "microyets" formed during asymmetric cavitation [1]. The use of ultrasound in a reaction system provides specific activation based on a physical phenomenon, known as "acoustic cavitation". Cavitation is caused by a longitudinal sound wave, which results in a change in local pressures and temperatures in the liquid electrolyte [2]. The change in pressure causes the gas bubbles to form and burst, which contributes to electrolyte mixing [3]. The scheme of the mechanism of formation, growth and bursting of bubbles under ultrasound conditions are shown in Fig. 1.

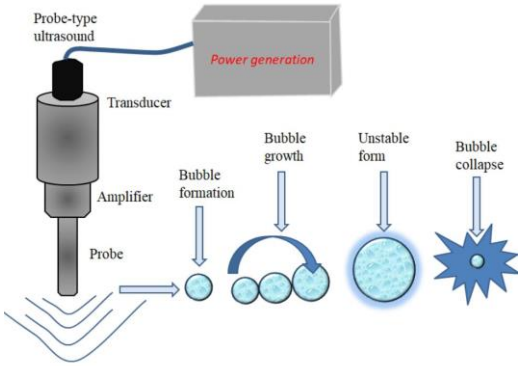

Fig. 1. Schematic presentation of bubble implosion under ultrasonic conditions in electrolyte near cathode surface [3].

Electrodeposition in presence of ultrasound (US-ED) may have effects in terms of: degradation of the reaction, enhanced electrochemical diffusion processes and mass-transport, increase electrochemical rates and current efficiencies, decrease electrode overpotentials [4]. The effects of ultrasonic mixing of electrolyte and influence on the metallic coatings properties have also reported in the literature: change morphology (reduction in grain size or change grain orientation), influence on residual stress, that hence good adhesion and hardness, the increase of brightness has been also observed, etc [4–7]. Ultrasonic deposition (sonoelectrodeposition) is often used in combination with the co-deposition of particles as reinforcement into a metal matrix composite [8].

Using AFM technique, the coating surface roughness was investigated in function of grow rate (applied current density) [9], film thickness (deposition time), variation substrates and mixing conditions [10], as well as variation electrolytes [10, 11].

Ivana Mladenović, Stevan Andrić, Miloš Vorkapić, Marko Obradov, Dana Vasiljević-Radović and Nebojša Nikolić are with the Institute of Chemistry, Technology and Metallurgy, University of Belgrade, Njegoševa 12, 11 000 Belgrade, Serbia (e-mail: ivana@nanosys.ihtm.bg.ac.rs), (e-mail: stevan@nanosys.ihtm.bg.ac.rs), (e-mail: worcky@nanosys.ihtm.bg.ac.rs), (e-mail: marko.obradov@nanosys.ihtm.bg.ac.rs), (e-mail: dana@nanosys.ihtm.bg.ac.rs), (e-mail: nnikolic@ihtm.bg.ac.rs).

Jelena Lamovec is with the University of Criminal Investigation and Police Studies, Cara Dušana Street 196, 11 000 Belgrade, Serbia (e-mail: jelena.lamovec@kpu.edu.rs).

Vesna Radojević is with the Faculty of Technology and Metallurgy, University of Belgrade, Karnegijeva 4, 11 000 Belgtrade, Serbia (e-mail: vesnar@tmf.bg.ac.rs).

Hardness and adhesion testing are the most important and widely used methods for assessing the structural and mechanical properties of the composite systems and coatings [12]. If the thickness of the coating is very small, the influence of the substrate must be considered during the coating hardness determination [13] and mathematical composite hardness models are used for this purpose [14–19].

Hence, the present experiment aims here to find the synergistic effects of ultrasound agitation, temperature oscillation, while increasing the power of ultrasonic mixing influence on the roughness, adhesion and micro hardness of copper coatings.

II. COMPOSITE HARDNESS MODELS

Multilayer complex structures such as thin coatings (films) on bulk substrates are often used in fabrication of MEMS devices. A thin coating deposited electrochemically on a conductive substrate can be considered as a composite system. Determination of the hardness of the coating, independent of the influence of the substrate hardness, is not possible in the entire region of the applied indentation loads. For this reason, composite hardness mathematical models are used to estimate the absolute hardness of a thin coating [14–19], and two adequate ones have been selected in this paper. The composite hardness model of Chicot-Lesage (C–L) was found to be suitable for experimental data analysis (for composite hardness values, H_c) and coating hardness determination (H_{coat}) based on our previous research [14–16]. Using this model, it is possible to calculate the absolute value of the coating hardness for each individual indentation load. The model is based on Meyer's law which expresses the variation of the size of the indent (d) in function of the applied load (P) [13]:

$$P = a^* \cdot d^{n^*} \tag{1}$$

The variation part of the hardness number with load is represented by the factor n^*. Chicot-Lesage adopted the following expression [16]:

$$F\left(\frac{\delta}{d}\right) = \left(\frac{\delta}{d}\right)^m = f \quad where\ m = \frac{1}{n^*} \tag{2}$$

In equation (2) m is the composite Mayer's index, d is average diagonal size of Vickers indent and δ is coating thickness. The value of m is calculated by a linear regression performed on all the experimental data obtained for a given coating/substrate couple and deduced from the relation [13]:

$$\ln d = m \cdot \ln P + b \tag{3}$$

The composite hardness can be expressed by the following relation [13, 16]:

$$H_C = (1-f)/\left(1/H_s + f \cdot \left(\frac{1}{H_{coat}} - \frac{1}{H_s}\right)\right) + \\ + f \cdot \left(H_s + f \cdot (H_{coat} - H_s)\right) \tag{4}$$

Hardness of the film is the positive root of the next equation [13, 16]:

$$A \cdot H_{coat}^2 + B \cdot H_{coat} + C = 0, \quad with \\ A = f^2 \cdot (f-1) \\ B = \left(-2 \cdot f^3 + 2 \cdot f^2 - 1\right) \cdot H_s + (1-f) \cdot H_c \\ C = f \cdot H_c \cdot H_s + f^2 \cdot (f-1) \cdot H_s^2 \tag{5}$$

With the known value of m, only the hardness of the films remains to be calculated. The values of composite hardness and substrate hardness (H_s) are the values obtained by measuring on a Vickers tester.

For the evaluation of the adhesion properties of thin films and absolute film hardness, Chen–Gao (C–G) model was chosen [17–19]. This method introduces the composite hardness as the function of the critical reduced depth beyond which the material will have no effect on the measured hardness. The critical reduced depth, represents ratio between the radius of the plastic zone beneath the indentation and indentation depth [12, 17–19]. The large value of the critical reduced depth corresponds to good adhesion, while low values indicate poor adhesion of the films. The correlation between composite hardness value H_c and the critical reduced depth b are found as [12, 17–19]:

$$H_c = H_s + \left[\frac{(n+1)\cdot\delta}{n \cdot b \cdot h}\right] \cdot (H_{coat} - H_s) \tag{6}$$

H_s and H_{coat} are the hardness of the substrate and of the film, respectively, δ is film thickness, h is indentation depth, n is the power index and b is the critical reduced depth. The convenient value of n is found to be 1.8 for "soft film on hard substrate" and n = 1.2 for "hard film on soft substrate" [12, 17–19]. It is first necessary to perform the fitting of the composite hardness depending on the depth of indentation according to the model shown in the equation (7) [18]:

$$H_c = A + B \cdot \frac{1}{h} + C \cdot \frac{1}{h^{n+1}} \tag{7}$$

A, B and C are fitting parameters, and h is indentation depth. Indentation depth can be calculated as 1/7 of diagonal size. Then coating hardness can be expressed as [18]:

$$H_{coat} = A \pm \sqrt[n]{\frac{\left[n \cdot |B| / (n+1)\right]^{n+1}}{n \cdot |C|}} \tag{8}$$

The equation used to estimate adhesion properties coating/substrate composite system has the following form [12]:

$$H_c = \frac{7 \cdot (n+1) \cdot (H_s - H_{coat})}{n \cdot b} \cdot \frac{\delta}{d} \tag{9}$$

III. EXPERIMENTAL

A. Preparation of electrolyte and samples

Copper was electrodeposited from an aqueous solution of copper sulfate and sulfuric acid without (electrolyte I) and with added additives (electrolyte II). The composition of the electrolytes used in experiments is given in Table 1. Three different additives were used for electrolyte II: polyethylene glycol (PEG, molecular weight 6000), Na-3-mercapto-1-propane sulfonic acid (MPSA) and NaCl, based on the suggested recipe found in the reference [20]. The volume of the electrolyte for all experiment was 100 ml. Brass foil, ½ hard, (ASTM B36, K&S Engineering), 250 µm thick was us as cathode. Pure copper foil, cylindrical shape, was used as anode (see Fig. 2).

TABLE I
COMPOSITION OF THE ELECTROLYTES

Electrolyte I	g/l	Electrolyte II	g/l
$CuSO_4 \cdot 5\,H_2O$	240	$CuSO_4 \cdot 5H_2O$	240
H_2SO_4	60	H_2SO_4	60
		PEG 6000	1
		MPSA	0.0015
		NaCl	0.1240

An ultrasonic cleaner (model HD 2200 Bandelin / Germany) of 20 kHz ± 500 Hz frequency (f_s) equipped with a standard sonotrode (probe of 13 mm tip diameter), with power (I) of 200 W in continuous mode was used for sonication and mixing of electrolyte. In general, power intensity I_i (power irradiance) represents power, I, distributed over surface area, S (sonotrode tipe surface) as shown as $I_i = I / S$ [W/cm^2]. The temperature change, T_i, of the electrolytes was observed during the operation of the ultrasound probe with the variation of the amplitude range, P_i. The temperature change of the electrolyte was measured every 5 minutes (see Table II). Electrochemical deposition was performed under DC galvanostatic mode. The current density values were maintained at 50 mA·cm^{-2}; deposition time was fixed at 15 minutes and coating thickness was calculated according to Faraday's law.

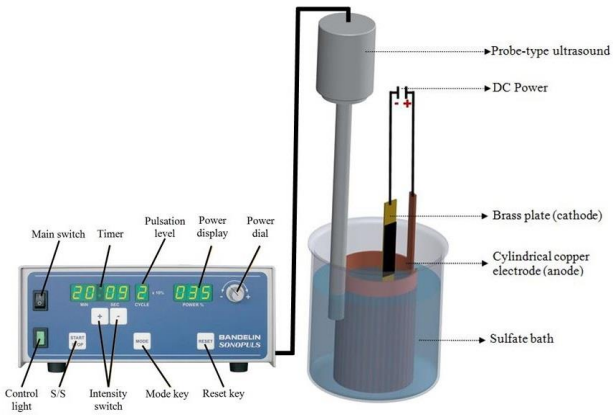

Fig. 2. Experimental setup for a sonoelectrochemical deposition process.

TABLE II
THE PARAMETERS OF THE SONOELECTRODEPOSITION

No.	P_i / %	electrolyte	t_i / min	T_i / °C
1	10	I	1	28.8
			5	29.7
			10	30.4
			15	32.2
3	30	I	1	28.3
			5	29.6
			10	30.6
			15	35
5	50	I	1	28.9
			5	30.9
			10	33.2
			15	37.2
3'	30	II	1	27
			5	28.1
			10	30.5
			15	31.5

B. Optical microscopy

The structural properties of Cu coatings were examined by optical microscope (OM)–model Motic AE-2000 MET. A metallographic microscope–Carl Zeiss Epival Interphako was used to measure the diagonal size of Vickers indents.

C. Topography of the Cu coatings

The surface topography and roughness of the Cu coatings were examined using atomic force microscope (AFM, TM Microscopes-Vecco) in the contact mode. The values of the arithmetic average of the absolute roughness parameters (R_a) of the surface height deviation, were measured from the mean image data plane, using free software Gwyddion [21]. The values of R_a roughness parameter, calculated as average from three independent measurements at different locations of one sample of copper surface obtained by the DC regime with variation of ultrasonic intensity mixing and electrolyte composition. The scanned area was 20 µm^2 in contact mode.

D. Mechanical characterization

The mechanical properties of the composite systems were characterized using Vickers microhardness tester "Leitz, Kleinharteprufer DURIMET I" with loads ranging from 2.452 N down to 0.049 N. Three indentations were made at each indentation load from which the average diagonal and composite hardness could be calculated.

IV. RESULT AND DISCUSSION

A. Structural characterization of the Cu coatings

Fig. 3 shows morphologies of the Cu coatings obtained using sonoelectrodeposition method with ultrasonic amplitude at 10 % (Fig. 3a), 30 % (Fig. 3b), 50 % (Fig. 3c) from electrolyte I.

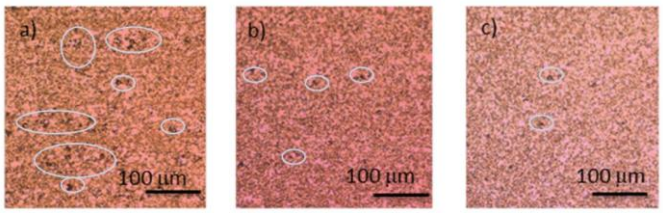

Fig. 3. Microscopic images of Cu coatings obtained in sonoelectrodeposition regime on a brass substrate from electrolyte I. The sonoelectrodeposition parameters are: j = 50 mA·cm^{-2}, t = 15 min, δ = 16.61 µm, T_{av} = 31.6 °C and f_s = 20 kHz with variation of the amplitude range of ultrasonic mixing: a) P_i = 10 %, b) P_i = 30 % and c) P_i = 50 %.

The smaller number of different size of cavitation holes were observed (Fig. 3a). It has been observed that the number of holes decreases with increasing intensity of ultrasonic mixing of the electrolyte (Figs. 3b and 3c). The bursting of large gas bubbles caused by the mixing of electrolytes at the low intensity, leads to the formation of micro cavities on the surface of the coating (Fig. 1).

B. The roughness analysis of the Cu coatings

The AFM surface areas of Cu coatings produced under different conditions are shown in Fig. 4. The average values of the roughness parameters (R_a) obtained by application of *Gwyddion* free software are given in Table III. The average roughness can be calculated as:

$$R_a = \frac{1}{N_x \cdot N_y} \sum_{i=1}^{N_x} \sum_{j=1}^{N_y} \left| z(i,j) - z_{mean} \right| \qquad (10)$$

where N_x and N_y are the number of scaning points on the *x*-axis and *y*-axis; *z(i, j)* is the height of the *(i, j)* measuring point, z_{mean} is the mean hight of all measuring points [22].

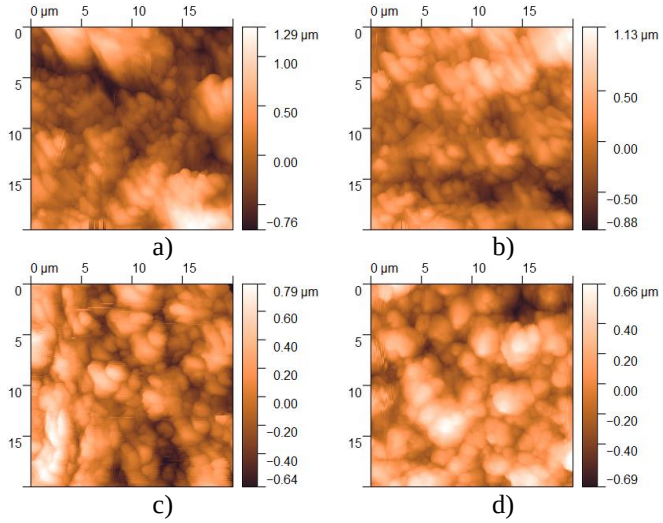

Fig. 4. 2D-AFM images of copper deposits prepared on brass substrate obtained in DC-US regime. The sonoelectrodeposition parameters are: j = 50 mA·cm^{-2}, t = 15 min, δ = 16.61 µm, T_{av} = 31.6 °C and f_s = 20 kHz with variation of the amplitude range of ultrasonic mixing: a) P_i = 10 %, b) P_i = 30 % and c) P_i = 50 % for electrolyte I and d) P_i = 30 % for electrolyte II.

Based on the results in Table III and Fig.4, a decrease in the roughness of the Cu coating from electrolyte I was observed with increasing mixing intensity (Fig. 4a–c).

The copper coating obtained from the electrolyte with additives and 30 % applied ultrasound amplitude hads minimal roughness (see Fig. 4d).

TABLE III
THE VALUES OF ROUGHNESS PARAMETER FOR SONOELECTRODEPOSITION COPPER COATINGS WITH VARIATION ULTRASONIC AMPLITUDE AND ELECTROLYTE

No.	P_i %	electrolyte	R_a / nm
1	10 %	I	270
3	30 %	I	230
5	50 %	I	180
3’	30 %	II	148.8

C. Composite hardness of copper coatings/brass systems.

The average values of the indent diagonal d (in µm), were calculated from several independent measurements on every specimen for different applied loads P (in N). The absolute substrate hardness and composite hardness values, H_c (in GPa) were calculated using the formula [23]:

$$H_c = 0.01854 \cdot P \cdot d^{-2} \qquad (11)$$

where 0.01854 is a constant, geometrical factor for the Vickers indenter.

Fig. 5 shows the variation in composite hardness values with relative indentation depth (h/δ =RID), where h is indentation depth ($h = d/7$) for copper coatings deposited from electrolyte I with change applied ultrasonic amplitude percent.

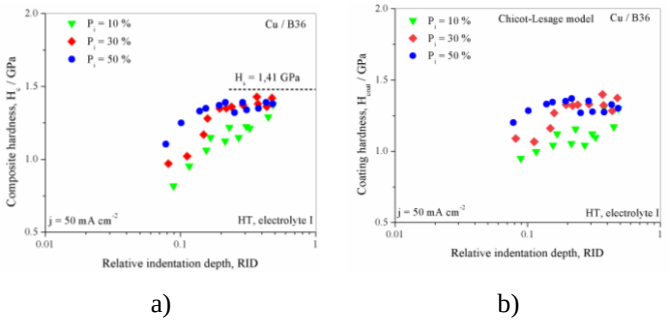

Fig. 5. Variation hardness vs. relative indentation depth for the copper coatings deposited on brass substrates with variation ultrasonic mixing of electrolyte: a) composite hardness and b) hardness of the coating calculated according to Chicot-Lesage model. The current density and deposition time were 50 mA·cm^{-2} and 15 min. Electrolyte I was used.

The effect of changing the intensity of the ultrasonic mixing of the electrolytes is reflected in the change values of the composite system hardness and the coating hardness. An increase in composite hardness with increasing electrolyte mixing was observed. The maximum value of the composite hardness was obtained for the copper coating deposited with the 50 % ultrasound mixing electrolyte (Fig. 5a) and the

minimum value for the 10 %. The results of the calculated coating microhardness according to the C-L model more clearly indicate the influence of the applied ultrasound mixing condition on the microstructure and the hardness of the coating, and the highest coating microhardness value was obtained for the 50 % ultrasound amplitude settings (Fig. 5b). For shallow indentation penetration depth ($0.1 \leq RID \leq 1$), it was found that the response was that of the coating and substrate together. Based on the results from: Fig. 3c), Table III (sample 5), Fig. 4c and Fig. 5a,b conclude that a 50 % ultrasound amplitude is an optimal condition for copper ultrasonic deposition from electrolyte I.

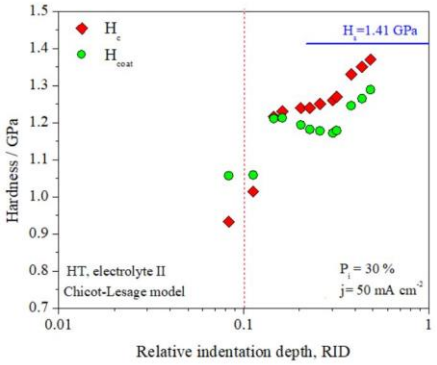

Fig. 6. Variation hardness vs. relative indentation depth for the copper coatings deposited on brass substrates with applied 30 % amplitude of ultrasonic mixing of electrolyte II. Red points are composite hardness values and green points are values for hardness of the coating calculated according Chicot-Lesage model. The current density and deposition time were: 50 mA·cm^{-2} and 15 min.

The composite hardness response has a growing tendency with increasing applied indentation load or relative indentation depth (see Fig. 6). The hardness of the coating is lower than the composite hardness in the composite region so it is confirmed that the system belongs „soft film-hard substrate“ composite system type.

Based on the results from: Fig. 4d, Table III (sample 3') and Fig. 6 conclude that a 30 % ultrasound amplitude (3.77 W/cm^2) is an optimal condition for copper ultrasonic deposition from electrolyte II.

D. Determination the copper coatings hardness and adhesion

Absolute hardness of the brass substrate, H_s, necessary to calculate the absolute hardness of the coating, is 1.41 GPa, according to our previous measurements [25].

The results of calculated film hardness according to the Chen–Gao model for the system ED Cu film on brass as the substrate were given in Table IV. Fitting of experimental datas (Fig. 7) were done in Matlab using the *cftool* command.

Films obtained with optimal condition of ultrasonic mixing appear harder than others deposited (sample No. 5). Copper coatings deposited from electrolyte with additives show lower hardness value then same coatings from electrolyte I.

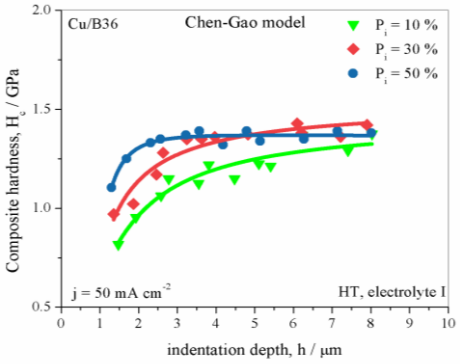

Fig. 7. The dependencies of the composite hardness of the Cu coatings, H_c on indentation depth, h calculated by Eq. (7) for various ultrasound mixing amplitude of electrolyte I.

TABLE IV
THE RESULTS OF CALCULATED FILM HARDNESS ACCORDING CHEN–GAO MODEL AND FITTING PARAMETERS (A, B, C) WITH ROOT MEAN SQUARE ERROR (*RMSE*)

No.	H_{coat}	A	B	C	*RMSE*
1	1.381	1.446	-7.20	-55.2	0.005
3	1.399	1.527	-5.46	-12.3	0.050
5	1.466	1.494	-1.52	-54.1	0.021
3'	1.357	1.412	-4.13	-43.0	0.038

The increase in hardness of electrodeposits obtained with ultrasonic agitation has been associated with the production of deposits with a fine grain size and higher grain-packing density [24]. Equation (9) was used to calculate the critical reduced depth b for the system of thin ED Cu films on the brass as the substrate. The value of the parameter n in the CG model can be 1.2 or 1.8, for soft films 1.8 is taken [12, 17-19].

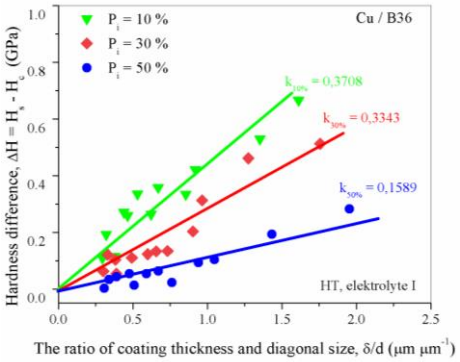

Fig. 8. Hardness difference vs. ratio between the film thickness and the indentation diagonal for copper films on the brass as a substrate. The slope value, k, ED Cu films (electrolyte I) for different ultrasonic mixing amplitude % is shown.

According to the model Chen–Gao (C–G) in Fig. 7 and Fig. 8 the values of slope, k (its value is used to calculate the critical reduction depth, b) for ED Cu films on brass deposited with different ultrasonic amplitude (10, 30 and 50 %) were shown. It was noted higher value of the slope, k, for the sample deposited at lower ultrasound intensity values.

The slopes values, k, (from Fig.7) and the absolute hardness values of the film (from Table IV) were used for the

calculation the critical reduction depth, *b*, the calculated values are shown in the Table V.

TABLE V
THE RESULTS OF CALCULATED CRITICAL REDUCTION DEPTH, ACCORDING TO CHEN–GAO MODEL

No.	electrolyte	*k*	*b*
1	I	0.3708	2.995
3	I	0.3343	2.736
5	I	0.1589	1.165
3’	II	0.2872	4.777

Comparison of the adhesive strength by the adhesion parameter, *b*, can be noticed that higher value corresponds to the ED Cu films from electrolyte II than ED Cu films from electrolyte I. That means that better adhesion properties have ED Cu film with additives then ED Cu films without additives. When additives are added, more intense ultrasonic mixing power contributes to an increase in the adhesive strength of the substrate film and a better dissolution of the additives in the basic electrolyte. In the case of no additives, the adhesion value is almost unchanged with the variation of the mixing power.

V. CONCLUSION

Based on the microhardness measurements, it was shown that the same film with different structural properties giving different mechanical response depending on the electrochemical parameters during synthesis. The copper films deposited on brass from basic electrolyte have higher composite and film hardness values then sonoelectrodeposited copper films from electrolyte with additives for same deposition parameters and projected thickness.With increasing value of applied amplitude ultrasound mixing of electrolyte I, composite hardness value increasing, too. Adhesion properties is better for copper films from electrolyte II on brass then copper films from electrolyte I, because the values of *b* are larger for system ED Cu (electrolyte II)-brass then ED Cu (electrolyte I-brass). Better adhesion properties shown copper film deposited with a higher mixing condition.

ACKNOWLEDGMENT

This work was funded by Ministry of Education, Science and Technological Development of Republic of Serbia, Grant No.451-03-9/2021-14/200026.

REFERENCES

[1] L. C. Hagenson, L. K. Doraiswamy, “Comparison of the effects of ultrasound and mechanical agitation on a reacting solid-liquid system,” *Chem. Eng. Sci.*, vol. *53*, no. *1*, pp. *131–148*, Apr., 1998.

[2] L. Fathyunes, J. Khalil-Allafi, “Effect of employing ultrasonic waves during pulse electrochemical deposition on the characteristics and biocompatibility of calcium phosphate coatings,” *Ultrason. Sonochem.*, vol. *42*, pp. *293–302*, Apr., 2018.

[3] J. M. Costa, A. F. A. Neto, “Ultrasound-assisted electrodeposition and synthesis of alloys and composite materials: A review,” *Ultrason. Sonochem.*, vol. *68*, pp. *105193*, Nov., 2020.

[4] C. T. Walker, R. Walker, “Effect of ultrasonic agitation on some properties of electrodeposits,” *Electrodeposition Surf. Treat.*, vol. *1*, no. *6*, pp. *457–469*, Jul., 1973.

[5] A. K. Behera, A. Mallik, “Ultrasound assisted electroplating of nano-composite thin film of Cu matrix with electrochemically in-house synthesized few layer graphene nano-sheets as reinforcement,” *J. Alloys Compd.*, vol. *750*,, pp. *587–98*, Mar., 2018.

[6] Y. Niu, J. Wei, Y. Yang, J. Hu, Z. Yu, “Influence of microstructure on the wear mechanism of multilayered Ni coating deposited by ultrasound-assisted electrodeposition,” *Surf. Coat. Technol.*, vol. *210*, pp. *21–27*, Oct., 2012.

[7] A. Mallik, B. C. Ray, “Residual stress and nanomechanical properties of sonoelectrodeposited Cu films,” *Surf. Eng.*, vol. *27*, no. *7*, pp. *551–556*, Aug., 2011.

[8] I. Tudela, Y. Zhang, M. Pal, I. Kerr, A. J. Cobley, “Ultrasound-assisted electrodeposition of composite coatings with particles,” *Surf. Coat. Technol.*, vol. *259*, no. *C*, pp. *363–373*, Nov., 2014.

[9] K. Hedayati, G. Nabiyouni, “Surface roughness analysis and magnetic property studies of nickel thin films electrodeposited onto rotating disc electrodes,” *Appl. Phys. A*, vol. *116*, pp. *1605–1612*, Feb., 2014.

[10] I. O. Mladenović, J. S. Lamovec, V. B. Jović, M. M. Obradov, D. G. Vasiljević-Radović, N. D. Nikolić, V. J. Radojević, “Mechanical characterization of copper coatings electrodeposited onto different substrates with and without ultrasound assistance,” *J. Serb. Chem. Soc.*, vol. *84*, no. *7*, pp. *729–741*, Mar., 2019.

[11] L. Bonou, M. Eyraud, R. Denoyel, Y. Massiani, “Influence of additives on Cu electrodeposition mechanisms in acid solution: direct current study supported by non-electrochemical measurements”, *Electrochim. Acta*, vol. *47*, no. *26*, pp. *4139–4148*, Oct., 2002.

[12] L. Magagnin, R. Maboudian, C. Carraro, “Adhesion evaluation of immersion plating copper films on silicon by microindentation measurements,” *Thin Solid Films*, vol. *434*, no. *1*, pp. *100–105*, Jun., 2003.

[13] J. Lamovec, V. Jović, D. Ranđelović, R. Aleksić, V. Radojević, “Analysis of the composite and film hardness of electrodeposited nickel coatings on different substrates,” *Thin Solid Films*, vol. *516*, no. *23*, pp. *8646–8654*, Oct., 2008.

[14] J. Lesage, D. Chicot, A. Pertuz, P. -Y. Jouan, N. Horny, A. Soom, “A model for hardness determination of thin coatings from standard micro-indentation tests,”, *Surf. Coat. Technol.*, vol. *200*, no.*1–4* , pp. *886–889*, Oct., 2005.

[15] D. Chicot, J. Lesage, “Absolute hardness of films and coatings”, *Thin Solid Films*, vol. *254*, no. *1–2*, pp. *123-130*, Jan., 1995.

[16] J. Lesage, A. Pertuz, D. Chicot, “A New Method to Determine the Hardness of Thin Films,” *Revista Matéria*, vol. *9*, no. *1*, pp. *12–19*, Jan. 2004.

[17] M. Chen, J. Gao, “The adhesion of copper films coated on silicon and glass substrates,” *Mod. Phys. Lett. B*, vol. *14*, no. *3*, pp. *103–108*, Mar., 2000.

[18] J. L. He, W. Z. Li, H. D. Li, “Hardness measurement of thin films: Separation from composite hardness,” *Appl. Phys. Lett.* vol. *69*, no. *10*, pp. *1402–1404*, Jun., 1996.

[19] Q. Hou, J. Gao, S. Li, “Adhesion and its influence on micro-hardness of DLC and SiC films,” *Eur. Phys. J. B*, vol. *8*, pp. *493–496*, Apr., 1999.

[20] N. D. Nikolić, Z. Rakočević, K. I. Popov, “Reflection and structural analyses of mirror-bright metal coatings,” *J Solid State Electrochem.*, vol. *8*, pp. *526–531*, Dec., 2004.

[21] http://gwyddion.net/

[22] Y. Li, J. Yang, Z. Pan, W. Tong, “Nanoscale pore structure and mechanical property analysis of coal: An insight combining AFM and SEM images,“ *Fuel*, vol. *260*, pp. *116352*, Jan., 2020.

[23] *Metallic Materials—Vickers Hardness Test—Part 1: Test Method*, ISO 6507-1-2005, International Organization for Standardization: Geneva, Swizterland, 2005.

[24] P. M. Ashokkumar, “*Theoretical and Experimental Sonochemistry Involving Inorganic Systems*”, *2011*th ed. New York, US: Springer, 2014.

[25] I. O. Mladenović, N. D. Nikolić, J. S. Lamovec, D. G. Vasiljević-Radović, V. J. Radojević, “Application of the Composite Hardness Models in the Analysis of Mechanical Characteristics of Electrolytically Deposited Copper Coatings: The Effect of the Type of Substrate,” *Metals*, vol. *11*, no. *1*, pp. *111*, Jan., 2021.

Magnetic Field Generator For Simulation of a Vehicle Movement For a Wide Range of Velocities

Milan Stojanović, *Student Member, IEEE,* Jana Vračar, *Student Member, IEEE,* Ilija Neden Dimitriu, Ljubomir Vračar

***Abstract* — This paper describes the LTSpice model of a magnetic field generator needed for testing a vehicle detector. This simulator reproduces magnetic field distortion equal to a vehicle when passing over the detector located in the road in real conditions. The electric circuit of the simulator described in this paper is a solenoid, PWM generator, and filter capacitors. The different values of capacitors are given for different vehicle velocities. The switching matrix is used for selecting the appropriate capacitor values to achieve simulation of different vehicle velocities.**

***Index Terms* — Magnetic field generator, magnetic field distortion, LTSpice model, vehicle detection.**

I. Introduction

Vehicle detection is an essential part of traffic systems, especially in places of high population density. This system is used to get data about available parking spots and analyze traffic flow [1, 2]. Vehicle detection can be done by analyzing the magnetic field changes, which occur due to the vehicle presence [3]. Fig. 1 shows the placement of the magnetic field sensor on the road, and the changes of the magnetic field due to the passing vehicle over the sensor.

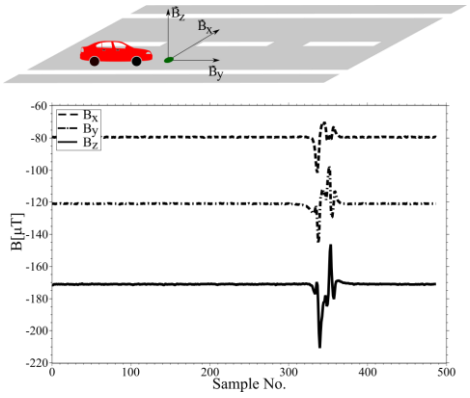

Fig. 1. The placement of the magnetic field sensor on the road, and changes of the magnetic field induced by the vehicle.

Milan Stojanović is with the Department of Microelectronics, Faculty of Electronic Engineering, University of Niš, Aleksandra Medvedeva 14, 18000 Niš, Serbia (e-mail: milan.stojanovic@elfak.ni.ac.rs).

Jana Vračar is with the Department of Microelectronics, Faculty of Electronic Engineering, University of Niš, Aleksandra Medvedeva 14, 18000 Niš, Serbia (e-mail: jana.vracar@elfak.ni.ac.rs).

Ljubomir Vračar is with the Department of Microelectronics, Faculty of Electronic Engineering, University of Niš, Aleksandra Medvedeva 14, 18000 Niš, Serbia (e-mail: ljubomir.vracar@elfak.ni.ac.rs).

Ilija Neden Dimitriu is with the Public Enterprise "Roads of Serbia", 11000 Belgrade, Serbia (e-mail: ilija.nedendimitriu@putevi-srbije.rs).

As shown, the vehicle induces magnetic field distortion along all axes (*x*, *y*, *z*). Determining the vehicle presence can be done by analyzing the measured values from one [4] or several axes [5]. The measured results show that when the vehicle passes over the sensor, it creates bigger changes in the magnetic field along the *z*-axis. Therefore, the values measured along this axis are taken within the analysis usually.

The reliability of the detector needs to be tested before installing it on the road. That includes testing the success of the detection of different types of vehicles moving at different velocities. A simulator capable of reproducing a magnetic change identical to vehicle-induced is useful to increase the efficiency of the testing process. The solenoid is the part of the simulator that generates the magnetic field, and this field depends on the waveform of the current flow through the solenoid, and it is directly proportional to it. The current of an arbitrary waveform can be obtained using the PWM generator of the variable duty cycle (DTC) [6, 7]. If that generator drives the solenoid, the magnetic field of arbitrary shape is created. The rest of the paper shows the magnetic field simulator, described by electrical circuits in the software tool LTSpice. The current flow through the solenoid changes as the magnetic field due to the passing of the vehicle.

II. The Theoretical Principle of Simulator Operation

Fig. 2 shows a relation between the current changes through the solenoid ΔI, and the DTC of PWM voltage, at the end of the pulse. As can be seen, the increase of DTC contributes to an increased value of ΔI. The showed values of ΔI are absolute, so the value of the current flow is equal to zero before a pulse arrival.

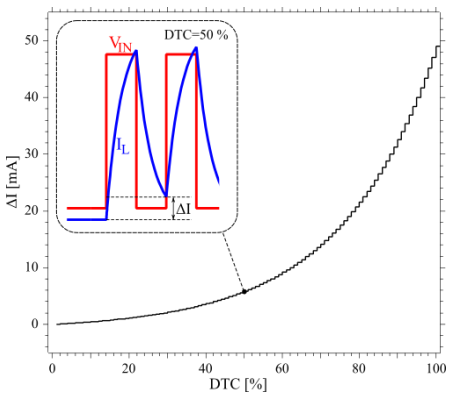

Fig. 2. Influence of duty cycle of PWM voltage to the intensity of the current through the solenoid.

The current flow through the solenoid is changed, by changing the duty cycle of PWM voltage. The current intensity can be controlled in this way, but the current always flows in the same direction. The coil should be connected to the two PWM generators to allow the change in the direction of the current flow and thus generate changes in the magnetic field as the vehicle does. Fig. 3 shows a simplified schematic of the simulator.

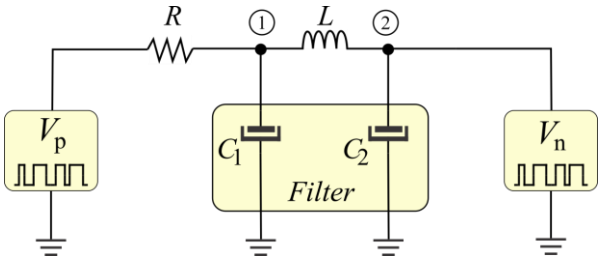

Fig. 3. Simplified schematic of the magnetic field simulator.

The simulations of current flow were done using LTSpice software. The ideal solenoid inductivity is 100 mH, and that value is used in the software. The resistor R limits the current intensity (magnetic field), and the value is 100 Ω. The capacitors C_1 and C_2 form a filter that suppresses sudden changes in a current flow when voltage level changes of both generators.

PWM generators are realized as PWL (Piecewise Linear) generators in LTSpice. The parameters of PWL generators were generated inside textual files. The textual file of every PWL generator contains couples of points (x, y), where x represents the time, and y represents voltage values. The generator makes pulses by reading values from the file.

A. PWM generators

The magnetic field that presents the passing of one vehicle is created by driving the solenoid by 100 pulses from the generators. The V_p makes positive, and V_n negative changes to the magnetic field.

The duty cycle of the PWM voltage of both generators is proportional to the changes in the magnetic field. The frequency of PWM voltage depends on the duration of the magnetic field distortion.

The duration of one pulse is calculated as

$$t_{pulse} = \frac{t}{100},$$

where t represents the time of magnetic field distortion. In this case, the distortion is induced by a vehicle, so t can be replaced by $t_{vehicle}$ and this value depends on the length ($l_{vehicle}$) of the vehicle and its velocity ($v_{vehicle}$)

$$t = t_{vehicle} = \frac{l_{vehicle}}{v_{vehicle}}.$$

So the duration of one pulse is

$$t_{pulse} = \frac{d_{vehicle}}{100 \cdot v_{vehicle}},$$

and the frequency of the pulse signal is equal to

$$f_{pulse} = \frac{1}{t_{pulse}} = 100 \cdot \frac{v_{vehicle}}{d_{vehicle}}.$$

The length of the vehicle is considered to be 4 m. The textual files of both PWL generator V_p and V_n are created based on the value of t_{pulse}. One pulse is defined by four points (x, y), as shown in Fig. 4.

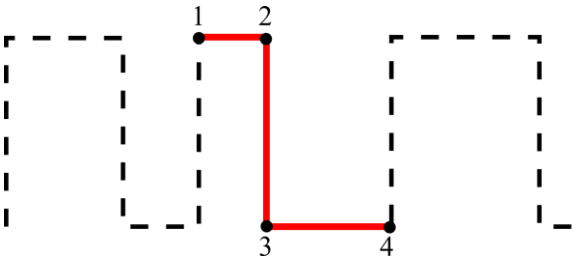

Fig. 4. Points that determine the frequency and duty cycle of one pulse of PWM voltage.

The x_1, y_1 are coordinates of the first point, x_2, y_2 the second, et cetera. The values of coordinates of all four points are calculated:

$$(x_1, y_1) = \left((i-1)\cdot t_{pulse} + \Delta t, V_{ON}\right)$$

$$(x_2, y_2) = \left((i-1)\cdot t_{pulse} + DTC_j[i]\cdot \frac{t_{pulse}}{100} + \Delta t, V_{ON}\right)$$

$$(x_3, y_3) = \left((i-1)\cdot t_{pulse} + DTC_j[i]\cdot \frac{t_{pulse}}{100} + 2\Delta t, 0\right)$$

$$(x_4, y_4) = \left(i \cdot t_{pulse}, 0\right)$$

$$j \in \{p, n\}, i \in \{1, N\},$$

where N represents the number of pulses. Δt is the time interval needed to change the value of the generator voltage from 0 to V_{ON} and vice versa. This interval value is much smaller than the value of the t_{pulse}, so it does not affect the accuracy of the frequency of the generated voltage. The noted equations apply if the condition is met

$$DTC_j[i] \neq 0.$$

Otherwise, the voltage value at points 1 and 2 is equal to zero, and only point 4 within the current pulse is generated.

B. Filter capacitors

The capacitance values of C_1 and C_2 are equal, because the frequency of both generators is equal, and they are determined experimentally. Fig. 5 shows the current waveform through the solenoid for vehicle density of $1\frac{m}{s}$ and three different values of capacitors C_1 and C_2.

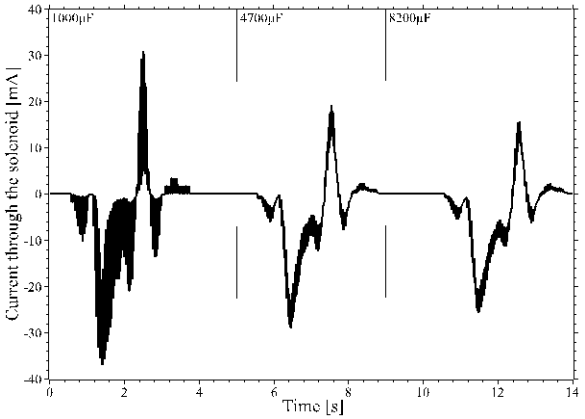

Fig 5. The waveforms of the current through the solenoid for vehicle velocity of $1\frac{m}{s}$ and three different values of C_1 and C_2.

If the capacitors C_1 and C_2 have a capacitance of 1000 μF there are unwanted high-frequency changes in the waveform of the current through the solenoid. These changes should be "smoothed" to get the required shape of the generated magnetic field.

In the other case, if the capacitors have too large values, such as 8200 μF, the amplitude of the current waveform becomes attenuated. So, the simulation shows that the appropriate values of C_1 and C_2 are 4700 μF for shown vehicle velocity.

In Fig. 6. the current through the solenoid for vehicle velocity from $1\frac{m}{s}$ to $5\frac{m}{s}$ is shown.

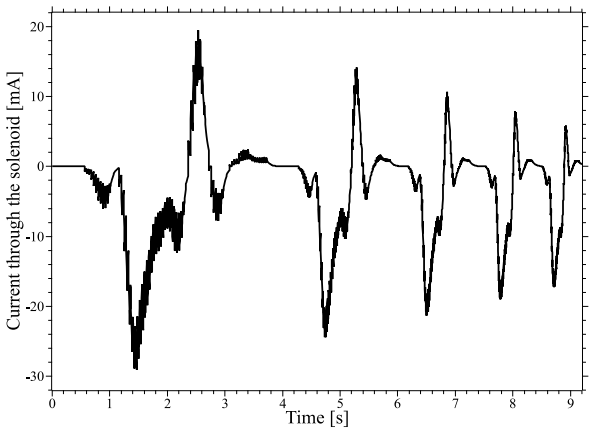

Fig. 6. The waveforms of the current through the solenoid for vehicle velocity from $1\frac{m}{s}$ to $5\frac{m}{s}$. The value of vehicle velocity increases from the left to the right side.

There are two problems when a vehicle's velocity rises. The amplitude of the current waveform decreases, but the waveform shape is degraded also. That happens because the capacitance values of C_1 and C_2 are too large. It is required to determine appropriate values of capacitors for all vehicle velocities, or for ranges of the velocity that is supposed to be simulated.

That is done experimentally, by creating the PWM generators of various frequencies. Table I shows the values of capacitors C_1 and C_2 which are depending on the vehicle velocity, whose movement is simulated.

TABLE I
VALUE OF FILTER'S CAPACITORS FOR DIFFERENT VEHICLE VELOCITY

Vehicle velocity [m/s]	Capacitance C_1 and C_2 [uF]
1	4700
2	1800
3	820
4 - 5	470
6 - 7	220
8 - 10	150
11 - 15	120
16 - 20	68
20 - 30	47
30 - 50	22

Capacitor values should be selected before starting the simulation.

III. SWITCHING MATRIX AND RESULTS

Changing capacitor values without interrupting the simulation and manual reconnection of new components can be made using the switching matrices, shown in Fig. 7. In this way, the capacitor value can be selected depending on the frequency of the PWM signal. It provides the ability to simulate an unlimited number of vehicles of different lengths and velocities.

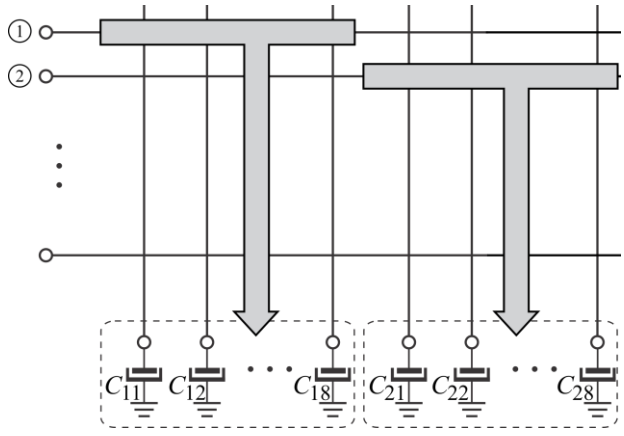

Fig. 7. The simplified block schematic of the switching matrix. The first and the second index of capacitors denotes the row and column of the switching element, respectively.

The complete switching matrix contains eight rows and 16 columns. In this case, two rows and the 8 columns of every row are used.

The necessary row number of the matrix determines the number of different capacitances connected simultaneously. Table I shows that the number of different values of capacitor capacitance is ten. The matrix contains eight columns, allowing the connection of up to eight various capacitors. The first row of the matrix is used instead of the capacitor C_1, and the second matrix instead of C_2. The capacitor values from C_{11} to C_{18} are shown in Table I, there the C_{11} is the biggest value. The capacitors connected in both rows are equal. The capacitance of C_{11} is equal to C_{21}, the C_{12} is equal to C_{22}, and so on. Because there are eight different capacitors in the circuit, and there are ten values that are needed for shown velocity range, two capacitances are missing. In this case, the capacitors of 68 µF and 220 µF are not connected because these values can be obtained as a combination of others. Two remaining capacitances are obtained by a parallel connection of connected capacitors, 68 µF as the sum of 47 µF and 22 µF, and 220 µF as the sum of 150 µF, 47 µF, and 22 µF.

The selection of the capacitors that need to be connected to the output is done by the components inside the matrix. In Fig. 8 is shown the simplified schematic of one row of the switching matrix. The microcontroller controls all rows and is positioned left out of the schematic for better visibility.

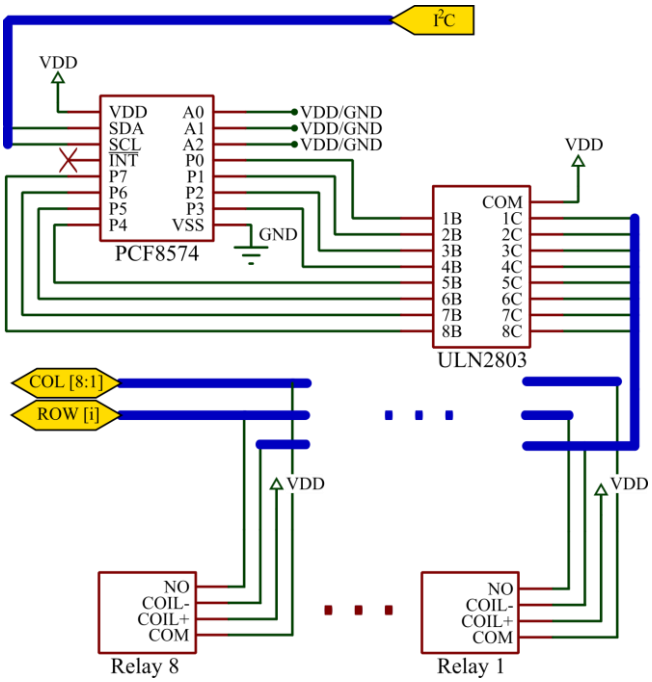

Fig. 8. The simplified schematic of one row of the switching matrix.

The input stage of a row is the I/O expander [8] that receives data from the microcontroller via I^2C communication. The received one byte of data determines which switching elements will be activated. This information is forwarded to the driver [9], which activates one or more appropriate switching elements (relays) [10]. The capacitors are connected to the output of the matrix, after the activation of relays. The PWM generators, after the selection of the capacitors, are activated. If the next simulated vehicle has velocity from another range, the appropriate capacitance is set again, and the simulation is repeated.

The current waveform through the solenoid is shown in Fig. 9, wherein the corresponding capacitor is used for each simulated vehicle velocity.

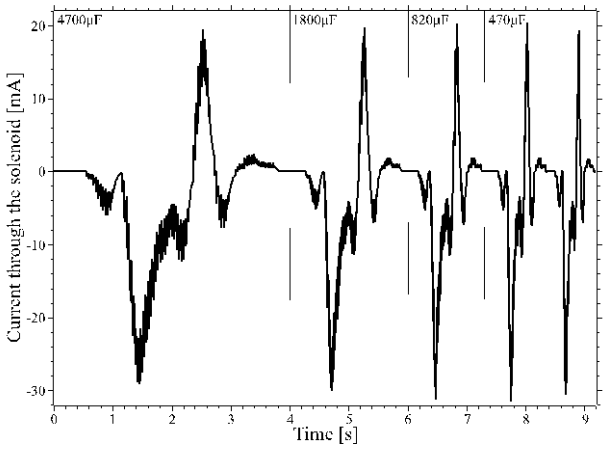

Fig. 9. The current through the solenoid for vehicle velocity from 1 m/s to 5 m/s, with a corresponding capacitor used for each simulated vehicle velocity.

Comparing Fig. 9 and Fig. 6 can be seen that using of switching matrix contributes to getting the current waveforms without degradations. The current through the solenoid has the same waveform for all simulated vehicle velocities. The current amplitude is also unchanged and does not depend on a vehicle's velocity.

IV. Conclusion

In this paper simulation for replicating a magnetic change identical to vehicle-induced is described. The simulator is described by the electrical circuit in LTSpice. The part of the simulator is a solenoid that generates the magnetic field. The PWM generators of variable DTC drive the solenoid to generate the current flow of arbitrary shape. That current flows through the solenoid and the magnetic field of the same waveform is generated.

Connecting the solenoid to the two PWM generators results in a change in the direction of the current flow. That change generates changes in the magnetic field equal to vehicle-induced changes in the magnetic field.

Degradation of generated magnetic field for different velocities are regulated by capacitor filter, with various values of capacitors C_1 and C_2. The values for capacitors are determined experimentally, and a part of the switching matrix for selecting the values for capacitors is used. When using the appropriate capacitor value, the amplitude and waveform of the current through the solenoid are unchanged for a wide range of vehicle velocities.

The future research will be based on expanding the scope of

simulations for different types of vehicles. Also, one of the next steps in researching is the practical realization of the described simulator.

ACKNOWLEDGMENT

This paper is supported by the Serbian Ministry of Education, Science and Technological Development No. 451-03-9/2021-14/200102.

The described research is done in cooperation with Public Enterprise "Roads of Serbia", Serbia.

REFERENCES

[1] J. Gu, Z. Zhang, F. Yu and Q. Liu, "Design and implementation of a street parking system using wireless sensor networks," IEEE 10th International Conference on Industrial Informatics (INDIN), Beijing, China, pp. 1212-1217, 25-27 July 2012.

[2] E. Sifuentes, O. Casas, and R. Pallas-Areny, "Wireless Magnetic Sensor Node for Vehicle Detection With Optical Wake-Up", *IEEE SENSORS JOURNAL*, vol. 11, no. 8, pp. 1669-1676, August 2011.

[3] Michael J. Caruso, Lucky S. Withanawasam, "Vehicle Detection and Compass Applications using AMR Magnetic Sensors", Honeywell, SSEC, 12001 State Highway 55, Plymouth, MN USA 55441

[4] S. Y. Cheung, S. Coleri, B. Dundar, S. Ganesh, C-W Tan and P Varaiya, "Traffic Measurement and Vehicle Classification with Single Magnetic Sensor", *Transportation Research Record*, vol. 1917, no. 1, pp.173-181, 2005.

[5] Q. Wang, J. Zheng, H. Xu, B. Xu and R. Chen, "Roadside Magnetic Sensor System for Vehicle Detection in Urban Environments," *IEEE Transactions on Intelligent Transportation Systems*, vol. 19, no. 5, pp. 1365-1374, May 2018.

[6] Q. Zhong, B. Zhang, H-Y Yang, J-E Ma, R-F Fung. "Performance analysis of a high-speed on/off valve based on an intelligent pulse-width modulation control", *Advances in Mechanical Engineering*, vol 9, no. 11, November 2017.

[7] V. Steinsland, "Modeling and Control of Retarder using On/Off Solenoid Valves", Masters' Degree Project, Stockholm, Sweden April 2008.

[8] PCF8574 Remote 8-Bit I/O Expander for I^2C Bus, Datasheet, https://www.ti.com/lit/ds/symlink/pcf8574.pdf?ts=1621942328093&ref_url=https%253A%252F%252Fwww.google.com%252F

[9] ULN2803A Darlington Transistor Arrays, Datasheet, https://www.ti.com/lit/ds/symlink/uln2803a.pdf?ts=1621921786139&ref_url=https%253A%252F%252Fwww.startpage.com%252F

[10] HE3600 Miniature Single In-line Reed Relay, Datasheet https://eu.mouser.com/datasheet/2/240/Littelfuse_Reed_Relays_HE3600_Datasheet_pdf-876890.pdf

Active Matrix Liquid Crystal Display – AMLCD Switching Time Measurements

Branko Livada, *Member SPIE*

***Abstract*—Liquid crystal displays (LCD) are currently dominant in visual content presentation applications. In the case of video content presentation LCD switching time determines image appearance and perception. The photometric and temporal properties of LCDs are unfamiliar to many practitioners, especially switching time temperature dependence. In specific applications as ruggedized military displays temperature dependence is critical parameter for operation on low temperatures. Current liquid display technology does not provide proper operation at low temperatures so additional heater should be incorporated into display design. The temperature dependence of switching time provides initial data determining heater design parameters. The short review of the LCD switching time theory is presented. The AMLCD switching time over temperature, method is described. The selected measurement results are presented and discussed.**

***Index Terms*—liquid crystal display; active matrix liquid crystal display; switching time; rise time; fall time; measurement method; temperature dependence.**

I. Introduction

Twenty first century is century of liquid crystal (LC) displays (LCDs) that have been widely applied from small-size mobile devices to large-size televisions. Various methods have been developed for higher and advanced performance of active-matrix LCDs (AMLCDs) to provide superior application results [1]-[7]. Some of the most important achievements are: fast response LC providing high frame rate driving, backlight dimming technology for low consumption and high contrast ratio, wide viewing angle LC modes, high temperature range of operation etc. The majority of advancements have been achieved through advancements in LC science and technology [8]-[10].

The deep knowledge about LC [11]-[13] physical, optical and electro-optical properties is extensively used in design and operation of LCD pixel. One of the critical parameters is LCD pixel switching performances influencing proper video content reproduction, from the well–known issue of motion blur, to photometric settings and calibrations. Displays with faster transitions (switching) between different luminance levels are considered as supperior in the case of video content presentation. Because of that LC optical switching performances are studied theoretically and related measurement techniques have been developed. The basic data about LCD switching time is summarized in separate chapter.

Branko Livada is with the Vlatacom Institute of High Technologies, 5 Bulevar Militina Milankovića, 11070 Belgrade, Serbia (e-mail: branko.livada@ vlatacom.com).

In the specific application as ruggedized military displays [14]-[18] some of performances are critically important for application. Among the other parameters switching time is slightly more important, because it has influence on display design in addition to operation parameters. Current LC technology do not provide proper LCD operation at low temperatures as required in military applications, so additional heater should be built in display to provide proper display operation at low temperatures. The temperature dependence of the switching time determines the heater design and consumption sufficient to provide display proper operation at low temperatures.

In this paper measurement method applicable for display switching time measurements over display operation temperature range is described. The selected measurement results illustrating the switching time temperature dependence for several AMLCD panels are presented. Also, these results provide initial data for LCD heater design.

II. AMLCD Switching time

Liquid crystal occupies a small portion in an LC device, but plays a key role in determining the device performances. The LC material and molecular alignment jointly determine the device contrast ratio, operation voltage, response time, viewing angle, and operating temperature.

The LCD response time consideration has two key aspects:

(a) How to design liquid crystal composition to have desired response – switching time values? This is not topic of this article, but some aspects will be mentioned just for better understanding. More details could be find in references [19]-[29] dealing with theoretical studies and modeling of the switching time behavior in different LC materials and LCD architectures.

(b) What is the influence of the switching time on presented video content appearance and perception? This is important to define limiting values depending on application [30], [31].

The LCD response time depends on different factors as illustrated in TABLE I. All off listed parameters depends on temperature, so LC scientists have a hard task to design LC composition having desirable temperature dependence on temperature.

The temperature dependence of dielectric anisotropy - $\Delta\varepsilon$ is limiting factor at high temperatures. Usually as temperature increases, $\varepsilon//$ decreases while $\varepsilon\perp$ increases gradually, resulting in a decreased $\Delta\varepsilon$. As $T > T_c$, the isotropic state is reached and the dielectric anisotropy is vanished, with no birefringence. Critical temperature T_c is high temperature at

which LC lost its birefringence properties and LCD stop to work. Typical values for T_c are in the range 70°C up to 100°C.

TABLE I
THE EFFECTS OF DIFFERENT FACTORS ON RESPONSE TIME

Factors	T_{on}	T_{off}
Viscosity (γ1) ↓	↓	↓
Elastic constants (Kii) ↑	↑	↓
Dielectric anisotropy (Δε)↑	↓	↓
Thickness (d) ↓	↓	↓
Pretilt angle (θ0) ↓	↑	↓
Anchoring energy (W) ↑	↑	↓
Temperature (T) ↑	↓	↓
Voltage (V) ↑	↓	↓

The viscosity and elastic constants are limiting factors at low temperatures causing slower motion of LC molecules when electrical field is applied to change the order of LC in device.

The LC electro optical properties (time and temperature dependence) influence the display pixel response characteristics defining display video content appearance. One of the most important effects is motion blur appearance.

The motion-induced distortion [32], [33] of a visual target moving across an electronic display screen perceived as blurring of initially sharp edges by a human observer (motion blur) is caused by two effects:

- characteristics of the electro-optical response of the display to changes in video signal
- integration properties of the of the human visual system while

The increased response times of LCD pixel corrupt the visual quality of moving objects and thus contribute to motion blur.

III. AMLCD SWITCHING TIME MEASUREMENT METHOD

Motion blur influences display applicability on the different way depending on presented video content properties. Because of that motion blur measurement methods [34], [35] should be designed on different ways as illustrated in Fig.1.

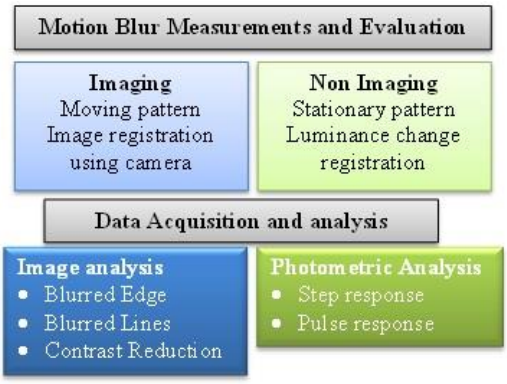

Fig. 1. Motion blur measurement and evaluation methods

Imaging methods are using selected moving patterns (blocks, lines, grille, grating etc.) presented on display and related image is recorded with tracking or stationary electronic cameras, and after that analyzed to quantify motion blur effects.

Non-imaging methods use stationary patterns on display surface but having temporary defined intensity change (pulse, step, periodic etc.) and pattern luminance level is measured using photometer [36].

In the case of ruggedized display presenting virtual instrument scale having moving bar edge proportional to the related quantity value it is important to have un-blurred moving edge to provide proper instrument reading. The LCD switching time value could be limitation factor. That type of display should be used reliably over all operation temperatures. As LC has known limitation for operation on low temperatures so LCD switching time temperature dependence should be known. This type of data is not presented in display data sheet so it is necessary that display designer provide that data.

Ideally, the measurement system should provide data about display panel brightness change versus temperature. To provide this it is necessary to avoid influence of the temperature to light sensor subsystem. For switching speed measurements, brightness change over time at set temperature should be recorded.

AMLCD Response Time is usually defined as sum of rise time (T_{on}) and fall time (T_{off}). T_{on} is defined as time necessary to change light signal from 10% value to 90% value when display pattern is changing from black to white. T_{off} is defined as time necessary to change light signal from 90% value to 10% value when display pattern is changing from white to black (See Fig.2).

We could only to compare response time (T_{on} & T_{off}) as defined previously. Also gray-to-gray level response time matters for video content presentation. In our case we are presenting moving bar instrument scale so it is good enough to measure only black to white level change.

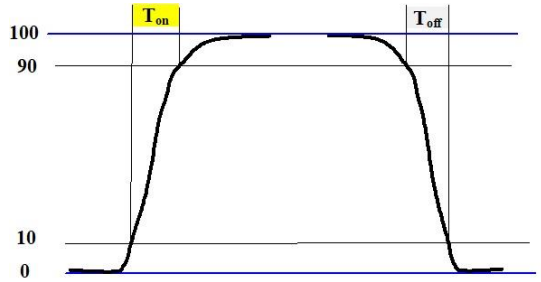

Fig. 2. T_{on} and T_{off} definition

Response Time is important parameter we need to know, to specify, at first place, heater requirements. Also, it is important parameter defining speed of response in the case of high frame rate imaging and fast motion artifacts in image. The way how it is defined does not allow us to have full sense what influence it has to image quality. Pixel response delay due to driving electronics is missing parameter.

Display temporal response was measured using a photodiode-based circuit and an oscilloscope. The photodiode

was directed at switchable (black and white) square generated by our test program. A memory scope was used to record the photodiode response. Controlled temperature chamber is used to stabilize AMLCD panel temperature. Originally proposed measurement set-up is presented in Fig.3. It is proposed as best solution to use collection lens coupled with fiber-optical cable to provide that temperature have influence only on AMLCD panel while other parts of measurement chain are on room temperature. Following the facts that Si photodiode do not suffer of the response temperature dependence and that T_{on} , T_{off} data are extracted from relative photo signal values (see Fig.2) we selected simplified solution presented in Fig.4 and using collection lens and Si photodiode placed in temperature chamber and connected to photo current measurement circuit via coaxial cable.

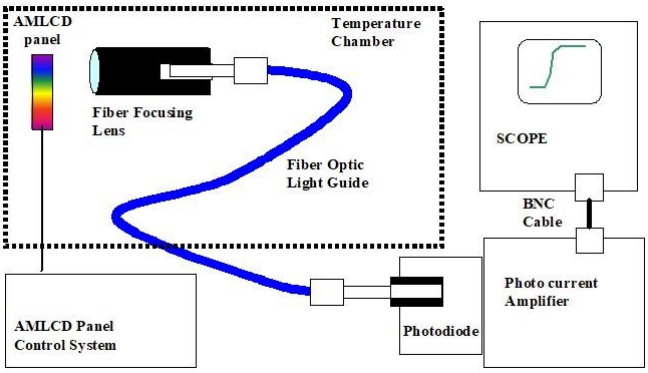

Fig. 3. Switching time measurement set-up

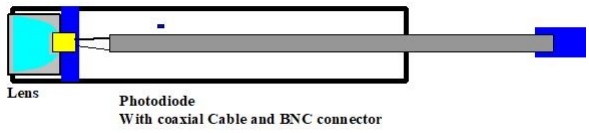

Fig. 4. Photodiode with collection lens

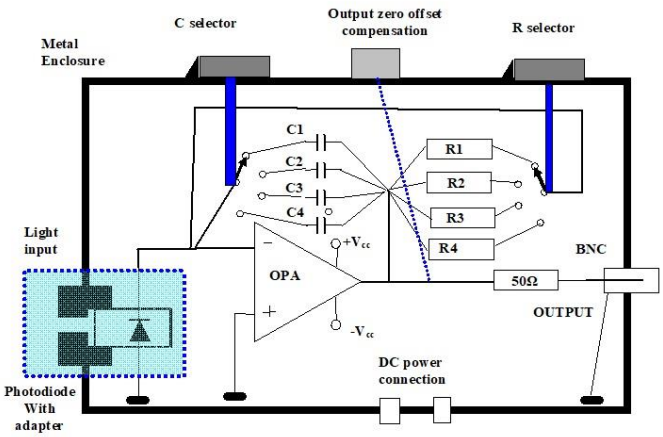

Fig. 5. Photocurrent to voltage electronic block schematic

Generated photocurrent is measured using photo current to voltage converter (trans-impedance operational amplifier) presented in Fig.4.

The light generated signal is generally noisy or involving high frequency components due to LCD backlight switching. It is good to filter the signal before recording to have more smooth line and easier determination of required 10% and 90% values. Because of that we use additional capacitance over load resistor for filtering, but RC constant should be at least ten times less than expected rise or fall time values.

The described photometric device and climatic chamber offers, flexible and easy evaluation of displays switching time in specific temperature environment between -40°C to +85°C.

Sensor and amplifier were tested and calibrated using 586 fL uniform halogen lamp in integration sphere white source (color coordinates x=0,386, y=0,401). Calibration results are summarized and presented in TABLE II.

TABLE II
CALIBRATION RESULTS

	R [K]	Voltage Sensitivity [mV/fL]	Photo -Current Sensitivity [nA/fL]
R1	100	0.59	5.87
R2	388	2.28	5.88
R3	910	5.37	5.90
R4	3260	19.28	5.91
Average current sensitivity			**5.89**

IV. AMLCD SWITCHING TIME MEASUREMENT RESULTS

In the proposed paper, we present experimental results obtained on several commercial LCDs using a thermal enclosure allowing a required temperature range.

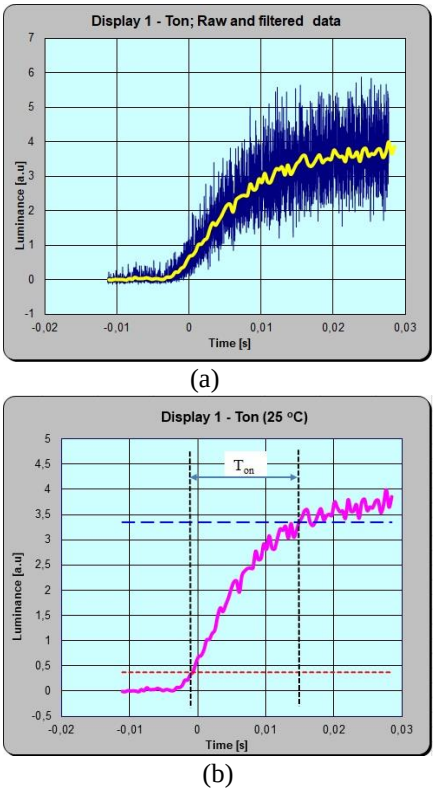

Fig. 6. T_{on} measurement signal (a) raw signal, (b) processed signal

The typical view of the recorded photometric signal during white to black and black to white switching is presented in Fig.6 and Fig.7.

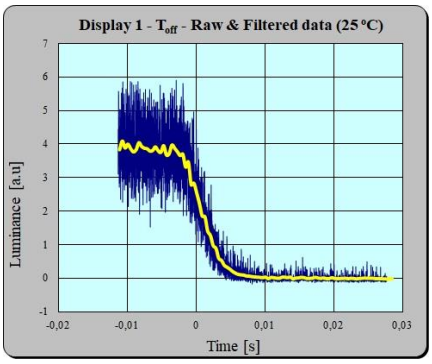

(a)

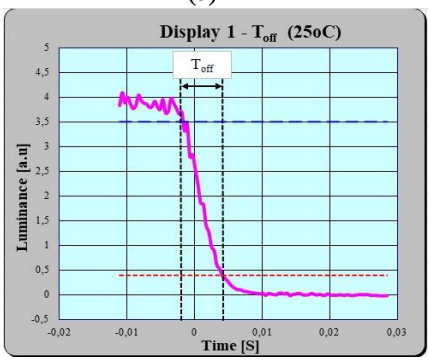

(b)

Fig. 7. T_{off} measurement signal (a) raw signal, (b) processed signal

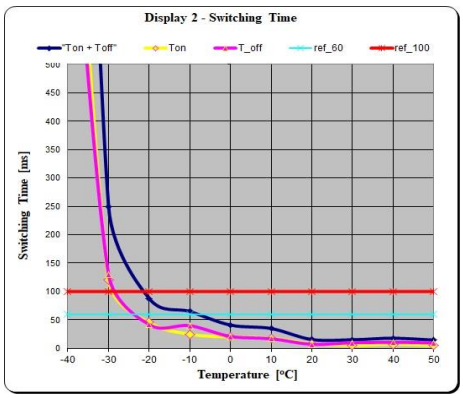

Fig. 8. Switching time vs. temperature measurement results (Display 2)

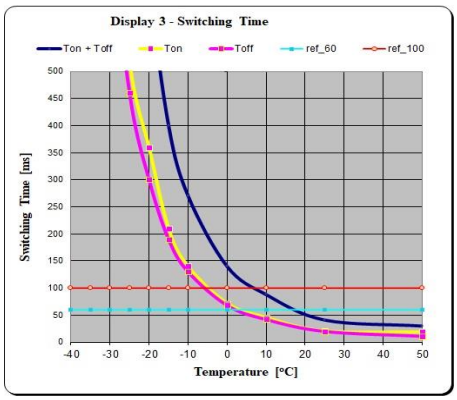

Fig. 9. Switching time vs. temperature measurement results (Display 3)

Measurement signal is exported as ASCI file and transferred to EXCEL spread sheet for further processing. Following recommendations from [37] and [38] moving averaging filter is successfully used for curve smoothing as illustrated in Fig.5 (a) and Fig.6(a).

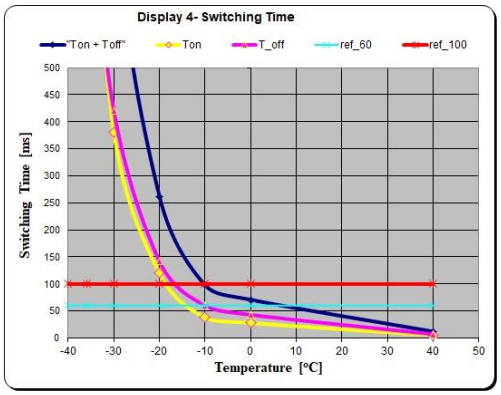

Fig. 10. Switching time vs. temperature measurement results (Display 4)

The summary of the measurement results for several AMLCD panels are presented in Fig.8 to Fig.10 together with two selected switching time critical values (60ms and 100ms). These results could be used to determine the lowest display operation temperature and provide starting data for heater design

V. Conclusion

AMLCD switching time depends on various LC parameters and LCD pixel design and operation. Also, switching time has influence on AMLCD panel operation. One of the most important switching time influences is motion blur appearance.

New light sensor aimed for response time measurements were built and tested and calibrated for photo current response.

Testing and calibration results show that it could be used successfully in all future response time measurements.

Switching time vs. temperature data are presented for several selected AMLCD panels and show that they have different critical temperature values. To use effectively these measurement results for heater design it is necessary to determine switching time (T_{on}, T_{off} or T_{on}+T_{off}) critical values to avoid motion blur influence according to display application.

It is shown that relatively simple and accurate method for switching time measurements could be designed and applied for aimed purpose when display critical switching time is known. The measurement methodology is successfully applied

In the case of display presenting virtual instrument scale having moving bar edge it was possible to determine critical switching time values. Using switching time vs. temperature measurement results heater design requirements could be derived.

REFERENCES

[1] *D.-K.* Yang and S.-T. Wu, *Fundamentals of Liquid Crystal Devices* , John Wiley & Sons, Ltd., New York, USA, 2006

[2] Jiun-Haw Lee, David N. Liu and Shin-TsonWu, *Introduction to Flat Panel Displays*, JohnWiley & Sons Ltd., Chichester, UK, 2008

[3] Robert H. Chen, *Liquid Crystal Displays: Fundamental Physics and Technology*, by John Wiley & Sons, Inc., Hoboken, New Jersey, USA, 2011

[4] Deng-Ke Yang and Shin-Tson Wu, *Fundamentals of Liquid Crystal Devices*, John Wiley & Sons Ltd, The Atrium, Southern Gate, Chichester, England, UK, 2006

[5] Roll R.Hainich, Oliver Bimber, *DISPLAYS: Fundamentals and Applications*, 2nd edition, Taylor & Francis Group, LLC, CRC Press,Boca Raton, USA, 2017

[6] Willem den Boer, Active Matrix Liquid Crystal Displays: Fundamentals and Applications, Elsevier Inc., New York, USA, 2005

[7] Janglin Chen, Wayne Cranton, Mark Fihn (Eds.), *Handbook of Visual Display Technology*, Springer-Verlag, Berlin, Heidelberg, Germany, 2012

[8] Hirohisa Kawamoto, The History of Liquid-Crystal Displays, *Proc. IEEE*, Vol. 90, No. 4, pp.460-500, 2002

[9] Haiwei Chen & Shin-Tson Wu, Advanced liquid crystal displays with supreme image qualities, *Liquid Crystals Today*, 28:1, 4-11, 2019

[10] Askari Mohammad Bagher, Mirzaei Mahmoud Abadi Vahid, Mirhabibi Mohsen, A Review of Challenges in Display Technology, International *Journal of Electrical Components and Energy Conversion*, 3(2): 26-39, 2017

[11] D. Demus, J. Goodby, G.W. Gray, H.-W. Spiess, V Vill, *Physical Properties of Liquid Crystals*, Wiley-VCH, New York, Chichester, Brisbane; Singapore, Toronto, 1999

[12] Khoo, Iam-Choon: *Liquid crystals*, 2nd ed., John Wiley & Sons, Inc., Hoboken, New Jersey, USA, 2006

[13] Sergey V. Pasechnik, Vladimir G. Chigrinov, Dina V. Shmeliova, *Liquid Crystals: Viscous and Elastic Properties*, WILEY-VCH Verlag GmbH & Co. KGaA, Weinheim, Germany, 2009

[14] Keith K. Niall (Editor), *Vision and Displays for Military and Security Applications: The Advanced Deployable Day/Night Simulation Project*, Springer Science+Business Media, LLC, Springer New York Dordrecht Heidelberg London, 2010

[15] Branko Livada, Radomir Jankovic, Nikolic, AFV Vetronics: Displays Design Criteria, *Strojniški vestnik - Journal of Mechanical Engineering (JME)*, vol.**58**, No6, 376-385, 2012

[16] Branko Livada, Ruggedized Avionic Displays Technology: Past, present, and future, *4th International Scientific Conference OTEH 2011*, Belgrade, 06-07, October 2011, 2011

[17] Branko Livada, "Avionic Displays", *Scientific Technical Review*, Vol. **62**, No.3-4,pp.70-79, 2012

[18] Branko Livada, Displays Metrology status and new challenges, *9th International Scientific Conference OTEH 2020*, Belgrade, 08-09, October 2020, 2020

[19] H Wohler, M. E. Becker, Numerical Modeling of LCD Electro-Optical performances, *Opto-Electronics Review*, 10(1), 23-33, 2002

[20] Fenglin Peng, Haiwei Chen, Fangwang Gou, Yun-Han Lee, Michael Wand, Ming-Chun Li, Seok-Lyul Lee, and Shin-Tson Wu, Analytical equation for the motion picture response time of display devices, *J. Appl. Phys*. 121, 023108 ,2017

[21] Lachezar Komitov, Liquid Crystal Polar State and Fast Switching, *IMID/IDMC/ASIA DISPLAY 2010 DIGEST, 18, 2010*

[22] Pierre Adam, Pascal Bertolino, Fritz Lebowsky, Mathematical modeling of the LCD response time, Journal of the Society for Information Display, 15 (8), pp.571-577, 2007

[23] Youngmin Cho, Chansoo Park, Jong-Man Kim, Seung-Hyuck Lee, and Seung-Woo Lee, A Behavioral Circuit Model of Active-Matrix Liquid Crystal Displays for Optical Response Simulation, *IEEE TRANSACTIONS ON ELECTRON DEVICES*, Vol. 59, No. 5, 1430-1438, 2012

[24] Jong-Man Kim, Seung-Hyuck Lee, and Seung-Woo Lee, Behavioral Model of Patterned Vertical Alignment Pixel in Active-Matrix Liquid Crystal Displays, *IEEE TRANSACTIONS ON ELECTRON DEVICES*, VOL. 61, NO. 11, 3783-3790, 2014

[25] S. H. Lee, S. L. Lee, and H. Y. Kim, Electro-optic characteristics and switching principle of a nematic liquid crystal cell controlled by fringe-field switching, *Applied Physics Letters* **73**, 2881-2883, 1998

[26] Pierre BOHER, Thierry LEROUX and Thibault BIGNON, Response Time and Viewing Angle Behavior of Liquid Crystal Displays versus Temperature, *Conference: Vehicle Displays*, Livonia, USA, September 2016

[27] Jong-Man Kim, Dong-Gun Lee, and Seung-Woo Lee, Temperature-Dependent Behavioral Model of Active-Matrix Liquid Crystal Displays for All Types of Liquid Crystals, *Journal of Display Technology*, Vol. 12, Issue 9, pp. 881-887, 2016

[28] Jong-Man Kim and Seung-Woo Lee, Temperature-dependent behavioral model of pixels in active-matrix liquid crystal displays with fringe-field switching mode, *Optical Engineering*, 54(9), 093104, 2015

[29] Jong-Man Kim and Seung-Woo Lee, Temperature-Dependent Behavioral Model of Twisted Nematic Pixel in Active-Matrix Liquid Crystal Displays, *SID 2015 DIGEST*, 1536-1539, 2015

[30] Tobias Elze, Thomas G. Tanner, Temporal Properties of Liquid Crystal Displays: Implications for Vision Science Experiments, *PLOS ONE*,| Volume 7, Issue 9, e44048, September 2012

[31] Jun Someya, Hiroaki Sugiura, Evaluation of liquid-crystal-display motion blur with moving-picture response time and human perception, *Journal of the SID* 15/1, 78-86, 2007

[32] Michael E. Becker, Motion-blur evaluation: A comparison of approaches, *Journal of the SID* 16/10, 989-1000, 2008

[33] Andrew B. Watson, Display motion blur: Comparison of measurement methods, Journal of the SID 18/2, 179-190, 2010

[34] Michael E. Becker, Motion Blur Measurement and Evaluation: From Theory to the Laboratory, SID07 DIGEST, 1122-1226, 2007

[35] Michael E. Becker, LCD Response Time Evaluation in the Presence of Backlight Modulations, *SID 08 DIGEST*, 1, 2008

[36] Michael E. Becker, Temporal characteristics of electronic display screens, DM&S 2013

[37] --, *Information Display Measurement standard*.- IDMS v.1.03, Society of Information Displays, June 01, 2012

[38] José Luis Guiñón, Emma Ortega, José García-Antón, Valentín Pérez-Herranz, Moving Average and Savitzki-Golay Smoothing Filters Using Mathcad, *International Conference on Engineering Education – ICEE 2007*, Coimbra, Portugal September 3 – 7, 2007

Hyper Focal Distance Application for Long Range Surveillance Camera Zoom Lens Focusing Settings

Saša Vujić, Member SPIE, Dragana Perić, *Member, IEEE*, Branko Livada, *Member, SPIE*

***Abstract*—Modern multi sensor surveillance systems integrate several multispectral imaging channels, laser range finder and positioning sensors (digital magnetic compass – north finding sensor and GPS sensor). Imaging channels use motorized zoom lenses providing convenient and fast field of view –FOV change. The fast FOV change to desired value keeping optimal image sharpness is provided through selected FOV pre-set settings using zoom lens position setting to desired values. In addition to FOV settings it is useful to pre-set lens focus motor position. The zoom lens hyper-focal distance determination for selected FOV and lens focusing motor position setting accordingly is used as pre-set lens parameter definition. The short review of the motorized zoom lens design and their basic properties is presented. The lens depth of field and hyper focal distance are discussed and basic formulas are derived. The zoom lens based imaging channel calibration procedures selection depends on application. We presented in detail hyper-focal distance based focusing motor parameter setting as one of the calibration procedures used in our multi sensor imaging systems.**

***Index Terms*—Surveillance systems, imaging system calibration, motorized zoom lens, depth of field, hyper focal distance**

I. Introduction

Multi sensor – multi spectral surveillance system users prefer application of the zoom lenses in the built in camera systems. Motorized zoom lens provides flexibility and controllability of the imaging conditions: changing the focal length, focusing distance, and aperture value to suit different fields of view (FOVs), depths of field (DOFs), and lighting conditions. Digital image sensor and application of the computer for surveillance system control provides technical means for convenient and accurate imaging data analysis and camera operation control using pre-set and calibration data generated in the laboratory.

Zoom lens calibration is described in open literature mainly for zoom lens application in photogrammetric measurement and machine vision application [1-8]. Camera calibration is a prerequisite for 3D imaging applications, providing data for 3D reconstruction. The calibration procedures could be identified as: standard calibration, self-calibration, photometric calibration and stereo-setup calibration. There are a lot of techniques applied for specific applications, but calibration of the surveillance zoom camera aimed for object pointing and tracking is poorly covered in the open literature. In this application [9] the most important is so called "zoom to FOV" calibration, involving lens optical axis stability calibration and line of sight – LoS control, using position control of the sighting reticle. Zoom lens focal length and image focus is set with digitally controlled positioning motors. "Zoom to FOV" calibration provides connection between motor position digital data and related zoom lens focal length or camera FOV. LoS stability control against zoom motor position is provided using data of optical axis displacement versus zoom motor position. This zoom lens calibration in surveillance systems provides accurate system aiming and target tracking. Sharp image is provided by additional camera focus control.

The long range surveillance system should provide wide field of regard – FOR (target search over wide area and different ranges) and possibility to provide high magnification in the same time. High magnification means that imagers use narrow field of view that is incompatible with wide FOR. This discrepancy could be overridden using zoom function. FOR search is done using wide FOV for target detection, and switch to narrow FOV for target recognition and identification. Human operator is usually involved in the system control chain. To support fast switching from wide FOV to suitable narrow FOV several zoom (FOV) pre-set positions are defined. To avoid additional time loss for focus adjustment it is convenient to pre-set focus motor position and provide sharp image immediately after switching to desired FOV. One of the possible solutions is to use idea about hyper-focal distance that is widely used in the cinema industry and photography [10].

In this article we are describing the basic design and properties of the motorized zoom lenses. We are pointing out zoom lens specifics leading to imperfections that should be corrected by calibration, together with definition of the main geometrical relations in the camera system. Also we described our simplified model for hyper-focal distance calculation applied for motorized zoom lens cameras used in our systems. The methodology for implementation of these results to camera pre-set parameters is explained.

Saša Vujić is with Vlatacom Institute of High Technologies, 5 Bulevar Milutina Milankovića, 11070 Belgrade, Serbia (e-mail: sasa.vujic@vlatacom.com).

Dragana Perić is with Vlatacom Institute of High Technologies,, 5 Bulevar Milutina Milankovića, 11070 Belgrade, Serbia (e-mail: dragana.peric@vlatacom.com).

Branko Livada is with Vlatacom Institute of High Technologies, 5 Bulevar Milutina Milankovića, 11070 Belgrade, Serbia (e-mail: branko.livada@vlatacom.com).

In the case of zoom lens calibration and set-up, common camera calibration should be conducted first. Camera calibration is the process of determining the intrinsic parameters of the camera, including back focus distance.

A zoom lens contains moving lens groups providing focal length change that could be moved using linear or rotational stages powered by electrical motor. To provide high effectivity of zoom lens controllability, lens calibration and initial set-up should be performed.

The focus adjustments for selected zoom pre-set positions is the last step in camera setting.

II. Zoom Lens Design and Basic Properties

Imaging zoom lens is capable of producing, on a fixed plane (image plane), images whose magnification is continuously variable between two extreme values. The variation in magnification is achieved by changing the relative positions of the lens elements or lens groups built in the zoom system. The zoom lens design is complex [11-18], including complicated mechanical motion system design and optical design and optimization, depending on dedicated zoom lens system application. Because of that, zoom lenses were not considered for high quality imaging application until 1960, when started wider application in commercial photographing systems.

Two broad classifications of the zoom systems recognize the mechanically compensated type and the optically compensated type. In mechanical compensation design, the motions given to the elements are such as to ensure exact constancy of focal position, these movements being non-linear and achieved by complicated camera mechanisms. In an optically compensated design the motion of all moving elements is identical and linear, but desired focus can be achieved only at a finite number of zoom positions.

The development of the digital imaging sensors leading to the small sensor size accompanied with aspherical lenses provides leads to the much wider applications of the zoom lens systems [14]. Long range surveillance application in visible and infrared region, requiring continuous focus caused that mechanically compensated zoom lens using fine motorized controls dominates in practical applications.

The zoom lens generalized structure is presented in Fig.1 showing the key fixed and moving (controllable) components. The illustration of complexity of zoom lens design is shown in in Fig.2.

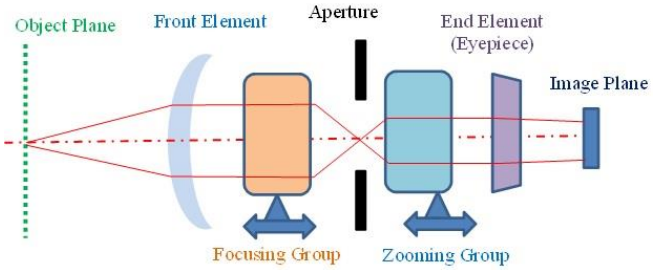

Fig. 1. Zoom Lens generalized structure

Zoom lens elements are grouped to provide basic functions: focusing group, magnification variation group, correction group and image formation group. The magnification variation group and correction group could be moved during zooming. Focusing group could be moved during focusing process that could be performed simultaneously or follow on zooming. Image formation group is usually fixed and belong to the end piece of lens, providing enough space to image plane where imaging sensor is placed (back focus distance).

Back focus distance is the distance along optical axis from the apex of the rearmost glass surface to the focal plane when a lens focused to infinity.

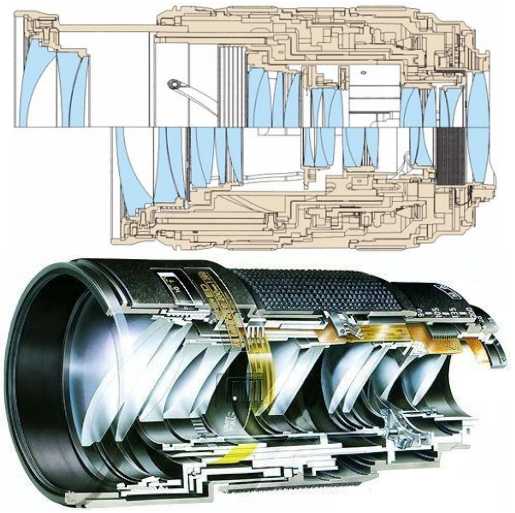

Fig. 2. Zoom lens design example illustration (cross section)

The advances in the optical design and manufacturing process [19], provides high quality for manufactured zoom lenses, but there are still imperfections that remain and that should be corrected during initial lens calibration. Some of them are caused by zoom lens mounting, as illustrated in Fig.3

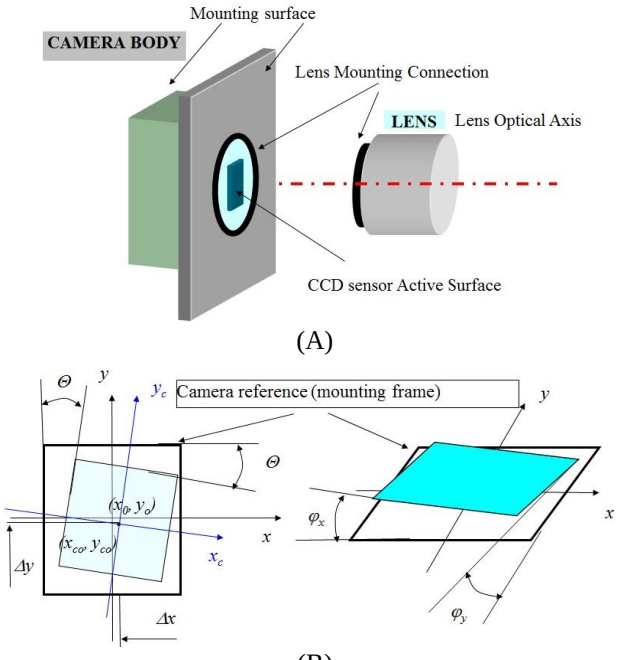

Fig. 3. Zoom lens mounting (A) Back focal distance; (B) Imperfections (Image sensor rotation and tilt)

In the case of surveillance cameras the position image sensor center and optical axis are the most important [20].

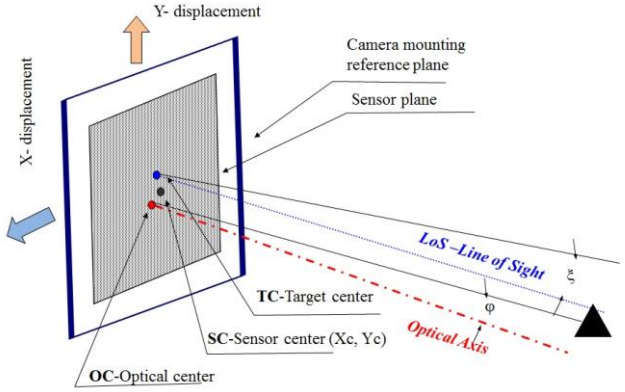

Fig. 4. Zoom lens camera calibration parameters geometry

The fusion of digital image, zoom lens magnification and focus digital control, provides the basis for development of the different calibration procedures that contribute to the effective zoom lens operation in related applications [20-25].

In this article we are dealing with zoom lens calibration to provide reasonably sharp image (according to allowable tolerances of focus [26]) during zoom focal length change but avoiding manual focus fine adjustment. This is of importance in the long range surveillance system application when fast reaction increase system efficacy.

Motorized zoom lenses have great potential in the applications long range surveillance systems providing object of interest - target and visual perception (detection, recognition, identification) and tracking. In such applications, the aperture, zoom, and focus of the lens can be controlled to adapt to different lighting conditions or to obtain the desired field of view, depth of field, spatial resolution, or focused distance. Calibration of a motorized zoom lens is extremely useful but not an easy job. The goal of motorized zoom lens calibration is to determine the relationship between the lens position settings (control parameters for the driving motors) to provide proper imaging performances. In our case we are establishing lens position settings for selected pre-set positions to provide sharp image immediately after zoom position change. In that case zoom lens is treated as mono-focal lens for selected FOV.

III. Hyper-focal Distance and Depth of Field

To provide calibration and set-up procedure we selected to explore the idea of hyper-focal distance that was widely used in first half of twentieth century for focus setting in photography and cinema industry [10, 27]. It is still explored in photography for achieving of the special effects in artistic photography.

Hyper-focal distance can be defined as distance in front of camera upon which all objects in front of that distance and up to infinity appears sharp in image. In other words, if you want everything to be acceptably sharp from infinity to as close as possible to the camera you should focus on the hyper-focal distance.

As a first step we need to discuss some important parameters:

Stop diaphragm - aperture: The opening which adjusts the diameter of the group of light rays passing through the lens. The zoom lens maximal aperture is limited by lens entrance element diameter. To provide possibility to regulate amount of the light the controllable stop diaphragm – iris is built in lens system to limit light bundle passing through lens but not disturbing image. In modern digital cameras aperture adjustment is commonly controlled automatically using command from image sensor to avoid sensor saturation. The control could be complex because saturation is controlled by exposure time, too.

Focal length: When parallel light rays enter the lens parallel to the optical axis, the distance along the optical axis from the lens' second principal point (rear nodal point) to the focal point is called the focal length. In simpler terms, the focal length of a lens is the distance along the optical axis from the lens' second principal point to the focal plane when the lens is focused at infinity.

F-number – F#: For zoom lens having aperture with diameter *d* and focal length *f* related lens F-number is defined as:

$$F_{\#} = \frac{f}{d} \tag{1}$$

Circle of confusion – CoC: Since all lenses contain a certain amount of spherical aberration and astigmatism, they cannot perfectly collect rays from a subject point to form a true image point. In addition, diffraction widening also contributes to the focused spot size. In the case of infrared lenses diffraction limited lenses are more often case. Since the image becomes less sharp as the size of these dots increases, the dots are called "circles of confusion". The advancement of the optical design and manufacturing technology practically eliminate the aberrations influence on CoC through proper compensation and optimization in design process, but diffraction influence could not be eliminated.

Diffraction limited resolution is defined by so called Rayleigh's criterion [28, 29] defined by diameter of the first Airy disk on point spread function. In that case one can to define that minimal value of CoC is equal to:

$$c = CoC = 2{,}44 \cdot \lambda \cdot F_{\#} \tag{2}$$

Sensor size: Imaging focal plane array contains the matrix of detectors – pixels having limited size, *p*. The final factor determining hyper-focal distance is the size of your digital sensor. A larger digital sensor will result in a closer hyper-focal distance.

Depth of focus is a space around focal plane in which acceptable sharp image could be achieved. Depth of focus in the image-space is related to how the quality of focus changes on the sensor side of the lens as the sensor is moved, while the object remains in the same position. Depth of focus, δ, could be calculated as:

$$\delta = 2 \cdot F_{\#} \cdot s \tag{3}$$

Where *s is* resolution limit (*s=p* – detector limited, *s=c* – diffraction limited)

Depth of focus characterizes how much tip and tilt is tolerated between the lens image plane and the sensor plane itself. As $F_{\#}$ decreases, the depth of focus does as well, which increases the impact that tilt has on achieving best focus across the sensor. Without active alignment, there will always be some degree of variation in the orthogonality between the sensor and the lens that is used. It is generally assumed that problems involving depth of focus only occur with large sensors.

Depth of field – DoF: The space in front of and behind an imaged object having sharp focus, image also appears sharp. In other words, the depth of sharpness to the front and rear of the subject where image blur in the focal plane falls within the limits of the permissible circle of confusion. Depth of field (as illustrated in Fig.5) varies according to the lens' focal length, aperture value and object distance (D_{pof}), so if these values are known, a rough estimate of the depth of field can be calculated using the following formulas:

$$D_{near} = \frac{f^2 \cdot D_{pof}}{f^2 + F_{\#} \cdot c \cdot (D_{pof} - f)} \quad (4)$$

$$D_{far} = \frac{f^2 \cdot D_{pof}}{f^2 - F_{\#} \cdot c \cdot (D_{pof} - f)} \quad (5)$$

$$DoF = D_{far} - D_{near} \quad (6)$$

$$D_{HF} = \frac{f^2}{F_{\#} \cdot c} \quad (7)$$

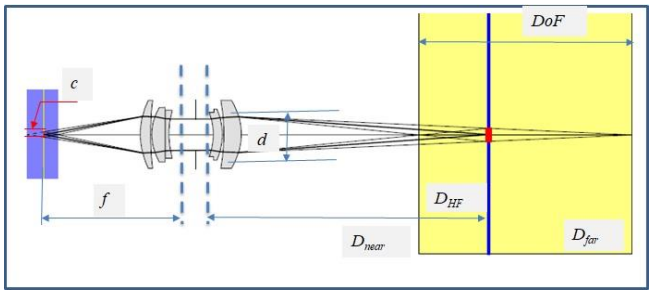

Fig. 5. Depth of focus and depth of field definition

Hyper-focal distance is a distance of object whose image is sharp same as all other far objects up to infinity and other near objects up to half of hyper-focal distance. It depends of the same three factors that determine depth of field.

Hyper-focal distance allows precise setting of the focus so that everything between half the hyper-focal distance and infinity is acceptably sharp. That means if one set proper focus of object placed on hyper-focal distance then all objects placed at distances from half of hyper-focal distance to infinity will have acceptable sharpness.

However, sharpness does not depend on focus setting alone. Camera motion, subject motion by wind, quality of the lens, weather, and other factors can greatly impact the sharpness of the image.

IV. Long Range Zoom Camera Focus Settings

The calculations of the hyper focal distance against focal length setting using equitation (7) were applied for selected cameras having characteristics listed in TABLE I.

TABLE I
CONDENSED REVIEW OF THE IMAGER BASIC PARAMETERS

System Type	Focal Length [mm]		F#		Pixel Size [μm]	Center λ [μm]
	min	max	min	max		
VOXI-LWIR	25	225	1,5	1,5	17	10
VOXI-SWIR	25	300	2,8	>30*	15	1,5
VOXI-VIS	23	506	3,1	>30*	6,25	0,55
C225	23	506	3,1	>30*	8,3	0,55
C1200	12	1680	4	18,2	5	0,55
C2500	33,4	2000	3,5	16	5	0,55

Note*: * - with iris control*

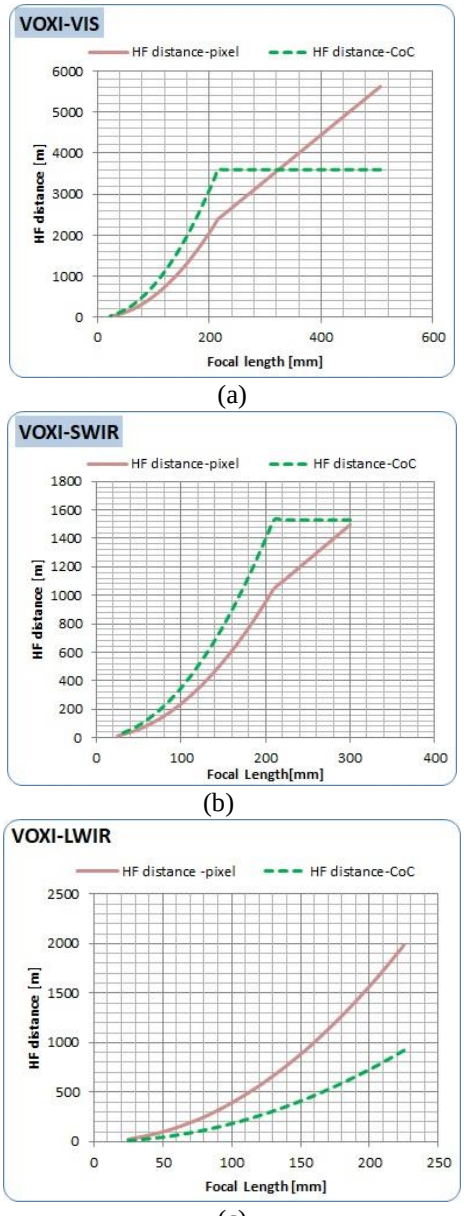

Fig. 6. Calculated hyper-focal distance value versus lens focal length for different cameras (VIS –visible, SWIR- short wavelength infrared, LWIR – long wavelength) in VOXI system

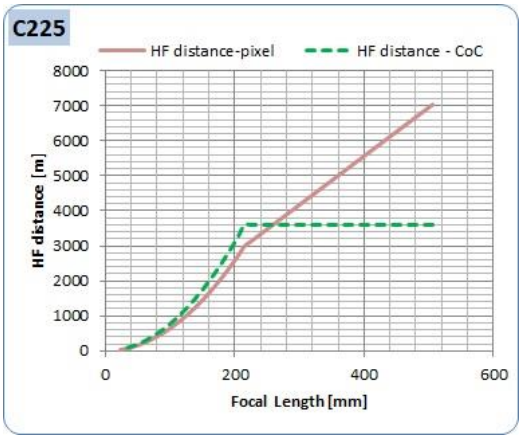

Fig. 7. Calculated hyper-focal distance value versus lens focal length for VIS camera in C225 system

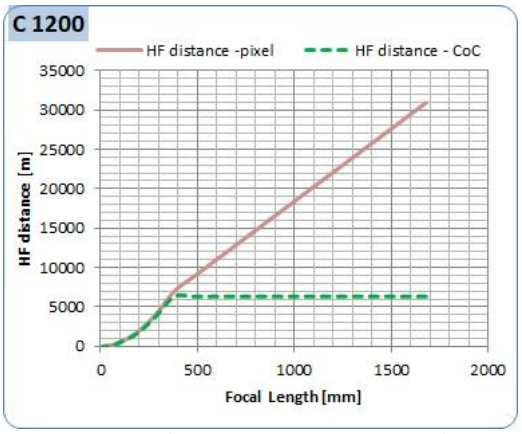

Fig. 8. Calculated hyper-focal distance value versus lens focal length for VIS camera in C1200 system

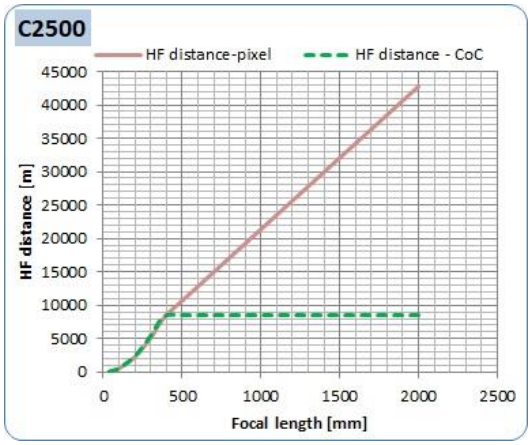

Fig. 9. Calculated hyper-focal distance value versus lens focal length for VIS camera in C2500 system

The results of hyper-focal distance calculations for medium range surveillance system and different imagers are shown in Fig.6. These results show that application of proper set-up will be effective in all three channels.

The results of hyper-focal distance calculations for long range systems (VIS imagers with different magnification) are shown in Fig 7 to Fig.9. These results show that hyper-focal distance based focusing setting could be useful for wide FOVs (focal lengths up to 400 mm) but for narrow FOV it is good enough to use just infinity focus settings.

The application of hyper-focal distance based zoom lens focusing parameter settings can contribute to improvements to system performances but have limited capabilities: (a) calibration process could be applied only for limited and predefined pre-set FOV positions; (b) it is effectively applicable only for zoom lens wide FOV pre-set positions; (c) practical implementation is not easy and reliable enough; (d) the influence of temperature on zoom lens focus stability is not involved in the procedure.

The good news is that additional manual focus setting is always allowable to system operator to try to improve image sharpness.

The application of collimator for focus setting following hyper-focal distance data is not practical in the case of long range imagers, so determination of the imager focus setting should be performed using real objects imaging in the field.

The setting procedure could be established as follows: (I) select the object in the field on the distance that is approximately as calculated hyper-focal distance for selected pre-set FOV (focal length); (II) starting from infinity focusing settings, change the focus setting to get selected object properly focused; (III) continue changing focus setting keeping object focused same as all other objects far from selected object; (IV) at the moment when very far objects (infinity) start to loose sharpness but selected object is still sharp record focus settings. This value could be set as selected focus setting for the FOV pre-set value according to hyper-focal distance.

V. Conclusion

Video channel functional parameter optimization is not simple task, but possibilities depends on image formation process knowledge including lens properties, imaging sensors properties and incorporated camera controls including image processing algorithms.

Application of the zoom lenses in the long range imaging systems is convenient for search and track task over all ranges but diffraction effects at high zoom degrades imaging sensor resolution. Image blurring is inherent to high magnification imaging systems due to lower contrast and high level of diffraction and atmospheric influences. Initial zoom lens set up can help but problem could be solved only by additional image processing algorithm application.

Motorized and controllable zoom lenses together with digital image allow wide range of computer application for application of digital controlled calibration procedures contributing to image quality/sharpness improvements. Camera focusing parameter set-up using hyper-focal distance is calibration process.

The application of the hyper-focal distance concept for camera initial set up provides faster and more comfort operation, but could not contribute alone to image quality/sharpness improvement.

Digital image quality and sharpness depends on lot of

factors and could be improved by application of the de-blurring algorithms using the knowledge about physical process causing image blur.

ACKNOWLEDGMENT

We kindly appreciate our colleague Saša Milićević, passionate photographer, who proposed the idea to exploite hyper-focal distance for system focus set-up.

REFERENCES

[1] Shirazi Muhammad Ayaz, Min Young Kim, Jaechan Park, Survey on zoom-lens calibration methods and techniques", *Machine Vision and Applications*, July 2017

[2] Y.Seo and K.S.Hong, "Theory and practice on the self-calibration of a rotating and zooming camera from two views", *IEE Proc.-Vis. Image Signal Process., Vol. 148, No. 3*, June 2001

[3] Andrea Pennisi, Domenico Bloisi, Claudio Gaz, Luca Iocchi, Daniele Nardi, "Novel Patterns and Methods for Zooming Camera Calibration", *Journal of WSCG*, Volume 21, Number 1, 2013, pp, 59-67

[4] Fabio Remondino, Clive Fraser, "Digital Camera Calibration Methods: Consideration and Comparisons", *IAPRS Volume XXXVI, Part 5*, Dresden 25-27 September 2006

[5] S.S. Al-Ajlouni , C.S. Fraser, "Zoom- dependent Calibration for Consumer Grade Cameras", *IAPRS Volume XXXVI, Part 5*, Dresden 25-27 September 2006

[6] Reg G. Willson "Modeling and Calibration of Automated Zoom Lenses", *Proceedings SPIE Volume 2350*, Videometrics III; Photonics for Industrial Applications, Boston, MA, United State, 6 October 1994

[7] Suchi Upadhyay, S.K.Singh, Manoj Gupta, Ashok K. Nagawat, "Linear and Non-linear Camera Calibration Techniques", *Journal of Global Research in Computer Science*, Volume 2, No. 5, April 2011

[8] Bo Wu, Han Hu, Qing Zhu, and Yeting Zhang, "A Flexible Method for Zoom Lens Calibration and Modeling Using a Planar Checkerboard", *Photogrammetric Engineering & Remote Sensing*, Vol. 79, No. 6, June 2013, pp. 555–57

[9] Branko Tomić, Dragana Perić, Miloš Radisavljević, Saša Vujić, „Reticle Integration and Camera Calibration in Multi Sensor Surveillance Systems", *8th International Conference on Defensive Technologies, OTEH 2018*, Belgrade, Serbia, 11-12 October 2018

[10] Rowlands, D. Andrew, *Field guide to photographic science*, SPIE Press, Bellingham, USA, 2020

[11] Allen Mann : "*Infrared Optics and Zoom Lenses"*, Vol. TT42, SPIE Press, Bellingham, USA, 2009

[12] A.D Clark; "*Zoom Lenses*", Monographs in Applied Optics No7, Adam Holger, London, 1973

[13] K. Yamaji: "*Design of Zoom Lenses*" ch.4 in "Progress in Optics" vol.6 (edited by E. Wolf), NORTH-HOLLAND PUBLISHIXG COMPANY, Amsterdam, 1967

[14] Richard N.Youngworth, Ellis I. Betensky: "Fundamental Considerations for Zoom lens Design (Tutorial)", *Proc. of SPIE,* Vol. **8488** p. 848806-1, 2012

[15] Allen Mann: "Infrared zoom lens system for target detection", Optical Engineering, Vol. 21 No. 4, pp.786-793, 1982

[16] Thomas H. Jamieson: „Thin-lens theory of zoom systems", OPTICA ACTA, VOL. 17, NO. 8, 565—584, 1970

[17] Antonín Mikš, Jiří Novák, and Pavel Novak: "Method of zoom lens design", *Applied Optics*, Vol. 47, No. 32, pp. 6088-6098, 2008

[18] D. Dilworth: "A zoom lens from scratch: the case for number crunching", *Proc. SPIE*. 9947, 994702, 2016

[19] Robert E. Fischer, Biljana Tadic-Galeb, Paul R. Yoder: "*Optical System Design*", The McGraw-Hill Companies, Inc., New York, 2008

[20] Reg G. Willson, Steven A. Shafer, "What is the center of the image?", *J. Opt. Soc. Am. A* ,/ Vol. 11, No. 11/, November 1994

[21] Zheng Wang, Jon Mills, Wen Xiao, Rongyong Huang, Shunyi Zheng and Zhenhong Li, "A Flexible, Generic Photogrammetric Approach to Zoom Lens Calibration", *Remote Sens.* 2017, 9, 244

[22] Yong-Sheng Chen Sheng-Wen Shih, Yi-Ping Hung, Chiou-Shann Fuh, "Camera Calibration with a Motorized Zoom Lens", *Proceedings of the 15th International Conference on Pattern Recognition*, Barcelona, Spain, Sep. 2000, Volume 4, pages 495–498

[23] Anthony G. Wlley and Kam W. Wong, "Geometrical Calibration of Zoom Lenses for Computer Vision Metrology", *Photogrammetric Engineering & Remote Sensing*, Vol. 61, No. 1, January 1995, pp. 69-74

[24] Yong-Sheng Chen, Sheng-Wen Shih, Yi-Ping Hung, Chiou-Shann Fuh: " Simple and efficient method of calibration a motorized zoom lens", *Image and Vision Computing*, 19, 1099-1110, 2001

[25] Ziyan Wu, and Richard J. Radke: „Keeping a Pan-Tilt-Zoom Camera Calibrated", *IEEE TRANSACTIONS ON PATTERN ANALYSIS AND MACHINE INTELLIGENCE*, pp 1-14, 2012

[26] S.G. Shiue, „Tolerances for Focus Stability in Zoom Lenses", *Optica Acta: International Journal of Optics*, 32:8, 923-936, 1985

[27] Sidnay F. Ray: "*Applied Photographic Optics: Lenses and optical systems for photography, film, video, electronic and digital imaging*", third edition, Focal Press, Oxford, 2002

[28] A. J. den Dekker and A. van den Bos: „Resolution: a survey", *J. Opt. Soc. Am. A* , Vol. 14, No. 3, 547-557 , 1997

[29] Sisi Zhou and Liang Jiang: "A modern description of Rayleigh's criterion", *Phys. Rev. A* , 99, 013808, 2019

Temperature influence on the performance of P3HT:ICBA polymer solar cells

Ali R. Khalf, Jovana P. Gojanović, Nataša A. Ćirović, Petar S. Matavulj, *Member, IEEE*, Grant Ledet, Mark Hidalgo and Sandra Živanović, *Member, IEEE*

***Abstract*—Temperature (*T*) dependent performance of polymer solar cells (PSCs) with a poly (3-hexylthiophene): indene-C_{60} bisadduct (P3HT:ICBA) active layer were investigated. The current-voltage *(I-V)* characteristics of devices with two different active layer thicknesses (ALTs) were measured within a temperature range of 20 °C-65 °C. The recorded *I-V* curves showed the S-shape deviation. The *I-V* curves were also simulated by a standard drift-diffusion model that includes the influence of the surface recombination on both electrode contacts. The Arrhenius-type temperature-dependent hole mobility was introduced to reproduce the experimentally observed temperature-dependent PSC behavior. The measured power conversion efficiency (PCE) and short-circuit current *(I_{sc})* changed non-monotonically with *T* whereby detailed temperature trends differed for solar cells of different ALTs. The noticed effects were not present in theoretically predicted PCE and I_{sc}. To match the simulated and experimental *I-V* characteristics the PCS internal quantum efficiency (IQE) was varied with *T*. We suggest that the obtained nonmonotonic IQE(*T*) dependence originates from changes in morphology caused by the influence of temperature and strongly correlates to the P3HT:ICBA thin-film thickness.**

***Index Terms*—P3HT; solar cells; simulation; temperature.**

I. Introduction

POLYMER-based bulk-heterojunction solar cells (PSCs) are an emerging renewable energy technology that enables easy, low-cost and low-environmental impact production and yields lightweight, flexible devices with the possibility of visible transparency, and large surface area. Power conversion efficiency (PCE) of PSCs has drastically improved during the last decade, surpassing 18% for single-junction cells [1], and 18.6% for tandem cells [2]. Enhancement of PCE has been accomplished through several different developmental directions. A crucial issue regarding polymer-based solar cells is how to manage the energy levels of the donor/acceptor (D/A) blends to maximize short-circuit current (I_{sc}) and open-circuit voltage (V_{oc}) at the same time without sacrificing the efficient charge separation [3, 4]. New donor [3, 4] and acceptor [5] materials were synthesized to accomplish this goal. Optimization of process parameters [6], annealing [7], aggregation, and morphology control [8] were used to improve the charge transport in PSCs. Much better extraction of charge carriers was accomplished by introducing the hole and electron buffer layers [9]. Optical manipulation of light has become an increasingly popular strategy to capture solar radiation more effectively into an ultrathin photoactive layer of PSC thus to enhance the light-harvesting efficiency [10, 11].

In the meantime, a lot of theoretical research has been done resulting in the first PSC drift-diffusion model (DDM) developed by Koster et al. in 2005 [12]. A long time ago, it was established that interferential effects play a significant role in organic thin-film photovoltaic devices [13]. Therefore, an optical model based on transfer matrix formalism was soon coupled to drift-diffusion calculations, completing the image of important physical processes in PSC [13]. This model including different modifications and updates is successfully used to simulate the performance of PSC with various structures and D/A material combinations. It is also a powerful tool for the investigation of physical phenomena that undergo PSC operation [14, 15] as well as for device optimization [16]. Besides the drift-diffusion approach, some equivalent circuit models have also been proposed [17]. These models introduce the other point of view, and they account for additional electrical PSC features not included in the DDM such as parasitic resistivities and other parasitic effects. Another field that the DDM does not cover in a sufficiently detailed way is the impact of morphology and nanoscale physical processes on the efficiency of PSC. Through Monte Carlo and multiscale simulations [18], one can approach the nanostructure of the active layer and follow the excitonic and charge carrier pathways. This can lead to some crucial conclusions and hints for the fabrication of highly efficient PSC.

Summarizing the state of the art in the field of PSCs, it becomes clear that there is a lot of room for additional research by physicists, chemists, and technologists to improve PSC efficiency towards their commercialization.

It is well known that temperature and light intensity dependence of optoelectronic device performance gives a good insight into the physical processes underlying its operation. Such measurements were carried out on the PSCs to study the photogeneration and transport of charge carriers [19, 14, 15, 20 21] as well as the mechanisms of their recombination [22, 23, 24, 20]. According to our knowledge only a few papers in the literature have been dedicated to the investigation of PSC *I-V* curve temperature-dependence and consequently I_{sc}, V_{oc}, fill factor (FF), and PCE temperature dependences [25, 26, 27, 28, 29, 30, 20]. Among these papers just one presents the DDM model that includes the PCS temperature dependent behavior, unfortunately, without matching the model results to any experimental data [20]. Knowing the influence of the temperature on PCS performance is very important to predict the operation of the device in standard working conditions as well as for further progress in PCE optimization. To prevent unnecessary

A. R. Khalf, J. P. Gojanović, N. A. Ćirović, and P. S. Matavulj are with the School of Electrical Engineering, University of Belgrade, Belgrade 11120, Serbia (e-mail: alirkhalf@yahoo.com; jovana@etf.bg.ac.rs; natasa@etf.bg.ac.rs; matavulj@etf.bg.ac.rs).

G. Ledet, M. Hidalgo and S. Živanović are with Institute for Micromanufacturing, Louisiana Tech University, Ruston, LA 71272 USA (e-mail: grantledet@gmail.com, mkhidalgo@charter.net, sz@latech.edu).

expenses, a useful model is needed to simulate temperature-dependence of PSC.

In this paper ITO(indium tin oxide)/PEDOT:PSS (poly(3,4-hylenedioxythiophene):poly(styrenesulfonate))/P3HT:ICBA (poly(3-hexylthiophene):indene-C_{60} bisadduct)/Al solar cells with two different thicknesses of P3HT:ICBA active layer were fabricated and tested in the 20 °C to 65 °C temperature range. The S-shaped *I-V* characteristics were recorded under solar simulator light from which I_{sc} and PCE dependences on T were determined for each device. The device performance was simulated by the standard drift-diffusion model (DDM) that accounts for surface recombination on electrodes. The Arrhenius-type temperature-dependent hole mobility was applied [15]. It was found that the experimental PCE and I_{sc} vary non-monotonicaly with temperature (T). Also, temperature caused variation of PCE and I_{sc} for two devices with different active layer thicknesses (ALTs) was different. The DDM calculated solar cell parameters did not show such behavior. To match the simulated and measured *I-V* curves it was necessary to introduce the temperature-dependent internal quantum efficiency (IQE) of PSCs. The surface recombination was also taken to be temperature-dependent. The nonmonotonic change of IQE with T obtained in this way was attributed to the change of P3HT:ICBA film morphology which is, on the other hand, correlated to the active layer film thickness [31].

II. Experiment

PSC devices with glass/ ITO/ PEDOT: PSS/ P3HT:ICBA/ Al device structure were fabricated and tested at Institute for Micromanufacturing, Louisiana Tech University.

P3HT and ICBA from Sigma Aldrich with 1:0.78 wt. ratio were mixed with chlorobenzene separately and kept on a hot plate with a magnetic stirrer at 50 °C overnight. PEDOT:PSS HTL Solar Heraeus Clevios water solution from Ossila was spin-coated at 3500 RPM to deposit about 50 nm-thick film and was then annealed at 115°C for 10 min. The P3HT:ICBA solution was then statically dispensed with a micropipette onto the ITO coated boro-aluminosilicate glass substrate (Delta Technologies) and spin-coated at 900 RPM and 1450 RPM to deposit approximately 90 nm and 67 nm-thick films, respectively. The P3HT:ICBA thin films were baked at 70 °C for 5 minutes to remove any residual solvent. Afterwards, a 110 nm aluminum layer was deposited as a cathode in the e-beam evaporator, and then the devices were annealed at 150 °C for 15 min on a conventional hot plate. The active area of each device was about 0.9 cm^2.

Devices were illuminated with AM1.5 spectra of 50-60 mW/cm^2 optical power density from Spectra Physics 66900 solar simulator. The incident optical power density was measured with a Newport Oriel 91150V reference cell and meter. To control the temperature of the solar cells for testing, a thermoelectric Peltier module with a DC voltage supply, which uses voltage to change the temperature on the plates, was used. A non-contact infrared thermometer was also used to monitor the temperature. The *I-V* curves were measured for the temperature range from 20 °C to 65 °C using Keithley 2400 source meter. Fig. 1 (a_1) and (b_1) show experimentally obtained *I-V* curves under solar simulator illumination. From the *I-V* characteristics, the corresponding temperature-dependent I_{sc} and PCE were determined (Fig. 1 (a_2), (a_3), (b_2), and (b_3)).

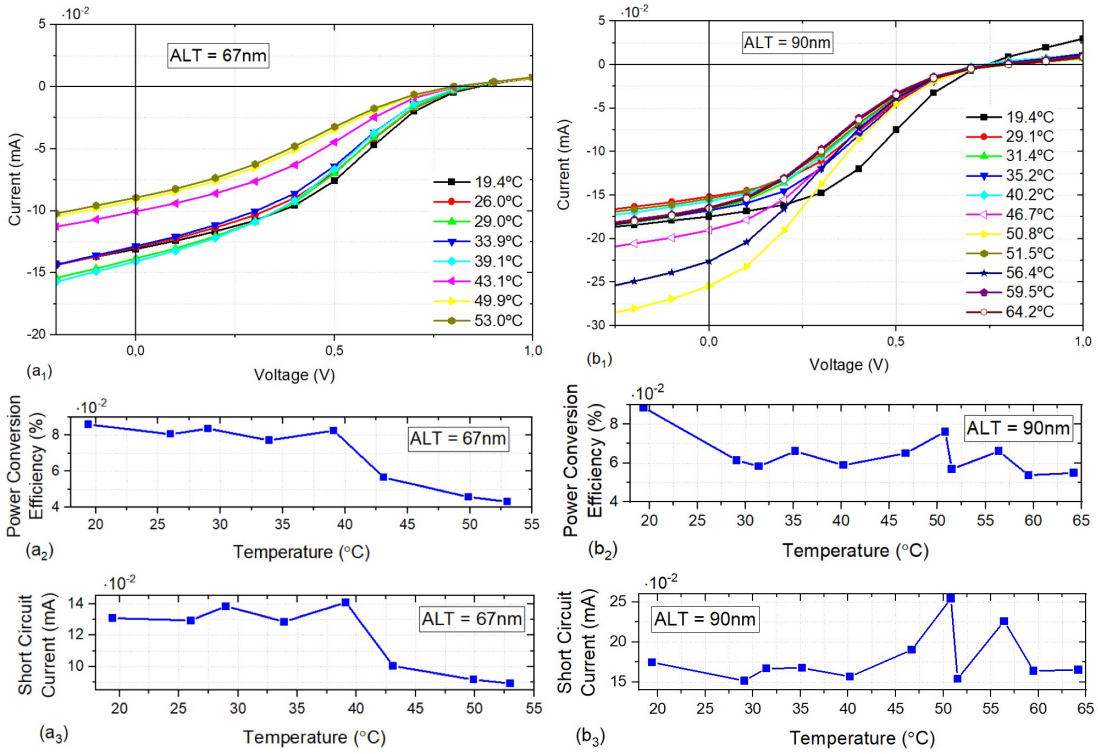

Fig. 1. Measured I-V characteristics of ITO/PEDOT:PSS/P3HT:ICBA/al solar cells with (a1) 67 nm and (b1) 90 nm active layer thicknesses at different Temperatures; (a2) and (b2) PCE and (a3) and (b3) Isc temperature dependencies for the same devices, respectively.

III. Model

To simulate the temperature dependence of ITO/PEDOT:PSS/P3HT:ICBA/Al solar cell characteristics, we used the DDM described in our previous research [32]. The Robin type boundary conditions which account for surface recombination on electrode contacts were applied [33]. Generation rate of charge carriers in the active layer was calculated using the transfer matrix method (TMM) which takes into account interference effects in the device [13]. The optical constants, refraction index, and extinction coefficient used in the TMM were determined from optical measurements that also take the interference effects in the thin organic films into account. As the transport mechanism of holes and electrons in polymer:fullerene blends are strongly thermally activated [14, 15], we supposed that temperature-dependent behaviour of ITO/PEDOT:PSS/P3HT:ICBA/Al solar cell is predominantly governed by temperature-dependent mobilities. Since mobility temperature dependence is much weaker for electrons than for holes [29], we assumed a constant electron mobility and an Arrhenius-type [15] temperature-dependent hole mobility:

$$\mu_p = \mu_{p0} e^{-\frac{\Delta}{k_b T}} \quad (1)$$

where μ_{p0} is a mobility prefactor, Δ is the activation energy, k_b Boltzmann's constant, and T the absolute temperature. The numerical DDM solution includes the Sharfetter-Gummel approach. All the other model methods and assumptions are the same as in [32].

IV. Results and Discussion

The *I-V* characteristics for two ITO/PEDOT:PSS/P3HT:ICBA/Al devices with 67 nm and 90 nm thick P3HT:ICBA active layer measured at several different temperatures between 20 °C to 65 °C are shown in Fig. 1 (a_1) and (b_1). Both devices exhibit pronounced S-shape deformation. The deformation most likely originates from the aggravated extraction through the Al electrode and a consequent accumulation of the charge carriers. The PCE and I_{sc} as functions of T for two examined PSCs are presented in Fig. 1 a_2, a_3, b_2, and b_3. The non-mnotonic change of PCE and I_{sc} with temperature is apparent for both devices. While the PCE(T) had an overall decreasing character, the maximum of I_{sc} was obtained around 40 °C for the solar cell with 67 nm ALT and around 50 °C for the solar cell with 90 nm ALT. The tested devices had rather small PCE values due to inefficient cathode extraction.

The DDM simulations were conducted by using the parameter values given in Table 1. Because of the S-shape experimental *I-V* characteristics anomaly, it was proposed that surface recombination of electrons was pronounced at the cathode contact. The surface recombination velocities (SRVs) on the anode contact were taken to be infinite, while the electron SRV on the cathode was assumed to be reduced (Table 1). The calculated *I-V* curves for the 67 and 90nm ALT devices for the same T values at which the measurements were done are shown in Fig. 2 (a_1) and (b_1). The corresponding PCE(T) and $I_{sc}(T)$ were determined and depicted in Fig. 2 (a_2), (a_3), (b_2), and (b_3). From Fig. 2 (a_2) and (b_2) it can be noticed that theory predicts a slightly increasing trend for PCE(T). Also, the increasing trend for $I_{sc}(T)$ is obtained from calculations as can be seen from Fig. 2 (a_3) and (b_3). Since the experimental results given in Fig. 1 are qualitatively poorly reproduced by the model, a conclusion was drawn that the DDM which includes the effect of temperature on the PSC performance only through Arrhenius T-dependent hole transport is not adequate. Apparently, there are other processes that are significantly affected by T.

TABLE 1
The Parameters for ITO/PEDOT:PSS/P3HT:ICBA/Al Solar Cells

Symbol	Quantity	Value
E_g	Energy gap	1.4eV
ε_r	Relative permittivity	3.4
N_C, N_V	The effective densities of states	1×10^{26} m^{-3}
μ_{p0}	Hole mobility	3 cm^2/(V·s)
μ_n	Electron mobility	4.92×10^{-4} cm^2/(V·s)
Δ	Activation energy	0.3eV
IQE	Internal quantum efficiency	0.05
τ_n	Electron lifetime	6.2×10^{-5} s
τ_p	Hole lifetime	3×10^{-7} s
S_n^c	Electron SRV at the cathode	9.6×10^{4} cm/s

When a photon is absorbed in the PSC's active layer, the Coulombically bound electron-hole pair constituting an excitonic state is produced. It is known that temperature plays an important role in exciton dissociation [19, 34]. First, the charge transfer (CT) state is made at the donor/acceptor junction and some additional energy is needed to complete the dissociation. Thermal energy can be used for the separation of the CT state into free carriers [19, 34]. Knowing that the photogeneration in PSCs is affected by temperature, we attempted to reproduce the PSCs *I-V* characteristics at different T by letting the IQE be T-dependent and used it as a fitting parameter. The electron SRV on the cathode is also expected to change with T since it is essentially the Shockley-Read-Hall recombination through the surface trap states. For this reason, the SRV for electrons on the cathode was taken to be variable. When the IQE and electron SRV on the cathode were changed with T, a very good agreement between experimental and simulated *I-V* data was accomplished. The comparison of measured and DDM calculated *I-V* curves for solar cells with 67 nm and 90 nm ALTs for three selected temperatures is shown in Fig. 3. The built-in voltage was also slightly changed with temperature, which is denoted on each *I-V* graph. The IQE and SRV values at different T obtained for the two considered PSCs are presented in Table 2. The IQE changed with T in a nonmonotonic fashion, which was not the same for devices with different ALTs. This can be attributed to the P3HT:ICBA film morphology changes caused by the temperature and correlated to the film thickness [31]. On the other hand, the electron SRVs on the cathodes for both devices were decreasing with T, reflecting the fact that the surface (trap-assisted) recombination becomes more pronounced with increasing T.

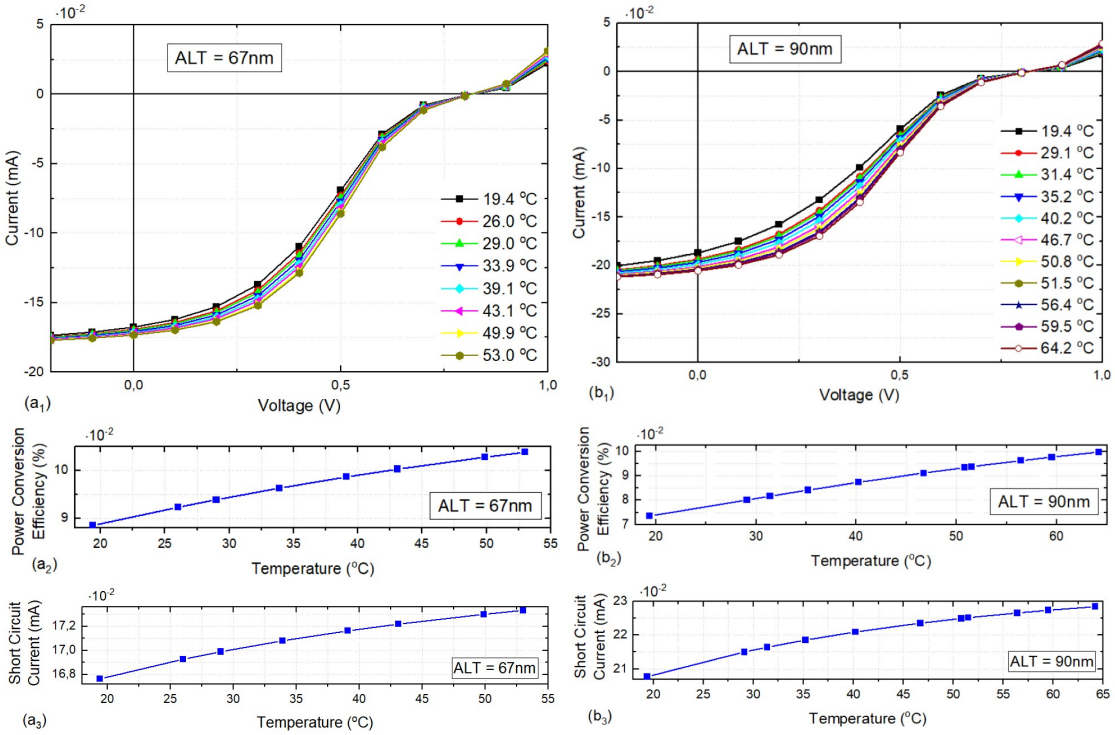

Fig. 2. The I-V characteristics of ITO/PEDOT:PSS/P3HT:ICBA/al solar cells with (a1) 67 nm and (b1) 90 nm active layer thicknesses at different temperatures simulated by standard DDM including Arrhenius-type temperature-dependent hole mobility. The calculated (a2) and (b2) PCE and (a3) and (b3) Isc temperature-dependencies for the same devices, respectively.

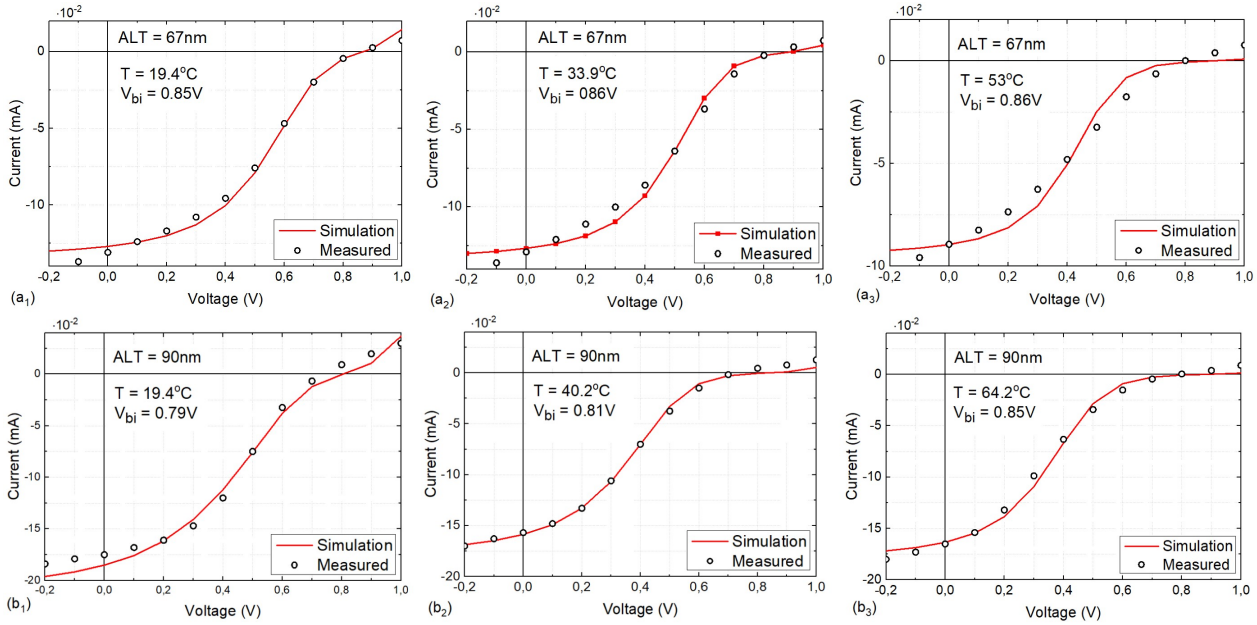

Fig. 3. Comparison of measured and simulated I-V characteristics of ITO/PEDOT:PSS/P3HT:ICBA/al solar cells with 67 nm and 90 nm active layer thicknesses at selected temperatures. Simulations are conducted using DDM with Arrhenius-type temperature-dependent hole mobility together with temperature-dependent IQE and electron SRV at the cathode.

V. Conclusion

Temperature influence on the performance of P3HT:ICBA solar cells was investigated. ITO/PEDOT:PSS/P3HT:ICBA/Al solar cells with two different ALTs were fabricated and characterized under solar simulator light. The *I-V* characteristics were measured within the temperature range of 20 °C-65 °C for both devices, and PCE and I_{sc} as functions of T were determined. The recorded *I-V* curves manifested the S-shape deviation. To simulate the *I-V*(*T*) data, the DDM model including surface recombination on both electrodes and Arrhenius-type *T*-dependent hole mobility was used and resulted in a poor agreement between theory and experiment. To better reproduce the experimental *I-V* curves, the *T*-dependent IQE and electron SRV at cathode were assumed and used in calculations as fitting parameters. This way, a very good

match of calculated with measured *I-V* curves was achieved in the whole temperature range. The obtained IQE(*T*) dependence was nonmonotonic and differed for solar cells with different ALTs. This was attributed to the temperature-induced morphology changes, which are strongly correlated with the P3HT:ICBA thin film thickness [31]. The electron SRV at the cathode showed increasing character with *T,* which is in accord with the fact that it is a trap-assisted recombination mechanism. A further study should be conducted to resolve the correlation between polymer thin film morphology, thickness, and applied temperature.

TABLE 2
THE IQE AND SRV VALUES AT DIFFERENT *T*

ALT= 90 nm		
T (°C)	IQE	Electron SRV [cm/s]
19.4	0.044	8.90×10^{-3}
29.1	0.037	4.55×10^{-4}
31.4	0.040	4.56×10^{-4}
35.2	0.040	5.74×10^{-5}
40.2	0.037	4.63×10^{-5}
46.7	0.046	4.68×10^{-5}
50.8	0.059	1.57×10^{-5}
51.5	0.036	1.57×10^{-5}
56.4	0.053	1.58×10^{-5}
59.5	0.037	4.77×10^{-6}
64.2	0.037	4.80×10^{-6}
ALT= 67 nm		
T (°C)	IQE	Electron SRV [cm/s]
19.4	0.037	4.47×10^{-3}
26.0	0.037	6.46×10^{-4}
29.0	0.040	3.03×10^{-4}
33.9	0.037	1.99×10^{-4}
39.1	0.040	9.24×10^{-5}
43.1	0.029	4.65×10^{-5}
49.9	0.027	2.35×10^{-5}
53.0	0.026	6.75×10^{-6}

ACKNOWLEDGMENT

This work is partially supported by the Serbian Ministry of Education, Science and Technological Development under Grant #171011 awarded to J. Gojanović and P. Matavulj, the National Aeronautics and Space Administration (NASA) grant and Cooperative Agreement Number NNX15AH82H through LaSpace LURA subaward PO-0000107276, and James W. Adams endowed professorship of S. Živanović that is made available through the State of Louisiana Board of Regents Support Funds.

REFERENCES

[1] M. B. Salim, R. Nekovei, and R. Jeyakumar, "Organic tandem solar cells with 18.6% efficiency," *Solar Energy*, vol. 198, pp. 160–166, Mar. 2020, doi: 10.1016/j.solener.2020.01.042.

[2] Q. Liu, Y. Jiang, K. Jin, J. Qin, J. Xu, W. Li, J. Xiong, J. Liu, Z. Xiao, K. Sun, S. Yang, X. Zhang, and L. Ding, "18% Efficiency organic solar cells," *Science Bulletin*, vol. 65, no. 4, pp. 272–275, Feb. 2020, doi: 10.1016/j.scib.2020.01.001.

[3] H. Chen, J. Hou, S. Zhang, Y. Liang, G. Yang, Y. Yang, L. Yu, Y. Wu and G. Li, "Polymer solar cells with enhanced open-circuit voltage and efficiency," *Nature Photon*, vol. 3, no. 11, pp. 649–653, Nov. 2009, doi: 10.1038/nphoton.2009.192.

[4] K. Kawashima, Y. Tamai, H. Ohkita, I. Osaka, and K. Takimiya, "High-efficiency polymer solar cells with small photon energy loss," *Nat Commun*, vol. 6, no. 1, p. 10085, Dec. 2015, doi: 10.1038/ncomms10085.

[5] H. Kang, W. Lee, J. Oh, T. Kim, C. Lee, and B. J. Kim, "From Fullerene–Polymer to All-Polymer Solar Cells: The Importance of Molecular Packing, Orientation, and Morphology Control," *Acc. Chem. Res.*, vol. 49, no. 11, pp. 2424–2434, Nov. 2016, doi: 10.1021/acs.accounts.6b00347.

[6] S. Jin, B. V. K. Naidu, H. Jeon, S. Park, J. Park, S. C. Kim, J. W. Lee, Y. Gal, "Optimization of process parameters for high-efficiency polymer photovoltaic devices based on P3HT:PCBM system," *Solar Energy Materials and Solar Cells*, vol. 91, no. 13, pp. 1187–1193, Aug. 2007, doi: 10.1016/j.solmat.2007.04.001.

[7] J. G. Sanchez, A. A. A. Torimtubun, V. S. Balderrama, M. Estrada, J. Pallares, and L. F. Marsal, "Effects of Annealing Temperature on the Performance of Organic Solar Cells Based on Polymer: Non-Fullerene Using V_2O_5 as HTL," *IEEE J. Electron Devices Soc.*, vol. 8, pp. 421–428, 2020, doi: 10.1109/JEDS.2020.2964634.

[8] Y. Liu, J. Zhao, Z. Li, C. Mu, W. Ma, H. Hu, K. Jiang, H. Lin, H. Ade, and H. Yan, "Aggregation and morphology control enables multiple cases of high-efficiency polymer solar cells," *Nat Commun*, vol. 5, no. 1, p. 5293, Dec. 2014, doi: 10.1038/ncomms6293.

[9] F. Cheng, G. Fang, X. Fan, H. Huang, Q. Zheng, P. Qin, H. Lei, and Y. Li, "Enhancing the performance of P3HT:ICBA based polymer solar cells using LiF as electron collecting buffer layer and UV–ozone treated MoO3 as hole collecting buffer layer," *Solar Energy Materials and Solar Cells*, vol. 110, pp. 63–68, Mar. 2013, doi: 10.1016/j.solmat.2012.12.006.

[10] S. B. Jo, Y. Liu, F. Lin, and A. K. -Y. Jen, "Tackling Energy Loss for High-Efficiency Organic Solar Cells with Integrated Multiple Strategies," *Adv. Mater.*, vol. 30, no. 16, p. 1706816, Apr. 2018, doi: 10.1002/adma.201706816.

[11] W. Cai, X. Gong, and Y. Cao, "Polymer solar cells: Recent development and possible routes for improvement in the performance," *Solar Energy Materials and Solar Cells*, vol. 94, no. 2, pp. 114–127, Feb. 2010, doi: 10.1016/j.solmat.2009.10.005.

[12] L. J. A. Koster, E. C. P. Smits, V. D. Mihailetchi, and P. W. M. Blom, "Device model for the operation of polymer/fullerene bulk heterojunction solar cells," *Phys. Rev. B*, vol. 72, no. 8, p. 085205, Aug. 2005, doi: 10.1103/PhysRevB.72.085205.

[13] L. A. A. Pettersson, L. S. Roman, and O. Inganäs, "Modeling photocurrent action spectra of photovoltaic devices based on organic thin films," *Journal of Applied Physics*, vol. 86, no. 1, pp. 487–496, Jul. 1999, doi: 10.1063/1.370757.

[14] V. D. Mihailetchi, H. X. Xie, B. de Boer, L. J. A. Koster, and P. W. M. Blom, "Charge Transport and Photocurrent Generation in Poly(3-hexylthiophene): Methanofullerene Bulk-Heterojunction Solar Cells," *Adv. Funct. Mater.*, vol. 16, no. 5, pp. 699–708, Mar. 2006, doi: 10.1002/adfm.200500420.

[15] F. Laquai, D. Andrienko, R. Mauer, and P. W. M. Blom, "Charge Carrier Transport and Photogeneration in P3HT:PCBM Photovoltaic Blends," *Macromol. Rapid Commun.*, vol. 36, no. 11, pp. 1001–1025, Jun. 2015, doi: 10.1002/marc.201500047.

[16] Y. Min Nam, J. Huh, and W. H. Jo, "A computational study on optimal design for organic tandem solar cells," *Solar Energy Materials and Solar Cells*, vol. 95, no. 4, pp. 1095–1101, Apr. 2011, doi: 10.1016/j.solmat.2010.12.018.

[17] A. Cheknane, H. S. Hilal, F. Djeffal, B. Benyoucef, and J.-P. Charles, "An equivalent circuit approach to organic solar cell modelling," *Microelectronics Journal*, vol. 39, no. 10, pp. 1173–1180, Oct. 2008, doi: 10.1016/j.mejo.2008.01.053.

[18] G. Li, L. Liu, F. Wei, S. Xia, and X. Qian, "Recent Progress in Modeling, Simulation, and Optimization of Polymer Solar Cells," IEEE J. Photovoltaics, vol. 2, no. 3, pp. 320–340, Jul. 2012, doi: 10.1109/JPHOTOV.2012.2193385.

[19] C. Ma, C. C. S. Chan, X. Zou, H. Yu, J. Zhang, H. Yan, K. S. Wong, and P. C. Y. Chow, "Unraveling the Temperature Dependence of Exciton Dissociation and Free Charge Generation in Nonfullerene Organic Solar Cells," *Sol. RRL*, vol. 5, no. 4, p. 2000789, Apr. 2021, doi: 10.1002/solr.202000789.

[20] A. Mahmoudloo and S. Ahmadi-Kandjani, "Influence of the temperature on the charge transport and recombination profile in organic bulk heterojunction solar cells: a drift-diffusion study," *Appl. Phys. A*, vol. 119, no. 4, pp. 1523–1529, Jun. 2015, doi: 10.1007/s00339-015-9130-3.

[21] K. Tvingstedt, J. Benduhn, and K. Vandewal, "Temperature dependence of the spectral line-width of charge-transfer state emission in organic solar cells; static *vs.* dynamic disorder," *Mater. Horiz.*, vol. 7, no. 7, pp. 1888–1900, 2020, doi: 10.1039/D0MH00385A.

[22] S. A. Hawks, G. Li, Y. Yang, and R. A. Street, "Band tail recombination in polymer:fullerene organic solar cells," *Journal of Applied Physics*, vol. 116, no. 7, p. 074503, Aug. 2014, doi: 10.1063/1.4892869.

[23] S. R. Cowan, N. Banerji, W. L. Leong, and A. J. Heeger, "Charge Formation, Recombination, and Sweep-Out Dynamics in Organic Solar Cells," *Adv. Funct. Mater.*, vol. 22, no. 6, pp. 1116–1128, Mar. 2012, doi: 10.1002/adfm.201101632.

[24] S. R. Cowan, A. Roy, and A. J. Heeger, "Recombination in polymer-fullerene bulk heterojunction solar cells," *Phys. Rev. B*, vol. 82, no. 24, p. 245207, Dec. 2010, doi: 10.1103/PhysRevB.82.245207.

[25] A. Petrovic, J. Gojanovic, P. Matavulj, M. Islam, and S. Zivanovic, "Temperature dependence of P3HT:ICBA polymer solar cells," in *2017 International Conference on Numerical Simulation of Optoelectronic Devices (NUSOD)*, Copenhagen, Denmark, Jul. 2017, pp. 133–134. doi: 10.1109/NUSOD.2017.8010027.

[26] G. Garcia-Belmonte, "Temperature dependence of open-circuit voltage in organic solar cells from generation–recombination kinetic balance," *Solar Energy Materials and Solar Cells*, vol. 94, no. 12, pp. 2166–2169, Dec. 2010, doi: 10.1016/j.solmat.2010.07.006.

[27] I. Riedel, J. Parisi, V. Dyakonov, L. Lutsen, D. Vanderzande, and J. C. Hummelen, "Effect of Temperature and Illumination on the Electrical Characteristics of Polymer–Fullerene Bulk-Heterojunction Solar Cells," *Adv. Funct. Mater.*, vol. 14, no. 1, pp. 38–44, Jan. 2004, doi: 10.1002/adfm.200304399.

[28] K. Tvingstedt and C. Deibel, "Temperature Dependence of Ideality Factors in Organic Solar Cells and the Relation to Radiative Efficiency," *Adv. Energy Mater.*, vol. 6, no. 9, p. 1502230, May 2016, doi: 10.1002/aenm.201502230.

[29] B. Yang, J. Cox, Y. Yuan, F. Guo, and J. Huang, "Increased efficiency of low band gap polymer solar cells at elevated temperature and its origins," *Appl. Phys. Lett.*, vol. 99, no. 13, p. 133302, Sep. 2011, doi: 10.1063/1.3643450.

[30] W. Bagienski and M. C. Gupta, "Temperature dependence of polymer/fullerene organic solar cells," *Solar Energy Materials and Solar Cells*, vol. 95, no. 3, pp. 933–941, Mar. 2011, doi: 10.1016/j.solmat.2010.11.026.

[31] J. Vlahović, M. Stanojević, J. Gojanović, J. Melancon, A. Sharma, and S. Živanović, "Thickness dependent photocurrent spectra and current-voltage characteristics of P3HT:PCBM photovoltaic devices," *Opt. Express*, vol. 29, no. 6, p. 8710, Mar. 2021, doi: 10.1364/OE.418082.

[32] Ž. Jelić, J. Petrović, P. Matavulj, J. Melancon, A. Sharma, C. Zellhofer, and S. Živanović, "Modeling of the polymer solar cell with a P3HT:PCBM active layer," Phys. Scr., vol. T162, p. 014035, Sep. 2014, doi: 10.1088/0031-8949/2014/T162/014035.

[33] A. R. Khalf, J. P. Gojanovic, N. A. Cirovic, S. Zivanovic, and P. S. Matavulj, "The Impact of Surface Processes on the J–V Characteristics of Organic Solar Cells," *IEEE J. Photovoltaics*, vol. 10, no. 2, pp. 514–521, Mar. 2020, doi: 10.1109/JPHOTOV.2020.2965401.

[34] S. Ono and K. Ohno, "Origin of Charge Transfer Exciton Dissociation in Organic Solar Cells," in *Excitons*, S. L. Pyshkin, Ed. InTech, 2018. doi: 10.5772/intechopen.69854.